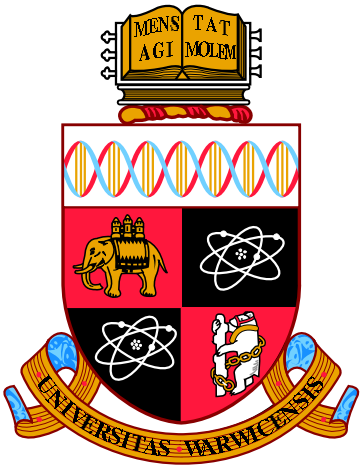

Germanium As a Platform For Semiconductor Spintronics

by

Jamie Matthew Foronda

Thesis

Submitted to the University of Warwick

for the degree of

Doctor of Philosophy

Department of Physics

May 2017

Contents

List of Tables

List of Figures

Acknowledgments

This thesis would not have been complete without the support of a number of people over the past four years. I would like to thank my supervisors Prof. David Leadley and Dr. Maksym Myronov for giving me the opportunity to carry out this Ph.D. and for their general guidance throughout my project.

Next I would like to thank Dr. Maksym Myronov once again for growing me the samples that have formed the basis my project. As for the remainder of the Nano-Silicon group, I am grateful for the guidance given to me by Dr. Chris Morrison on the subject of electrical measurements and spintronics. I would also like to thank Dr. Vishal Shah, Dr. Stephen Rhead and Dr. John Halpin for teaching me all the material techniques I have used in this project and of course Dr. Alan (Turbo) Burton, as without him I'm sure none of the equipment would have worked for long.

As for the members who were students whilst I was here; John, Dave, Olly, Phil, Gerard, James and Cat, I have enjoyed all the fun times weve had in the offices, my Ph.D. and lunch breaks would have been dull without them.

I also would like to thank Leanne, who helped me keep going and supported me, particularly in the last months of writing

Finally I would like to thank my family, without them, I would not have had the opportunity to come this far.

Declarations

The work described in this thesis was carried out either by the author himself, or under the direction/supervision of the author at the Department of Physics, University of Warwick, with the exception of the following cases

- RP-CVD growth of the semiconducting material was carried out by Dr. Maksym Myronov.

- Collection some XPS spectra (as stated in the text), by Dr. Marc Walker.

- Collection of SIMS data carried out by Evans Analytical Group.

The cases in which work was not performed by the author are stated in the text.

Publications

0.1 Publications

0.1.1 Publications Cited in This Thesis

- Reference [58]

  C. Morrison, **J. Foronda**, P. Wisniewski, S. D. Rhead, D. R. Leadley, M. Myronov,

  Evidence of strong spin-orbit interaction in strained epitaxial germanium,

  Thin Solid Films 602, 84 (2016).

- Reference [83]

  J. Foronda, C. Morrison, J. Halpin, S. D. Rhead , M. Myronov,

  Weak antilocalization of high mobility holes in a strained Germanium quantum well heterostructure,

  Journal of Physics-Condensed Matter 27, 022201 (2015).

- Reference [82]

  C. Morrison, P. Wisniewski, S. D. Rhead, **J. Foronda**, D. R. Leadley, M. Myronov,

  Observation of Rashba zero-field spin splitting in a strained germanium 2D hole gas,

  Applied Physics Letters 105, 182401 (2014).

- Reference [36]

  M. Myronov, C. Morrison, J. Halpin, S. Rhead, C. Castelerio, **J. Foronda**,

V. A. Shah, D. R. Leadley,
An extremely high room temperature mobility of two-dimensional holes in a strained Ge quantum well heterostructure grown by reduced pressure chemical vapour deposition,
Japanese Journal of Applied Physics 53, 04EH02 (2014).

0.1.2 Publications Not Cited In This Thesis

- M. Myronov, C. Morrison, J. Halpin, S. Rhead, **J. Foronda**, D. R. Leadley,
  Revealing high room and low temperatures mobilities of 2D holes in a strained Ge quantum well heterostructures grown on a standard Si(001) substrate,
  Solid-State Electronics 110, 35 (2015).

- P. J. Newton, J. Llandro, R. Mansell, S. N. Holmes, C. Morrison, **J. Foronda**, M. Myronov, D. R. Leadley, C. H. W. Barnes,
  Magnetotransport in p-type Ge quantum well narrow wire arrays,
  Applied Physics Letters 106, 172102 (2015).

0.2 Conference Participation

- C. Morrison, **J. Foronda**, M. Myronov,
  The Rashba Spin Orbit Interaction in Ge Quantum Wells
  IOP Magnetism, Sheffield,UK (2016).

- **J. Foronda**, C. Morrison , M. Myronov, J. Halpin, S. D. Rhead, D. R. Leadley,
  Weak Anti-Localization Behaviour of High Mobility 2D Hole Gas in a Strained

Ge QW Heterostructure,
2014 7TH International Silicon-Germanium Technology and Device Meeting (ISTDM), Singapore, SINGAPORE (2014).

- M. Myronov, C. Morrison, J. Halpin, S. Rhead, **J. Foronda**, D. R. Leadley,
  Revealing the high room and low temperature mobilities of 2D holes in a strained Ge quantum well heterostructures grown on a standard Si(001) substrate,
  2014 7TH International Silicon-Germanium Technology and Device Meeting(ISTDM), Singapore, SINGAPORE (2014).

- C. Morrison, M. Myronov, **J. Foronda**, C. Castelerio, J. Halpin, S. Rhead, D. R. Leadley,
  Quantum Transport of a High Mobility Two Dimensional Hole Gas in a Strained Ge Quantum Well,
  2014 7TH International Silicon-Germanium Technology and Device Meeting (ISTDM), Singapore, SINGAPORE (2014).

- C. Morrison, M. Myronov, **J. Foronda**, S. Rhead, D. R. Leadley,
  Transport Properties of Unintentionally Undoped Ge Quantum Well Heterostructure,
  International Conference on the Physics of Semiconductors, Austin, Texas, USA (2014).

- C. Morrison, **J. Foronda**, M. Myronov, S. Rhead, D. R. Leadley, P. Wisniewski
  Zero Field Spin Splitting in a High Mobility Ge 2D Hole Gas,
  International Conference on the Physics of Semiconductors, Austin, Texas, USA (2014).

- C. Morrison, **J. Foronda**, M. Myronov, D. R. Leadley, P. Wisniewski

  Observation of Rashba Spin Splitting in a Ge 2D Hole Gas

  IOP Magnetism, Manchester, UK (2014).

Abstract

The field of semiconductor spintronics is relatively underdeveloped when compared to its metallic counterpart which has found great success in the computer storage industry in hard disk drive head technology and to a lesser extent non-volatile and robust (M)RAM. The use of semiconductors in spintronics is promising with the ability to modulate spins via a gate controlled spin-orbit interaction allowing for spintronic logic and computation devices. Combining this with dilute ferromagnetic semiconductors, which have been suggested as a base for semiconductor MRAM, it may even be possible to integrate MRAM and logic into a single chip to allow for further miniaturisation of devices. In this thesis we look into the suitability of Ge as a platform for semiconductor spintronics verses other popular alternatives such as Si and GaAs.

The first section of this thesis looks at evidence of a strong spin-orbit interaction in low temperature magnetoresistance curves measured in a high mobility ($777{,}000\,\mathrm{cm^2V^{-1}s^{-1}}$) Ge 2DHG. Despite the lack of beatings in Subnikov de Haas oscillations, which often serves as a indicator of a strong spin-orbit coupling, weak antilocalisation like behaviour is seen at low fields. The spin splitting energy extracted from the weak antilocalisation and found to be 0.8 meV with a Rashba parameter of $3.2\times10^{-28}\,\mathrm{eVm^3}$. The spin split energy is comparable to other Ge and III-V 2DHGs, however the Rashba parameter is in fact higher, which we believe is attributed to the high level of remote doping.

The second section focuses on the treatment of ferromagnet/oxide spin tunnel contacts on Ge deposited by evaporation or sputtering, both of which are common in industrial scale fabrication. Annealing XPS studies are conducted on these contacts to examine the temperature limits at which annealing treatments can be done before contacts degrade. Transition line measurements are also examined to look at the electrical characteristics of the deposited contacts.

The final section focuses on the fabrication and measurements of Hanle devices on n-Ge. The extracted spin lifetimes are of the same order as those measured in similarly doped Ge devices, however strong temperature dependencies of both the spin lifetime and spin accumulation signal suggest that the signal measured is strongly influenced by local states within the oxide barrier.

Abbreviations

- 2DEG: 2-Dimensional Electron Gas
- 2DHG: 2-Dimensional Hole Gas
- 3T: 3-Terminal
- 4T: 4-Terminal
- AF: Anti-Ferromagnetic
- AFM: Atomic Force Microscopy
- BF: Bright Field
- BIA: Bulk Inversion Asymmetry
- CCC: Closed Cycled Cryostat
- CVD: Chemical Vapour Deposition
- DF: Dark Field
- DP: Dyakonov-Perel
- EY: Eliot-Yafet
- FET: Field Effect Transistor
- FIB: Focused Ion Beam
- FM: Ferromagnetic

– FTT: Fast Fourier Transform

– GMR: Giant Magneto-Resistance

– HH: Heavy Hole

– HR: High Resolution

– LH: Light Hole

– LRG: Linearly Reverse Graded

– MC: Magnetoconductivity

– MOSFET: Metal-Oxide-Semiconductor-Field-Effect-Transistor

– MR: Magnetoresistivity

– MRAM: Magnetic Random Access Memory

– MTJ: Magnetic Tunnel Junction

– NM: Non-Magnetic

– Ox: Oxide

– PTR: Pulse Tube Refrigerator

– QW: Quantum Well

– RA: Resistance Area product

– R_cA: Contact Resistance-Area product

– R_sA: Spin Resistance-Area Product

– RF: Radio Frequency

– RMS: Root Mean Square

– RP: Reduced Pressure

– RSM: Reciprocal Space Map

– RTA: Real Time Annealing

– SC: Semiconductor

– SdH: Shubnikov de Haas

– SEM: Scanning Electron Microscopy

– SHE: Spin Hall Effect

– SIA: Structural Inversion Asymmetry

– SIMS: Secondary Ion Mass Spectroscopy

– SO(I): Spin Orbit (Interaction)

– TEM: Transmission Electron Microscopy

– TLM: Transmission Line Measurements

– TMR: Tunnelling Magneto-Resistance

– TOA: Take-Off Angle

– TSP: Tunnelling Spin Polarisation

– UHV: Ultra-High Vacuum

– UV: Ultra Violet

– VdP: Van der Pauw

– VS: Virtual Substrate

– WAL: Weak Anti-Localisation

– WL: Weak Localisation

– XPS: X-Ray Photoelectron Spectroscopy

– XRD: X-Ray Diffraction

Chapter 1

Introduction

1.1 Spintronics

The digital age has thrived on technology that employs the transport and manipulation of charge carriers for the transfer and processing of information. Semiconductors have been at the centre of computing since the manufacturing of the first commercial n-p-n bipolar type Si transistor in the mid 1950s to the widely used metal-oxide-semiconductor-field-transistor (MOSFET). A high resistance in these transistor devices corresponds to an 'off' or '0' state and a low resistance an 'on' or '1' state. Spintronics is a branch of electronics which moves away from charge based transport and focuses on the intrinsic angular momentum (spin) of the carriers. The spin of electrons/holes can take the values of either $+\frac{1}{2}$ or $-\frac{1}{2}$ and is what gives spins their magnetic moment ($\boldsymbol{\mu_B}$) that allows interaction with other magnetic moments or magnetic fields. The use of pure spin (polarised) currents promises much lower energies [1].

The field of spintronics was first established in 1988 with the discovery of giant magneto-resistance (GMR). Initial studies on GMR by two independent groups Albert Fert et al. [2] and Peter Grunberg [3] involved ferromagnetic (FM) Fe and anti-ferromagnetic (AF) Cr multilayers. The Cr layers served as a spacer layer, the

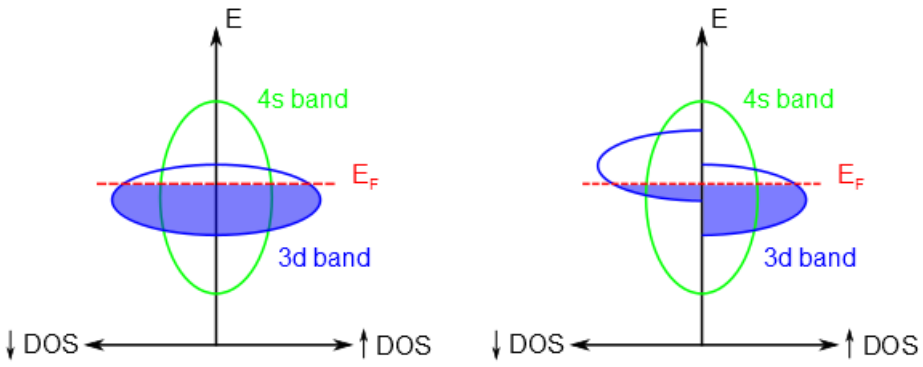

Figure 1.1: Density of states for non-magnetic (NM) transition metals (left) and FM transition meals (right).

particular thickness of which allowed the exchange interaction between adjacent Fe layers to form an antiparallel magnetisation configuration. The application of an in-plane field causes a significant decrease in resistivity when the magnetisation of the Fe layers switch from an antiparallel to parallel configuration. This effect is the result of spin dependant scattering. Resistivity in transition metals originates from scattering events that cause 4s electrons to scatter into the 3d states. In FM materials the density of states in the d-band are spin-split such that the minority spins have more unoccupied states than the majority spins, because of this the minority spin carriers are more likely to be scattered as they will have velocities smaller than majority spins for a given energy. In an antiparallel configuration, the majority carriers that flow from one FM layer to the other become minority spin carriers in the other and thus are preferentially scattered, leading to the increase of resistance. In these first two studies, the magnetoresistance (MR) dropped as far as 3% at room temperature and up to 50% at 4.2 K.

Ferromagnetism arises from the exchange interaction, which causes a spin splitting in the 3d band of FM metals. The spin dependent splitting leads to an imbalance of 3d up and down spin states occupied, as demonstrated in Fig. 1.1. The spin polarisation of a material is defined by the difference in the spin density

of states at the Fermi level (E_F)

$$P = \frac{g_\uparrow(E_F) - g_\uparrow(E_F)}{g_\uparrow(E_F) + g_\uparrow(E_F)} \tag{1.1}$$

$g_{\uparrow,\downarrow}$ refers to the density of states for the spin sub-bands. The asymmetry of the spin up and down density of states at E_F results in a partially spin polarised current, as the 4s and the 3d bands both contribute to conduction in transition metals.

GMR was quickly observed in other multilayer systems such as Co/Ru, Co/Cr and Co/Cu [4][5]. Studies moved onto using spin valve type structures where two FM layers were separated by a spacer and the magnetisation of one FM layer was fixed or pinned using an adjacent AF layer. The sensitivity of GMR in these types of structures led to the use of GMR-based read heads in hard-disk drives, first showcased by IBM in 1997, driving storage densities to much higher capacities (by two orders of magnitudes). The importance of GMR to the field of spintronics and magnetic storage was recognised in 2007 when Fert and Grünberg were awarded the Nobel prize for their discovery. Storage densities were later surpassed with the implementation of tunnelling magnetoresistance (TMR) type heads. This effect stems from GMR in spin valves, with the difference of using a tunnel barrier in place of a NM or AF spacer to from a magnetic tunnel junction (MTJ). Initial measurements showed much larger MR ratios than typically seen in GMR at 20%, more recent experiments boast figures as high as 600%.

Apart from hard disk drive read heads, spintronics has also made an impact in the computing industry in the form of magnetoresistive random-access memory (MRAM)[6], in which information is stored in FM elements that can be switched using electric currents (via the spin torque mechanism). FM elements allow information to be stored in a non-volatile format, furthermore the promise of high speeds and storage density, makes it a future candidate for universal memory. Currently its maximum capacity is relatively low at 64 Mb, however due to its stability in

extreme temperatures and durability (resistive to radiation damage) it has found uses in military and aeronautical industries.

1.2 Semiconductor Spintronics: Introduction and Basic Concepts

Semiconductor spintronics, in contrast to the metal spintronics discussed above is a much newer underdeveloped sector of spintronics. This stems from the fact that conventional semiconductors have no net spin polarization at equilibrium, providing the need for the injection of spin carriers into semiconductors for spintronic devices. Spin injection in materials can be performed in a number of different ways. It had been demonstrated first in GaAs [7] that it was possible to inject spin using circularly polarised light due to GaAs selection rules, other methods also include the spin pumping of an adjacent FM layer [8]. The two methods however, are not practical for real world application of spintronic devices, instead it is also possible to inject spin electrically through the use of a FM electrode.

Once spins are injected into a non-FM material, they will diffuse into the bulk and over a certain length will lose or 'forget' its spin orientation due to the effects of random magnetic fields or spin changing scattering events (discussed later in section 2.3). It follows that the degree of spin polarisation in the bulk material will decay exponentially the further away the spins are from the site of injection. The characteristic time scale at which this happens is known as the spin relaxation time, τ_s and the corresponding length scale L_s (the spin relaxation length) is defined as $L = \sqrt{D\tau_s}$ where D is the diffusion coefficient. L_s thus determines the length scale at which a spintronic device can operate. Semiconductors benefit from having larger values of L_s over metals. Experimentally measured τ_s and L_s values are given for Si, Ge and GaAs in table 1.2.

Over the past 20 years, there has been large progress to the field. Spin

	n-type		p-type	
	τ_s (ps)	L_s (nm)	τ_s (ps)	L_s (nm)
Si	140	230	270	310
Ge	123	830	15	120
GaAs	900	-	320	-

Table 1.1: A table of spin lifetimes and diffusion lengths obtained via electrical measurements for different semiconductors at 300 K [9][10][11].

injection has been achieved both optically [12] and electrically in a number of different semiconductor systems, as well as being detected electrically via the Hanle effect[13][14][15][16][17][18][19][20]. Interesting phenomena such as the spin Hall effect (SHE) [21] has also been observed in GaAs [22] where spin orbit (SO) related, spin dependent scattering induces a fully spin polarised current perpendicular to an applied charge current. Before we discuss semiconductor spintronics further, let us address some basic concepts.

1.2.1 Spin Injection into Non-Magnetic Materials

Initial discussions of electrical spin injection focused on the concept of diffusive FM/NM and FM/NM/FM junctions, with the application of a bias voltage between one FM electrode and the NM layer. The bias voltage effectively raises E_F in the FM, causing electrons to have higher energies than those at E_F in the NM layer allowing a flow of electrons from FM to NM in order for the electrons to achieve a lower energy and equilibrium. As $g_\uparrow(E) \neq g_\downarrow(E)$, an uneven number of up and down spins flow into NM. Conversely, if the bias is reversed, the chemical potential in the NM layer is now higher, reversing the flow. $g_\uparrow(E_F)$ for the FM however is larger than $g_\downarrow(E_F)$, thus allowing more $\uparrow$ spins than $\downarrow$ into the FM and causing the minority $\downarrow$ spins to accumulate in NM. This is known as spin extraction.

For injection into metals electrical injection is trivial, however a problem arises when the conductivity of the spin injecting contact material in vastly different from the bulk material such as semiconductors, in which case the polarisation of

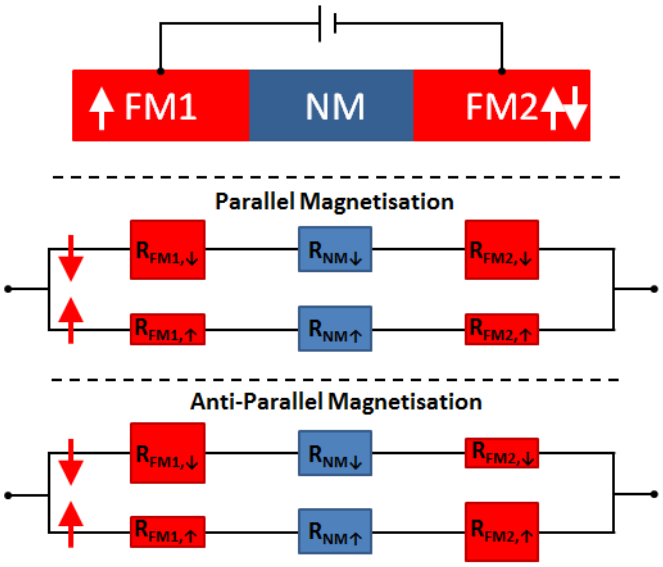

Figure 1.2: A FM/NM/FM junction (the magnetisation of FM1 and FM2 can be parallel or antiparallel) as described by the a simple resistor model. The size of the resistors indicate the degree of resistance. Adapted from [23].

the injected current is very small of the order ∼0.1% [23][24]. This is known as the conductivity mismatch problem and can be derived from the simplified resistor model where contributions to the current are described as two separate conduction channels with equal currents for spin ↑ and ↓ and each material has a respective spin dependent resistance. This is depicted in figure 1.2. In this discussion we label the spin dependent resistance for the FM as $R_{FM\uparrow}$, $R_{FM\downarrow}$ and the NM layer intuitively has $R_{NM\uparrow} = R_{NM\downarrow} = 2R_{NM}$. The efficiency of spin injection is defined by the proportion of spins currents flowing from the FM into the NM

$$\zeta = \frac{j_\uparrow - j_\downarrow}{j_\uparrow + j_\downarrow} \tag{1.2}$$

where $j_{\uparrow,\downarrow}$ are the individual current densities and the charge current density is $j = j_\uparrow + j_\downarrow$. When discussing the behaviour of spins in the spin valve, the spins have separate resistances $(R_\uparrow, R_\downarrow)$ in a material. The spin dependent resistances are

defined as

$$R_{\uparrow} = \rho_{\uparrow}\frac{l}{A} \tag{1.3a}$$

$$R_{\downarrow} = \rho_{\downarrow}\frac{l}{A} \tag{1.3b}$$

where $\rho_{\uparrow,\downarrow}$ are the resistivities of the spin channels and the inverse the spin conductivity $\sigma_{\uparrow,\downarrow}$. The resistor model for an FM/NM/FM junction is given in figure 1.2, for both parallel and antiparallel orientations of the FM electrode's magnetisation, the two FM layers have identical magnetic and electrical properties (i.e. $R_{FM1} = R_{FM2}$). When a spin $\uparrow$ travels through a FM with opposite sign to the magnetisation then the resistance $R_{FM\uparrow}$ is large, if it is parallel the value is small. We define the effective conductivity polarisation for a particular layer as

$$\beta_p = \frac{\sigma_{\uparrow} - \sigma_{\downarrow}}{\sigma_{\uparrow} + \sigma_{\downarrow}} \tag{1.4}$$

which is non-zero in FM and zero in NM. This in combination with the total resistance of the FM, $1/R_{FM} = (1/\rho_{\uparrow} + 1/\rho_{\downarrow})\frac{A}{l}$, equations 1.3a, 1.3b for the FM regions can be changed to

$$R_{FM\uparrow} = \frac{2R_{FM}}{1 + \beta_p} \tag{1.5a}$$

$$R_{FM\downarrow} = \frac{2R_{FM}}{1 - \beta_p} \tag{1.5b}$$

The total resistance for one channel $(R_{\uparrow}, R_{\downarrow})$ is just the series resistance of the spin-dependent current from the three layers. In the antiparallel magnetisation scenario, the two channels will have equal resistances. As $J \propto 1/R$ we can write the spin polarisation across the junction as

$$\alpha_p = \frac{R_{\downarrow} - R_{\uparrow}}{R_{\uparrow} + R_{\downarrow}} \tag{1.6}$$

in which in the antiparallel set-up α_p is zero. For the parallel set-up the resistances of the FM electrodes in a particular spin channel are the same and thus $R_\uparrow = 2(R_{FM\uparrow} + R_{NM})$ and $R_\downarrow = 2(R_{FM\downarrow} + R_{NM})$, substituting these as well as equations 1.5a, 1.5b we have

$$\alpha_p = \frac{R_{FM\downarrow} - R_{FM\uparrow}}{R_{FM\uparrow} + R_{FM\downarrow} + 2R_{NM}} \tag{1.7a}$$

$$\alpha_p = \beta_p \frac{R_{FM}}{R_{NM}} \frac{2}{2R_{FM}/R_{NM} + (1 - \beta_p^2)} \tag{1.7b}$$

We can see that the polarisation is dependent on β_p and a ratio of the FM and NM resistances. This result presents one of the larger obstacles for semiconductor (SC) spintronics and was first pointed out by Schmidt et al [23]. As most conventional FM materials are metallic, the resistance ratio is very small reducing the efficiency of spin injection significantly, even with the use of half metals with a spin polarisation of 100%.

One option to avoid this problem is the use of unconventional ferromagnetic semiconductors [25] as contact material, however these cannot be deposited as easily standard FM and often suffer from low Currie temperatures, much lower than room temperature. Instead Fert and Yaffres found that if the interface resistance of the FM/SC was larger than the spin resistance of both the FM and SC layer, the conductivity mismatch problem could be overcome, the proof of this is provided in [26]. This was also highlighted by Rashba at a similar time [27], suggesting the use of a tunnel barrier and to a lesser extent a Schottky barrier to achieve this effect. Since then, there have been a large number of studies in III-Vs, Si and Ge where efficient spin injection has be achieved through spin tunnel contacts using either insulating (oxide) tunnel barrier such as MgO and Al_2O_3 [13][14][15][16][17][28][29][30] or Schottky tunnel contacts such as Fe_3Si/n_+ and [18][19][20].

1.2.2 Spin Modulation

In addition to spin flip scattering, the orientation of a spin can change with time when in the presence of a magnetic field. If the magnetic moment of an electron ($\boldsymbol{\mu_B}$) has a component perpendicular to an external magnetic field ($\boldsymbol{B}$), the magnetic moment will experience a torque ($\boldsymbol{\Gamma}$) perpendicular to both the moment and $\boldsymbol{B}$ ($\boldsymbol{\Gamma} = \boldsymbol{\mu_B} \times \boldsymbol{B}$) causing the moment or spin or precess about the field (Larmor Precession). The rate of the precession is given as

$$\boldsymbol{\Omega} = \mu_B g \boldsymbol{B}/\hbar \tag{1.8}$$

where g is the Lande g-factor. Although Larmor precession is another source of spin relaxation, it can also be used to modulate spin, this can be achieved more efficiently using the spin orbit interaction (SOI). The SOI was initially realised for electrons orbiting around the electric field of a positive nucleus, intuitively using heavier elements results in a larger SO due to the larger field of the nucleus. The strength of the SOI in semiconductors however are not limited to their 'Z' value, but can also be introduced by forming a structural electrical field (Rashba SOI) such as one found in asymmetrical quantum wells [31]. Further tuning is possible simply by introducing a gate voltage to adjust the electrical field in the material. Further details will be discussed in section 2.2.1.

Electrical tuning of the SOI, forms the core concept for the spin-analogue of the field effect transistor (FET) proposed by Datta and Das in 1990 [32] for use in spin based computing logic. The proposed device consists of a FM source and drain used to inject a spin polarised current separated by a gated a 2-dimensional hole or electron gas channel, as depicted in figure 1.3. Spins traversing the channel precess due to the effective magnetic field from the SOI. The SOI can be tuned such that the spins arriving at the drain can either the have the same orientation as it had at the source, or have precessed to the extent of which the spins have flipped

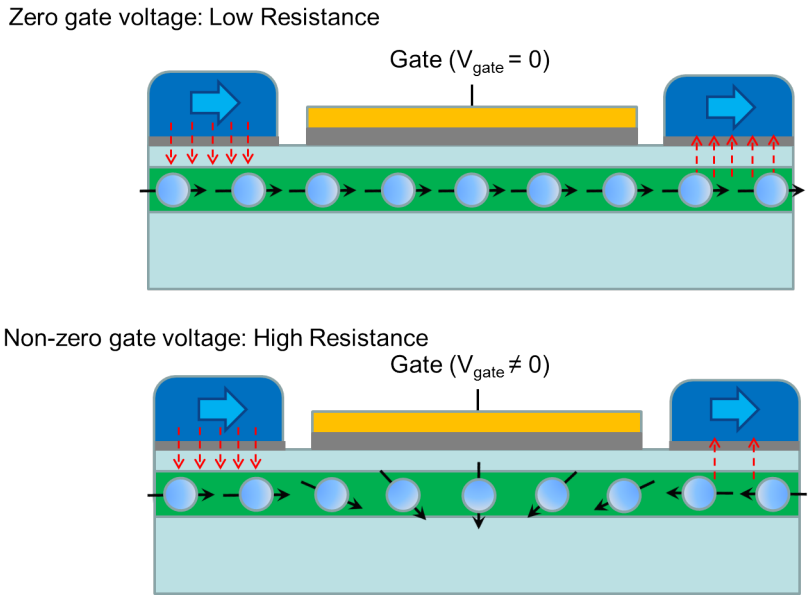

Figure 1.3: Schematics for the operation of a spin-FET. In this case a zero gate voltage corresponds to a low resistive 'on' state.

orientation. If spins have the same orientation as the magnetisation of the drain, the resistance across the contacts is low, if the spins have the opposite orientation, then the resistance across the transistor is high. The gate voltage is used to switch the transistor on and off by modulating the SOI via a gate voltage.

The demonstration of both semiconductor based MRAM and spin logic would be a large development in the field of spintronics, giving rise to the possibility of unifying both storage and logic capabilities onto a single chip. The combination of the two functions onto a single chip is becoming more attractive with the miniaturisation of technology, with the additional benefit of lower power consumption when compared to current mobile technology.

1.2.3 Motivation and Thesis Outline

A significant portion of research in semiconductor researched has focused on III-V materials such as GaAs [11][22] and InGaAs [33]. Being a direct bandgap material, its popularity was initially down to the ability to probe or inject spin optically,

however other advantages also include large SOI and large mobilities for large spin relaxation lengths. A major disadvantage of using non-centrosymmetric semiconductors (group III-V and II-VI), is the presence of the Dresselhaus SOI due to the inversion asymmetry of these materials [34]. This SOI effect is not tuneable like the Rashba interaction and can cause additional spin relaxation. The Dresselhaus SOI will be discussed further in section 2.2.1

As for group IV materials, Si has also been popular, as its wide spread use in the electronics industry has meant Si processing is well established and thus an Si platform is desirable to industry. Its relatively low mass and in turn weak SOI, implies long spin relaxations times and although some cite this as an advantage, it also sacrifices performance in spin modulation devices.

In this thesis I examine the feasibility of using Ge as a platform for semiconductor spintronics. Ge alternately combines the advantage of both V-III semiconductors and Si. As a heavier element than Si the SOI interaction in Ge is larger, but does not suffer from the Dresselhaus SOI that III-Vs have. Furthermore as a group IV material it remains compatible with the widely established processing techniques and high mobilities have routinely been achieved [35][36] by staining 2D Ge layers, approaching III-V values.

In chapter two I outline the basic properties of Ge and Si as well as the concepts required to understand later discussions on SOI and SOI-related phenomena. Experimental techniques along with their associated analysis techniques employed during the investigation will be discussed in chapter three. Chapter four studies the Rashba SOI of a highly strained Ge quantum well (QW) through low temperature magnetoresistance measurements. Later chapters are dedicated to investigating the effectiveness of spin tunnel contacts, namely using Ni, NiFe, Al_2O_3 and MgO fabricated with common deposition tools. First in chapter five, an annealing study using x-ray photoelectron spectroscopy, looks at the thermal stability of these contacts required for processing and annealing treatments, this is followed the electrical

characterisation of as deposited tunnel contacts. Chapter six focuses on the measurement of the spin lifetime in n-Ge using the as deposited Ni/Al_2O_3. Following these results chapters a summary of the investigation is given and suggestions on what future progress could be made in this line of research.

Chapter 2

Theoretical Discussion

2.1 Properties of Silicon and Germanium

Si and Ge are group-IV semiconductors with a diamond cubic crystal structure illustrated in figure 2.1. The basic properties of Si, Ge and other semiconductors are given in table 2.1.1. With a Z number of 14, Si has a smaller lattice parameter of a_{Si} =5.431 Å with Ge at a_{Ge}=5.658 Å [37]. Both of these elements can be combined to form an alloy (of the same structure) $Si_{1-x}Ge_x$ where x is the ratio of Ge in the material which can take the values $0< x <1$. The resulting lattice parameter of the $Si_{1-x}Ge_x$ at a particular temperature is determined by Vergard's law (essentially a weighted average of the two lattice parameters) defined as

$$a_{Si_{1-x}Ge_x} = (1-x)\cdot a_{Si} + x\cdot a_{Ge} - 0.00273x(1-x) \tag{2.1}$$

where a_{Ge} and a_{Si} are the lattice constants at the desired temperature and the latter term is a correction factor initially proposed by Kasper and later modified by Salvador et al after a linear deviation was discovered from measurements of various compositions [37][38][39].

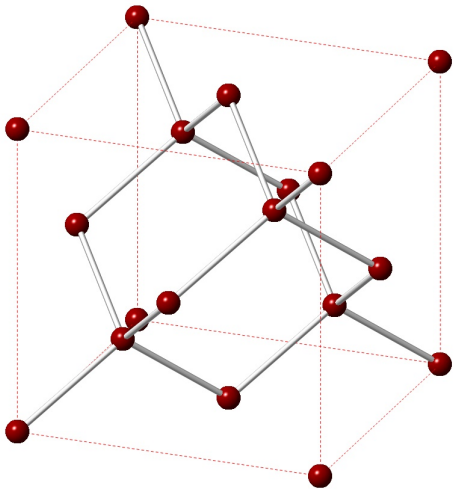

Figure 2.1: A diagram of the diamond cubic unit cell, generated in the Crystal Maker program.

2.1.1 Band Structure of Ge and Si

The band structure of a material describes the possible energies an electron can have when occupying certain states in a lattice (characterised by the wave vector $\boldsymbol{k}$), these are derived by solving the wave functions of electrons in a periodic potential which is defined by the lattice of atoms/molecules. The band gap of semiconductors is defined as the energy between the conduction (minima) and valence band (Γ maxima), where there is forbidden range of energies in which there are no states for electrons to occupy in the absence of any impurities. Both Si and Ge have indirect band gaps where the Si conduction band minima is in the [100] direction (known as the Δ minima) with a band gap of 1.12 eV and the Ge minima occurs in the [111] direction (L minima) forming a band gap of 0.66 eV. The band diagrams for Si and Ge are given in Figure 2.2. For $Si_{1-x}Ge_x$ alloys, the band gap decreases in energy from the Si value down to the Ge value as x is increased. It has been found that for $0< x <0.85$, the conduction band minima is Si-like (Δ), transitioning to an L minima for $0.85< x <1$ [40].

The conduction band in semiconductors contain s-like states corresponding

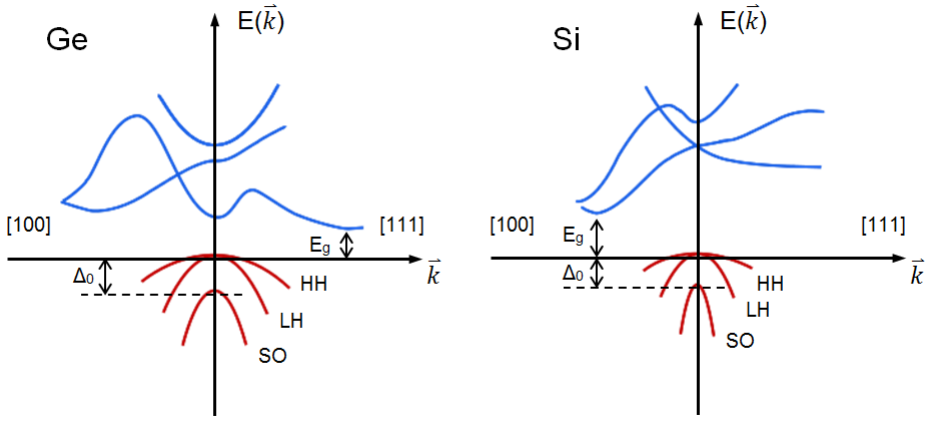

Figure 2.2: Ge (left) and Si (right) band structure.

to an angular momentum of $l = 0$, where as the valence bands are p-type ($l = 1$), as a consequence the valence band is formed of three bands corresponding to states with total angular momentum ($j = l + s$) $j = 3/2$ where $m_j = \pm 3/2, \pm 1/2$ (the projection of total angular momentum on an arbitrary axis) and $j = 1/2$ with $m_j = \pm 1/2$. At the valence band maxima ($\boldsymbol{k} = 0$), when ignoring the SOI the three bands are expected to be six-fold degenerate. Due to the $s = -1/2$ of the $j = 1/2$ band, the SOI lifts the degeneracy between the $j = 3/2$ and $j = 1/2$ bands, inducing a SO-split energy Δ_0 (for which in Ge is Δ_0^{Ge} =0.30 eV and for Si Δ_0^{Si} =0.044 eV) [37][38]. The shift in the $j = 1/2$ band has led it to be called the spin orbit-split band.

The two $j = 3/2$ bands are known as the heavy hole (HH) and light hole (LH) bands, due to their effective masses (m^*). The effective mass is used, as the mass of a carrier is different in a periodic potential than in a vacuum. The effective mass of a carrier is derived from the curvature of the band it occupies. Close to the valence band minima, the bands can be considered parabolic taking the form $E_v = \hbar^2 \boldsymbol{k}^2 / 2m^*$. As shown in figure 2.2 the LH band has a larger curvature than the HH band corresponding to a smaller m^*. The carrier mobility (μ) is related to

the effective mass using the following equation

$$\mu = \frac{q\tau_{tr}}{m^*} \tag{2.2}$$

where q is the carrier charge and τ_{tr} is the transport scattering time, the inverse of which is the summation of the scattering rates of the various scattering mechanisms (Matthiessen's rule). The lower m^* for carriers in bulk Si in comparison to Ge accounts for the higher mobilities in bulk Ge.

From the values of m^* in table 2.1.1, it can be seen why Si suffers from lower mobilities than Ge.

2.1.2 Strain Effects in Germanium

The growth of a material onto a substrate with the same crystal structure and different lattice parameter can lead to the top-most layer becoming strained, where the atoms/molecules of the top-most layer attempt to match the positions of the corresponding atoms/molecules in the layers below. When Si, Ge and $Si_{1-x}Ge_x$ alloys grown in the (001) direction are under strain, the unit cell deforms tetragonally, such that a reduction in in-plane parameters (a_x, a_y) leads to an increase in out-of-plane parameter (a_z). a_z of a strained sample grown on a (001) substrate can be calculated with the following equation

$$a_z = a_{bulk} + \frac{2c_{11}}{c_{12}}(a_{bulk} - a_x) \tag{2.3}$$

where c_{11} and c_{12} are the elastic moduli. Figure 2.3 illustrates the type of strain produced when growing onto substrates with differing lattice parameters. If the epitaxial layer is strained to a substrate with a larger lattice parameter, the epitaxial layer will be under tensile strain, conversely if the substrate has a smaller lattice parameter the top layer will be compressively strained.

Semiconductor	Structure Type	Lattice Parameter (Å)	E_g (eV)	Δ_0 (eV)	m^*_{el} (m_0)	m^*_{et} (m_0)	m^*_{hh} (m_0)	m^*_{lh} (m_0)	μ_e ($cm^2V^{-1}s^{-1}$)	μ_h ($cm^2V^{-1}s^{-1}$)
Si	Diamond	5.431	1.12	0.044	0.92	0.19	0.49	0.16	1450	450
Ge	Diamond	5.658	0.66	0.29	1.59	0.08	0.33	0.043	3900	1900
$Si_{0.5}Ge_{0.5}$	Diamond	5.538	0.92	0.167	∼0.92	∼0.19	-	-	-	-
GaAs	Zinc Blende	5.653	1.43	0.341	1.98	0.37	0.51	0.082	9340	450
GaN	Zinc Blende	4.52	3.2	0.02	0.13	0.13	0.19	1.3	1000	3500

Table 2.1: A table containing the basic material and transport properties of common bulk semiconductors at 300 K [37][41].

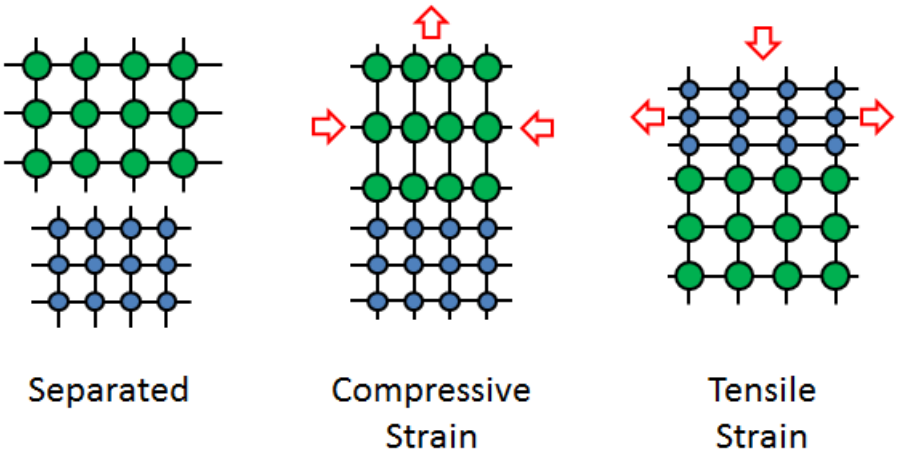

Figure 2.3: A diagram demonstrating compressive and tensile strain.

The strain (ε) of an epitaxial layer with respect to the substrate is given by

$$\varepsilon = \frac{a_{substrate} - a_{layer}}{a_{substrate}} \tag{2.4}$$

The lattice mismatch for Ge and Si is 4.17% meaning Ge grown on Si will be compressively strained ($\varepsilon = -0.0471$). As stated earlier $Si_{1-x}Ge_x$ alloys can have a lattice parameter that can take intermediate values between that of Si and Ge by varying x, this can be used to achieve different levels of compressive biaxial strain in Ge layers ($-0.0417 > \varepsilon > 0$) by growing crystalline Ge on $Si_{1-x}Ge_x$ virtual substrates (VS) [42][43]. Inversely, it is possible to produce tensile strained Si using Ge or $Si_{1-x}Ge_x$ VS and tensile strained Ge using Ge_xSn_{1-x} VS. The amount of material it is possible to strain is however limited, above a critical thickness misfit dislocations form to release the strain in a layer, this thickness will decrease as the mismatch between lattice parameters increase. For Ge on Si, the critical thickness has been measured to be only 4 monolayers when grown by MBE [44].

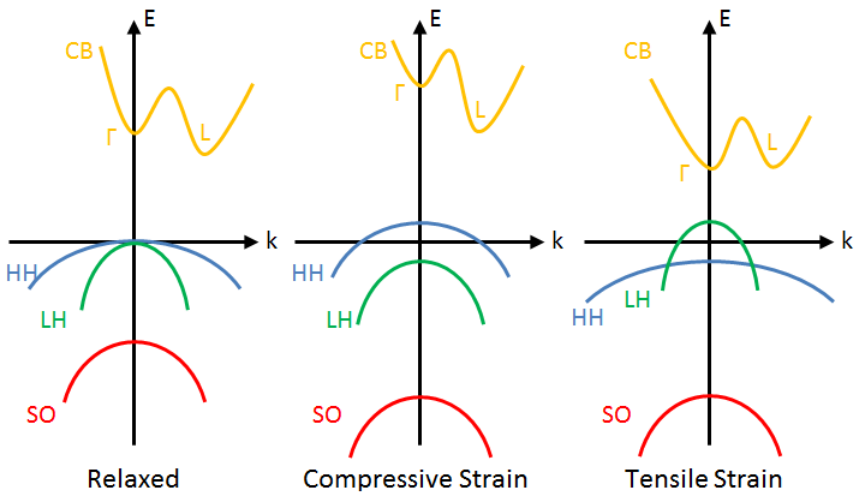

Figure 2.4: A qualitative schematic on the effect of compressive and tensile strain on the band structure of Ge.

Strain Effects On Bands and Carrier Transport

Strain engineering has routinely been used to enhance the transport properties in 2DEG and 2DHG [35][36][43]. The introduction of strain into a semiconductor often results in the deformation of bands (reducing parabolicity and changing m^*) and a shift in energy. A qualitative schematic of strain effects on the Ge band structure is given in figure 2.4. Inducing compressive strain shifts the HH band up in energy and decreases m^*_{HH} (making it more LH-like) whilst lowering the LH band and increasing m^*_{LH}. Due to the shifts in LH and HH bands, the valence band at the Γ-point becomes only two-fold degenerate and only the HH-band is occupied for low hole concentrations, furthermore the lowering of m^*_{HH} enhances μ (as seen in equation 2.2). In the case of tensile strain the inverse happens where the LH band reduces in m^* and rises above the HH band, which increases in m^*. The result is the occupation of only the LH band, again increasing μ due to the overall reduction of m^* (due to both the lack of HH and band deformation). In terms of the conduction band, tensile strain causes the conduction band to shift downwards, with the Γ

valley shifting at a faster rate than the L valley, these valleys move in the opposite direction for compressive strain.

2.2 Spin-Orbit Interaction

The SOI is a relativistic effect in which moving spins interpret electric fields as effective magnetic fields and forms the basis of a number of interesting phenomena in both spintronics and quantum computing [45]. Its initial discovery was used to describe the interaction between the spin and orbital angular momentum of an electron. In the rest frame of the nucleus, the electron can only see the electric field of the positive atom ion. In the stationary reference frame of the electron, the charged nucleus appears to be travelling in an orbital motion around the electron, thus generating a magnetic field perpendicular to the velocity ($\boldsymbol{\nu}$) of the electron/nucleus and the electric field with magnitude

$$\boldsymbol{B_{SO}} = (1/c)\boldsymbol{E} \times \boldsymbol{\nu} \tag{2.5}$$

Figure 2.5 illustrates the resulting effective $\boldsymbol{B_{SO}}$ from the application of an electric field to an electron applied perpendicular to $\boldsymbol{\nu}$.

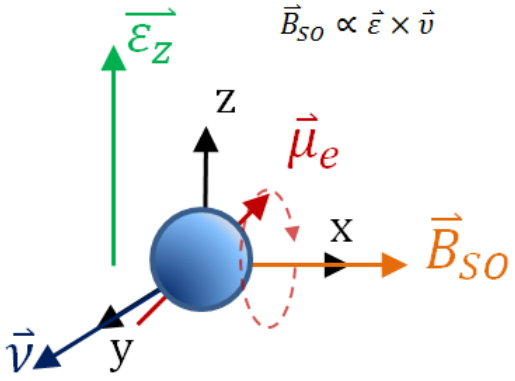

Figure 2.5: A diagram of the SO-effective magnetic field $\boldsymbol{B_{SO}}$ on an electron travelling at velocity $\boldsymbol{\nu}$. The dotted red line traces the precession of spin due to $\boldsymbol{B_{SO}}$.

Like Zeeman splitting, this effective field leads to a shift/slitting in atomic energy levels ($\pm\boldsymbol{\mu_B B}$). The size of the energy shift is dependent on the intrinsic and orbital angular momentum (s and l) as well as the 'Z' (atomic) number of the nucleus which defines the magnitude of the electric field. This generally means heavier elements tend to generate larger SO energy shifts than lighter elements.

2.2.1 Rashba and Dresselhaus Spin Orbit Interactions

The SOI felt by conduction electrons or holes due to the positive field of the nucleus is in reality fairly small due to the masking of the nucleus' electric field by other electrons. There are however other sources of the SOI, Dresselhaus first suggested that crystal structures lacking structural inversion symmetry such as the zinc blende type crystal that most III-V semiconductors have, will have an additional contribution to the zero field spin splitting [34]. In the case of inversion symmetry, the spin states are degenerate such that $E_+(\boldsymbol{k}) = E_+(-\boldsymbol{k})$ (where + and − refer to spin up and down) and with time inversion symmetry, $E_+(\boldsymbol{k}) = E_-(-\boldsymbol{k})$ (as time inversion reverses spin orientation as well as momentum). With the combination of these symmetries it follows that $E_+(\boldsymbol{k}) = E_-(\boldsymbol{k})$, where both spin states have the same energy, removing this symmetry gives rise to a spin dependent splitting.

The spin splitting arising from the inversion asymmetry of the crystal lattice as suggested by Dresselhaus is known as either the Dresselhaus SOI or bulk inversion asymmetry (BIA). The Hamiltonian for the spin splitting originating from inversion asymmetry can take a Zeeman-like form

$$H_{SO} = \frac{\hbar}{2}\boldsymbol{\sigma} \cdot \boldsymbol{\Omega}(\boldsymbol{k}) \tag{2.6}$$

where $\boldsymbol{\Omega}(\boldsymbol{k})$ is the Larmor frequency of the effective magnetic field and $\boldsymbol{\sigma}$ is the spin vector form. For Dresselhaus SOI, $\boldsymbol{\Omega}(\boldsymbol{k})$ (and therefore the field) has a cubic $\boldsymbol{k}$ dependency, however due to the centro-symmetric structure of diamond, Si and Ge do

not suffer from BIA and by extension Dresselhaus SOI. The Dresselhaus interaction is independent of any external electric field and thus cannot be tuned.

Centro-symmetric semiconductors can experience inversion asymmetry due to the inclusion of a non-symmetric potential built into the structure [31], this is known as Bychkov-Rahsba SOI and will be referred to as the Rashba interaction for the remainder of this thesis. Structural inversion asymmetry (SIA) appears in asymmetric quantum wells and at 2D-layer interfaces due to the band discontinuity and takes into account the addition of a potential from an external electric field, allowing control over the strength of the SOI which has been demonstrated in numerous gated heterostructures [46][47][48]. The asymmetry of a QW is easily achievable through asymmetric modulation doping. The dopants in the remote supply layer are charged due to either donating (n-type) or accepting (p-type) electrons into the surrounding structure. This localised charge thus causes an electric field, by growing a doping supply layer on one side of the QW, a linear potential will form across the channel.

For electrons, the Rashba SOI is linear in $\boldsymbol{k}$, taking the form $\boldsymbol{\Omega}_R^{(1)}(\boldsymbol{k}) \propto \alpha_R(\boldsymbol{k_y}, -\boldsymbol{k_x}, 0)$ where α is the Rashba parameter, ε_z is the electric field perpendicular to the 2D plane and $(\boldsymbol{k_x}, \boldsymbol{k_y}, 0)$ are elements of $\boldsymbol{k}$ in the 2D plane [49][50]. The so called Rashba parameter, α_R quantifies the strength of the Rashba SOI and is often used to compare the relative strength of the Rashba interaction between different material systems. The spin splitting of the conduction at the Fermi wavevector $\boldsymbol{k}_F$ is related to α_R by

$$\Delta_0 = 2\alpha_R \boldsymbol{k}_F \tag{2.7}$$

The Rashba interaction in the valence band however is more complicated with the LH and HH bands behaving differently from each other. The LH band is known to behave like electrons in the conduction band with a $\boldsymbol{k}$-linear dependency, whilst the Rashba interaction is closer to the Dresselhaus interaction with a $\boldsymbol{k}$-cubic depen-

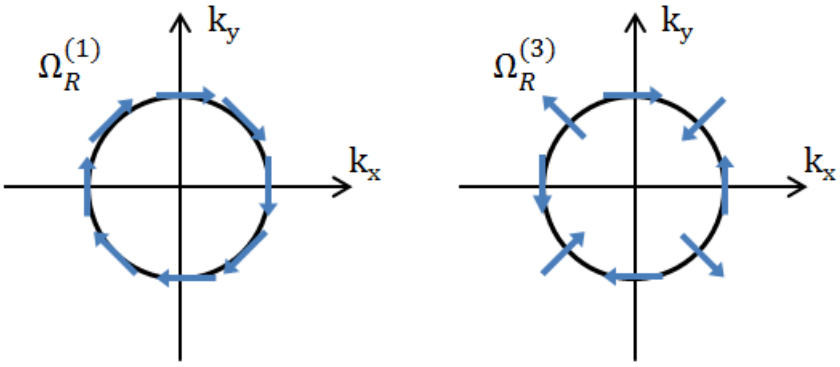

Figure 2.6: The effective magnetic field direction for a given in plane wave vector for the case of a pure linear Rashba system (left) and a pure cubic Rashba system right. Adapted from reference [48].

dency where $\boldsymbol{\Omega}_R^{(3)} \propto \beta_R(3\boldsymbol{k}_x^2\boldsymbol{k}_y - \boldsymbol{k}_y^3, 3\boldsymbol{k}_x\boldsymbol{k}_y^2 - \boldsymbol{k}_x^3, 0)$ [49][51]. The spin split energy for a pure HH population is given by

$$\Delta_0 = 2\beta_R \boldsymbol{k}_F^3 \tag{2.8}$$

where β_R is the $\boldsymbol{k}^3$ Rashba coefficient. For a LH dominated system, equation 2.7 applies. In general

$$\Delta_0 = 2\hbar\boldsymbol{\Omega} \tag{2.9}$$

The two effective precession vectors when plotted show the dependence of the effective field direction on $\boldsymbol{k}$, an example of this is given in figure 2.6. As the effective field is dependent on $\boldsymbol{k}$, the spin quantization axis is coupled to $\boldsymbol{k}$ by the SO interaction, for a system with purely Rashba SOI, the spin are always orientated within the 2D plain.

Strain Effects On the Rashba Interaction

An additional complication to the separate spin splitting behaviour is the degeneracy of the LH and HH bands. With the occupation of both bands, the Rashba interaction can be complicated by the contribution of both $\boldsymbol{k}$ and $\boldsymbol{k^3}$ effects. A small population of holes and the application of strain can separate the two valence bands such that only one sub-band is occupied, as discussed in section 2.1.2. Although this simplifies the behaviour of the Rashba SOI, it has been shown that that the LH-HH separation actually competes with spin splitting, effectively weakening the SOI [49][52][53]. Increasing strain, there by increasing the separation between the LH and HH bands results in a reduction of $\alpha_R(\beta_R)$, and has been demonstrated in a single heterostructure where strain was applied and controlled using a piezoelectric stage [54].

2.2.2 Subnikov de Haas Oscillations

Landau Levels

In 2D quantum confined systems, electrons in high magnetic fields, perpendicular to the 2D plane move in circular orbits in between scattering due to the Lorentz force. If one includes the presence of a perpendicular magnetic field in the Hamiltonian, the structure of the Hamiltonian takes the form

$$\hat{H} = \frac{\hat{\boldsymbol{p_x}}^2}{2m} + \frac{1}{2}\left(\hat{\boldsymbol{p_y}} - \frac{q\boldsymbol{B}\hat{\boldsymbol{x}}}{c}\right)^2 \tag{2.10}$$

Substituting the equation for cyclotron frequency ($\omega_c = qB/mc$) in the second term of the Hamiltonian produces a form describing a simple harmonic oscillator with eigenvalues $E_n = \hbar\omega_c(n + \frac{1}{2})$, where n denotes the different Landau levels ($n >$0 integer values). The inclusion of ω_c in the eigenvalues means that an increase in magnetic field also increases the energy gap between Landau level. The number of

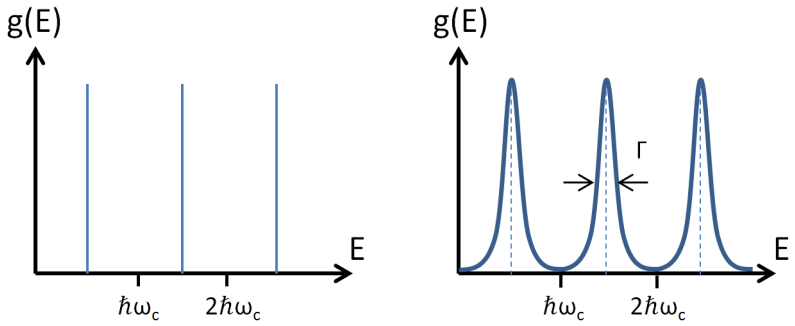

Figure 2.7: A diagram showing the density of states in a magnetic field for ideal δ-like Landau levels (left) and Lorentzian like Landau levels due to scattering (right), adapted from [55].

states per Landau level is given by

$$n_{2D} = \frac{eB}{h} \tag{2.11}$$

In an ideal situation the Landau levels should take a δ-function form and only appear when $\hbar\omega_c \geq K_B T$, however in the presence of scattering, these energy levels broaden and take on a Lorentzian form for low temperatures as depicted in figure 2.7. The width of the Lorentzian is $\Gamma = \hbar/\tau_q$, where τ_q is the quantum lifetime. τ_q is the time in which we expect an electron (hole) to scatter [55].

Oscillations in Magnetoresistance

When the field is increased in a 2D material, the separation between Landau levels increases and E_F will move through the levels. At integers of ν (where ν denotes the number of levels filled), the Landau levels occupied are completely full and E_F rests between levels, at which point scattering cannot occur. When passing through a level, the electrons in that level are free to contribute to the conductivity of the sample. This should in theory produce a magnetoresistance (MR) that resembles a square wave (when taking into account the Lorentzian shape levels), however at the edges of a material, cyclotron paths intersect with the boundary and scatter. This

edge effect bends the Landau levels at the edge of the sample up to higher energies allowing for conduction paths along the edges of the material even at integer filling factors.

These effects manifest as oscillations that expand exponentially in amplitude in the MR of a material, with minima corresponding to filled Landau levels. For this to be observable, the carriers must be degenerate, the magnetic field must be large enough for the formation of Landau levels ($\mu B \gg 1$) and $k_B T \ll \omega_c \hbar$ such that carriers cannot be thermally excited into higher Landau levels. This behaviour in the MR is described by [56][57]

$$\frac{\Delta\rho_{xx}(B)}{\rho_{xx}(0)} = 4cos\left(\frac{2\pi m^* E_F}{\hbar eB}\right) exp\left(-\frac{\pi m^* \alpha_D}{eB\tau_{tr}}\right) \frac{\psi}{sinh(\psi)} \tag{2.12a}$$

$$\psi = \frac{2\pi^2 k_B T m^*}{\hbar eB} \tag{2.12b}$$

where α_D is the Dingle ratio τ_q/τ_{tr}. It can be seen that the oscillations are generated from the cosine with a frequency dependent on E_F. A plot of the MR as a function of $1/B$ such that the frequency of oscillations are constant, can be used to extract the carrier density using

$$n_{2D} = \frac{q}{\pi\hbar\Delta(1/B)} \tag{2.13}$$

where $\Delta(1/B)$ is the separation between maxima.

The SOI does however cause a difference in populations between the two spin sub-bands due to the energy shift Δ_0. If the shift is large enough, Landau levels of the spins split and the superimposed SdH behaviour of the two populations produce a beating effect, changing equation 2.12a into

$$\frac{\Delta\rho_{xx}(B)}{\rho_{xx}(0)} = 4cos\left(\frac{2\pi m^*(E_F \pm \Delta_0)}{\hbar eB}\right) exp\left(-\frac{\pi m^* \alpha_D}{eB\tau_{tr}}\right) \frac{\psi}{sinh(\psi)} \tag{2.14}$$

The SO-splitting energy may then be extracted by finding the difference in

the two populations calculated from the respective FTT plot of the $(1/B)$ behaviour. Similarly at high enough fields the Landau levels also become split due to Zeeman splitting, the onset of this is decided by the size of the Landé g-factor.

It is also possible to extract m^* and τ_q from SdH oscillations, where as τ_{tr} is related to μ by equation 2.2 and is extracted from Hall measurements described in section 3.4.2. The process in which these two factors are extracted is an iterative process and goes beyond the scope of this thesis, a description of the methodology is described in [58].

2.2.3 Weak Localisation

Weak localisation (WL) is a quantum interference effect which increases the resistivity of a material at low temperatures and magnetic fields. The phenomena arises from the interference of coherent partial electron waves travelling in closed loops. Consider the case in figure 2.8, an electron undergoes a series of scattering events such that the path taken forms a closed loop. In quantum mechanics, a partial electron wave has a wavefunction defined as

$$\psi = Ae^{i(\boldsymbol{kr}-\varepsilon(\boldsymbol{k})t/h)} \tag{2.15}$$

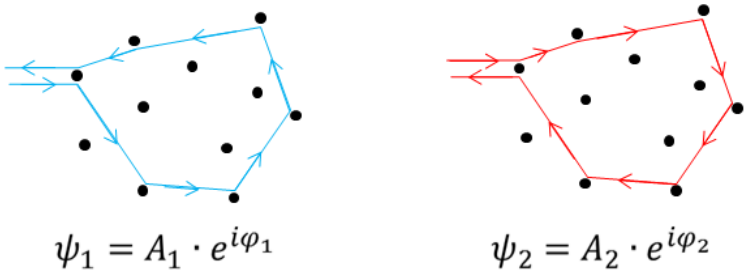

Figure 2.8: An electron backscattering after undergoing a series of scattering events forming a closed loop. The closed loop that results in back scattering can be described by two separate partial electron waves forming the loop in opposite directions.

The two partial electron waves going in opposite directions can be described in a simpler form; $\psi_1 = A_1 e^{i\phi_1}$ and $\psi_2 = A_2 e^{i\phi_2}$, where ϕ is the phase. Classically the probability of forming this closed loop is described by

$$P = |\psi_1|^2 + |\psi_2|^2 = |A_1|^2 + |A_2|^2 \tag{2.16}$$

however as quantum mechanics allows for the superposition of these partial electron waves, the probability is given as

$$P = |\psi_1 + \psi_2|^2 = 2|A|^2(1 + cos(\Delta\phi)) \tag{2.17}$$

This contains an additional term, which is dependent on the phase difference between the partial electron waves. If the scattering events in the closed loop are time reversible, the electron waves at the final point will be in phase with each other and will therefore constructively interfere and increase the probability of backscattering. The phase breaking length (L_ϕ) is defined as the path length required for the partial electron wave to undergo a phase breaking scattering event, which can be expressed as

$$L_\phi = \sqrt{D\tau_\phi} \tag{2.18}$$

where D is the diffusion coefficient and τ_ϕ (the phase breaking scattering time) is related to the inelastic scattering rate by Matthiessen's rule

$$\frac{1}{\tau_\phi(l,T)} = \frac{1}{\tau_\phi^0(l)} + \frac{1}{\tau_{in}(l,T)} \tag{2.19}$$

Here all terms are dependent on the elastic mean free path l and $1/\tau_\phi^0(l)$ is the temperature independent phase breaking scattering rate [59]. The scattering mechanisms thought to contribute to $1/\tau_{in}$ are believed to be carrier-carrier scattering, phonon-carrier scattering and Nyquist scattering (scattering from the time fluctuation electric field of the surrounding carriers) [59][60].

For a closed loop to contribute to WL effects, its path length must be larger than the elastic mean free path (which is commonly assumed to be equal to the transport scattering length L_{tr}) and smaller than L_ϕ. It can thus be seen that for WL effects to occur at all then $L_\phi > L_{tr}$.

WL is most noticeable in magnetoresistance measurements, where the application of a perpendicular magnetic field produces an additional phase difference

$$\Delta\phi = \frac{2e}{c\hbar} \oint \boldsymbol{A} \cdot d\boldsymbol{l} \tag{2.20}$$

where $\boldsymbol{A}$ is the magnetic potential vector related to the field by $\boldsymbol{B} = \bigtriangledown \times \boldsymbol{A}$. The total phase difference is equal to $2e\Phi/c$, where Φ is the magnetic flux within the area of the loop [61]. Increasing this field will cause the phase difference to increase thus reducing the second term in equation 2.17. The resulting dependence causes WL to manifest as a peak about the zero-field in MR measurements (i.e. negative MR) as depicted in figure 2.9.

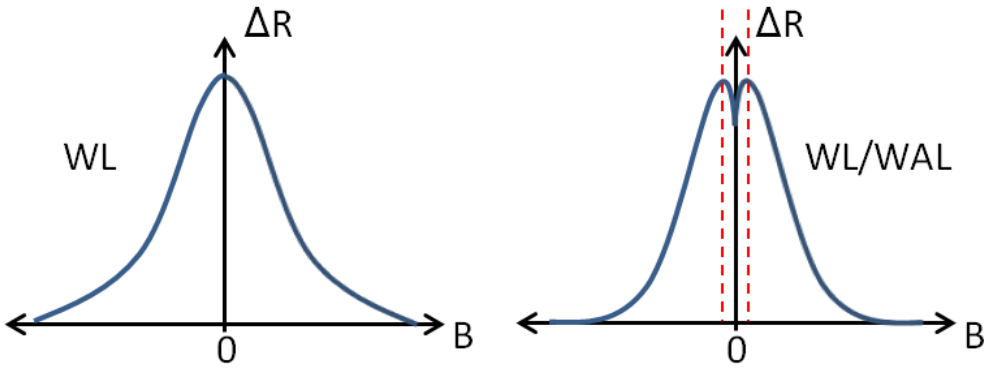

Figure 2.9: Typical shapes of MR curves exhibiting WL (left) and WL/WAL (right). The area of the right curve within the red dotted lines show the positive MR when WAL is dominant in low fields.

Weak Antilocalisation

The SOI can also provide an additional phase difference due to the rotation of spins through Lamour precession. The rotation of spin is opposite for the two path directions in the loop. If the SOI is strong enough, such that the spins rotate more than 2π, the interference becomes destructive [60], thus reducing the probability of back scattering and increasing the conductivity of the material, this is known as weak antilocalisation (WAL). At intermediate fields, the phase difference from the external field shifts the total phase difference into values at which constructive interference takes place and WL becomes dominant, because of this WAL appears as positive MR or a 'dip' at the centre of a WL peak as shown in figure 2.9. This was demonstrated by looking at the low field MR of Mg films coated with varying amounts of Au [60]. It was found that films with low/no amounts of Au exhibited WL, where-as increasing the amount of Au led to an onset of WAL with increasing SO strength. The strengthening of WAL corresponded to an increase in the SO strength (due to the high 'Z' number of Au).

WL/WAL Models

Several theories have been developed that describe the quantum correction of both WL and WAL in the presence of an external magnetic field [62], the most popular is the Iordanski-Lyanda-Pikus (ILP) model [63] which accounts for both $\boldsymbol{k}$-cubic and $\boldsymbol{k}$-linear contributions to the SOI. The model uses three fitting parameters

$$B_\phi = \frac{\hbar}{4eD\tau_\phi} \tag{2.21a}$$

$$B_{SO1} = \frac{\hbar}{4eD} 2\boldsymbol{\Omega}_1^2 \tau_{tr} \tag{2.21b}$$

$$B_{SO3} = \frac{\hbar}{4eD} 2\boldsymbol{\Omega}_3^2 \tau_{tr} \tag{2.21c}$$

where B_ϕ, B_{SO1} and B_{SO3} are the phase breaking and SO (linear and cubic contributions) characteristic fields that can be used to extract τ_ϕ and $\mathbf{\Omega}$. Alternately, the B_{SO} fields can be expressed in terms of τ_{SO} with the same form as equation 2.21a.

These models are only valid for small SO-coupling, such that $\mathbf{\Omega}\tau \ll 1$ and small fields where $l_{tr} \ll L_B$ [63] where L_B is the characteristic magnetic field strength $L_B = \sqrt{\hbar/e\boldsymbol{B}}$. However due to recent advances in growth techniques, 2D structures with both high mobility and SO interaction, both conditions can be invalid due to large values of τ_{tr} (l_{tr}) and/or $\mathbf{\Omega}$. The latter condition defines the diffusion regime which can be alternately expressed as a field limit $B \ll B_{tr}$ in which

$$B_{tr} = \frac{\hbar}{4eD\tau_{tr}} \tag{2.22}$$

Recently a model developed by Golub [64] with the same fitting parameters has been developed for low and high μ and Ω system which is valid in high fields.

Temperature dependence of WL/WAL

The path length at which a spin completes a 2π rotation due to the SOI is called the SO scattering length ($L_{SO} = \sqrt{D\tau_{SO}}$), from this it can be seen that loop paths of length $l > L_{SO}$ contribute to WAL and WAL can only occur when $L_{SO} < L_\phi$. As L_ϕ is dependent on inelastic scattering rates, an increase in temperature reduces L_ϕ. This causes the positive MR WAL correction to reduce with temperature as fewer closed loops have lengths that satisfy the condition $l > L_{SO}$. At higher temperatures when $L_{SO} > L_\phi$, WAL crosses over to WL which also continues to weaken until fully suppressed when L_ϕ falls below l_{tr}.

Initial evidence of WL looked at the temperature dependence of the resistivity of 2D films [65][66][67]. Both WAL and WL exhibit a lnT dependence, with ΔR decreasing linearly for WL and increasing linearly for WAL as demonstrated in Figure 2.10.

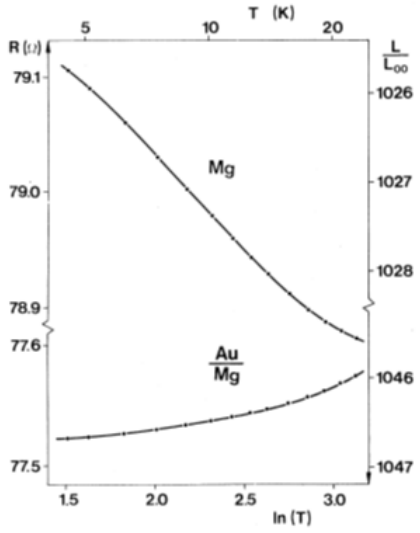

Figure 2.10: The temperature dependence on the resistance for an Mg film exhibiting WL (top) and Mg/Au film with WAL (bottom), taken from reference [68].

2.3 Spin Relaxation

In terms of spin relaxation mechanisms in semiconductors, two mechanisms are often considered the dominant factor in defining τ_s, depending on the type of material. The Elliot-Yafet (EY) spin relaxation refers to the loss of spin polarisation though momentum scattering. This arises from the dependence of spin quantisation axis on $\boldsymbol{k}$ as discussed in section 2.2.1 [50][69][70]. The spin axis for one value of $\boldsymbol{k}$ will differ from another, containing components of spin amplitude perpendicular to the other. When a spin scatters off a phonon or impurity, it will result in a change in momentum ($\boldsymbol{k}$), often resulting in a small rotation or misalignment of the quantisation direction of spin. If the carrier undergoes a number of momentum changing events, the new quantisation direction of spin may have a negative amplitude in the component parallel to its initial spin direction resulting in the relaxation of spin. Understandably, the EY mechanism is dominant in lower quality (low μ) materials where momentum scattering is maximised due to the presence of impurities and dislocations. The effectiveness of EY spin relaxation is also expected to increase with temperature [50], corresponding to an increase in phonon scattering and to a minor

degree, electron-electron scattering. EY-related spin relaxation yields a spin relaxation rate proportional to the momentum scattering rate ($1/\tau_s \propto 1/\tau_m$) [50][70].

The second major contribution to spin relaxation is the Dyakonov-Perel (DP) mechanism which is related to the spin precession induced by the effective field of the SOI. The effective field felt by the carriers is $\boldsymbol{k}$-dependent, $\boldsymbol{\Omega(k)}$. When scattering, the direction and magnitude of $\boldsymbol{\Omega(k)}$ changes along with the direction and frequency of precession. The different planes of precession for different carriers leads to a dephasing of spins, this is enhanced by the different rates of precession due to the varying $\boldsymbol{v}$, and in turn magnitudes of $\boldsymbol{\Omega(k)}$, felt by carriers. Unlike the EY mechanism, the relaxation of spin occurs between momentum changing events instead of the time of collision. An increase in momentum scattering can therefore suppress DP spin relaxation as the time between changes in momentum can be too small for any significant rotation to the spin. It follows that for DP spin relaxation $1/\tau_s \propto \tau_m$ [50][70][69] and therefore is typically suppressed at higher temperatures where EY is more dominant. This mechanism is thought to be the main source of spin relaxation for bulk semiconductors with inversion asymmetry or low dimensional materials with Rashba spin splitting.

Chapter 3

Experimental Techniques

3.1 Growth

3.1.1 Chemical Vapour Deposition

The semiconductor industry routinely uses CVD technology to epitaxially grow high quality semiconductor wafers on a larger scale. CVD growth techniques can employ a wide range of temperatures (200-1600 °C) and pressures, occasionally with the added use of plasma, photons and other methods to enhance growth. All semiconductor material in this thesis was grown epitaxially by Maksym Myronov using an ASM Epsilon 2000E reduced pressure (RP) CVD in a cleanroom environment.

CVD is a common technique used in both research and industry to epitaxially grow crystalline semiconductors with great reproducibility that cannot be matched by molecular beam epitaxy (MBE). The basic process involves flowing precursor gases (compounds used to react and produce the desired material) over a heated substrate, where the precursor can decompose and react to bond with the wafer. The products of the reactions are then carried out of the chamber by a carrier gas. The flow of the precursors and dopant gas is controlled precisely by mass flow controllers. The basic construction of the RP-CVD is shown in figure 3.1. The wafer sits on a susceptor inside an infra-red transparent quartz chamber and the wafer

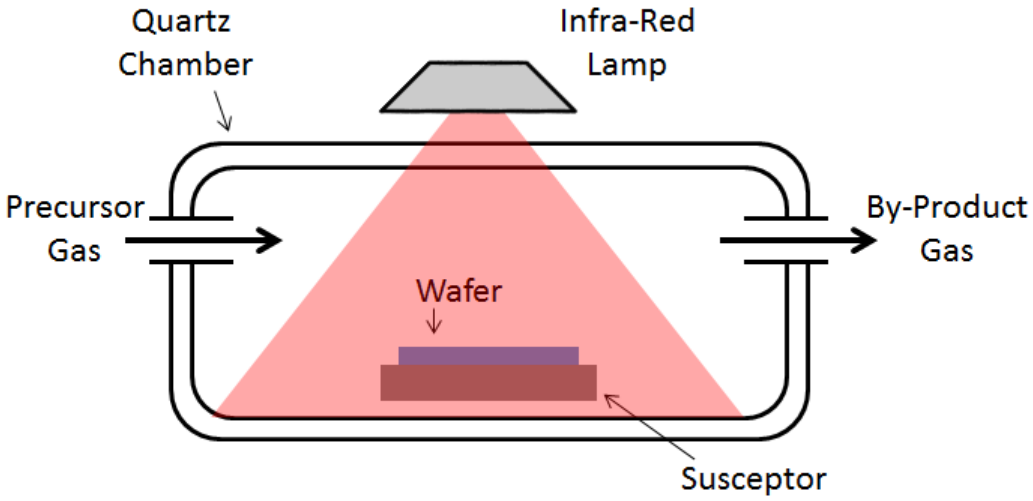

Figure 3.1: A simplified schematic of a CVD during growth.

is heated using infra-red lamps. The heat decomposes the precursors into smaller molecules, some of which are adsorbed onto the surface of the wafer. The remaining unreacted precursor, gaseous by-products and carrier gas are then piped out of the chamber to be processed. The temperature is monitored using thermocouples in the susceptor, and the temperature can be adjusted by altering the power output of the infra-red lamps.

The precursors used for Ge and Si were germane (GeH_4) and di-silane (Si_2H_6). The common chemical process for Ge growth using GeH_4 involves the GeH_4 decomposes into GeH_2 and H2, where GeH_2 is absorbed into the surface. This is described as the following reaction [42]

$$GeH_4(g) + 2* \rightarrow H_2(g) + 2H* + Ge(b)* + 2(b) \tag{3.1a}$$

$$2H* + 2(b) \leftrightarrow H_2(g) + 2* \tag{3.1b}$$

where (g) denotes the gaseous state, $*$ represents a free surface site or a lattice bonded atom when attached to an element. For Si growth with di-silane, the reaction

process is as follows [71][72]

$$Si_2H_6(g) + 2* \rightarrow 2SiH_3* \tag{3.2a}$$

$$SiH_3 * +2* \leftrightarrow SiH_2 * +H* \tag{3.2b}$$

$$2SiH_2 * +2* \leftrightarrow 2SiH * +H_2(g)* \tag{3.2c}$$

$$2SiH* \leftrightarrow 2Si * +H_2(g) \tag{3.2d}$$

Generally, growth rate is dependent on two factors; the temperature, which controls the decomposition of precursors and the rate of flow which dictates the amount of precursor available to absorb. The two factors must be varied interchangeably to achieve the desired growth rate.

3.2 Material Characterisation

3.2.1 X-Ray Diffraction

X-ray diffraction (XRD) is primarily used to determine the lattice parameter of a crystalline material, from this it is possible to extract the composition of heterostructure layers and the degree of strain accurately. In this thesis a Panalytical X'Pert PRO Materials Research Diffractometer was used in XRD measurements, the basic operation of which is illustrated in figure 3.2. Samples are mounted on a stage in an open Eulerian cradle that allows full rotation along the z axis ($-180° < \phi < 180°$) and the x axis (-90°$< \psi <$90°). The stage itself may also move in both x and y directions for the probing of multiple areas/samples. The x-ray source and detector rotate about the y axis such that the angles ω (incident angle) and 2θ (the angle between incident and scattered beam) are accurately controlled.

The x-ray source uses a Cu anode at 45 kV (40 mA) to generate CuKα_1 of λ =1.5406 Å. Before reaching the sample, the x-rays are collimated and passes

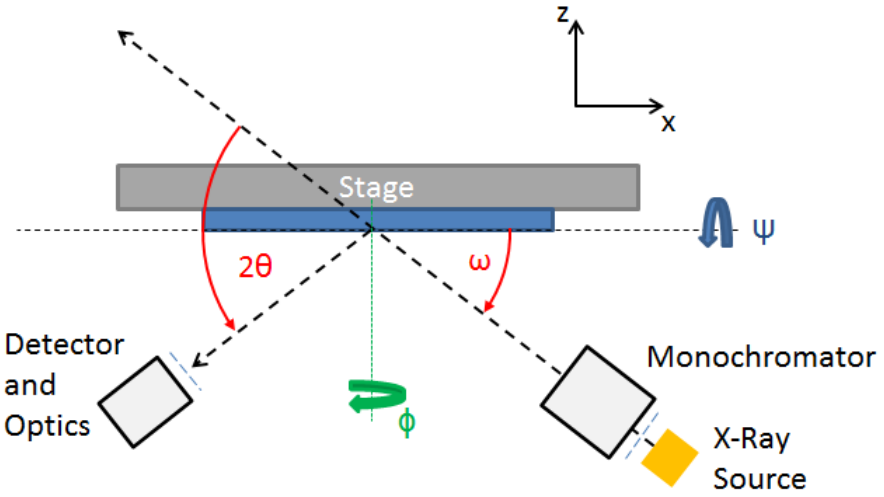

Figure 3.2: A simplified diagram of a typical x-ray diffractometer set up.

through a Ge 2-crystal, 4-reflection (220) Bartels monochromator which selects the beam energy by allowing diffraction of the beam by a specific crystal plane between two pairs of parallel Ge crystals [73]. Once scattered the beam enters a collimator slit and through a Ge crystal and onto the detector itself. The collimator slit once again reduces the angular acceptance, whilst the Ge crystal serves to specify the particular wavelength that can be detected by the Xe proportional detector. To prevent damage from high intensities, an attenuator positions an Ni plate in front of the monochromator when a threshold is reached.

Reciprocal Lattice and the Bragg Condition

The crystal lattice is often described in terms of reciprocal lattice space, which is the Fourier transform of the regular lattice. The result is a coordinate system which describes a crystal lattice plane. The reciprocal lattice axis vectors, $\mathbf{b_i}$ are given by

$$\mathbf{b_1} = \frac{\mathbf{2}\pi(\mathbf{a_2} \times \mathbf{a_3})}{\mathbf{a_1} \cdot (\mathbf{a_2} \times \mathbf{a_3})} \tag{3.3a}$$

$$\mathbf{b_2} = \frac{\mathbf{2\pi(a_3 \times a_1)}}{\mathbf{a_2 \cdot (a_3 \times a_1)}} \tag{3.3b}$$

$$\mathbf{b_3} = \frac{\mathbf{2\pi(a_1 \times a_2)}}{\mathbf{a_3 \cdot (a_1 \times a_2)}} \tag{3.3c}$$

For cubic unit cells, this reduces to $\mathbf{b_i} = \mathbf{2\pi/a_i}$. Miller indices (hkl) are used to indicate the specific crystal planes which are orthogonal to $h\mathbf{b_1} + k\mathbf{b_2} + l\mathbf{b_1}$. Bragg's law describes the condition for which diffraction can occur and is given as

$$2dsin\theta = n\lambda \tag{3.4}$$

where d is the separation between parallel planes, θ is the angle of incident radiation and n is an integer. When this is satisfied the scattered photons interfere constructively to form Bragg peaks.

$\omega - 2\theta$ -Scan and Reciprocal Space Maps

The most basic measurement used is a coupled $\omega - 2\theta$ scan, or rocking curve. For a rocking curve the sample is rotated about the y-axis by an angle; such that ω and 2θ are kept at a constant ratio of 1:2, as this degree of stage rotation is not possible on the Panalytical diffractometer, in which the angles ω and 2 are kept at a constant ratio and scanned about different ω values. This is achieved by rotating the sample stage (about the y-axis) and detector simultaneously to maintain a constant $\omega - \theta$ ratio.

For a measurement, the source and detector are centred about a known Bragg peak of a chosen reflection and $\omega - 2\theta$ are scanned around this peak. For the samples measured in this thesis the symmetrical Si (004) peak from the substrate is chosen, the resulting peaks will be dependent on the out of plane parameter a_z of the various layers, which will differ with both the composition and strain of the layers. The $\omega - 2\theta$ scan is typically used to confirm the crystallinity of a layer and give rough indication of the number of different compositions in the

heterostructure. Additionally, high quality layers can produce thickness fringes due to photons reflecting off the upper and lower surface of the layer before leaving the sample to interfere and produce the fringe pattern. The separation between fringes will be larger for thinner layers, however this is typically only visible for fully strained layers as dislocations associated with relaxations hinder reflections.

Reciprocal space maps (RSM) can be collected by combining different $\omega - 2\theta$ scans with different offsets between ω and 2θ. The area which can be probed by the diffractometer is determined by λ and ω and is illustrated in figure 3.3. Firstly $\omega/2\theta < \lambda/2$ and secondly by the physical restraints of ω (photons are incident from the back of the sample when $\omega < 0$ and scattered photons exit the back of the sample at $\omega > 2\theta$). The studies in this thesis employs RSM scans of the symmetric (004) and asymmetric (224) reflections.

ω and 2θ are converted into reciprocal space using [74]

$$q_z = \frac{\lambda}{2} sin\theta cos(\omega - \theta) \tag{3.5a}$$

$$q_x = \frac{\lambda}{2} sin\theta sin(\omega - \theta) \tag{3.5b}$$

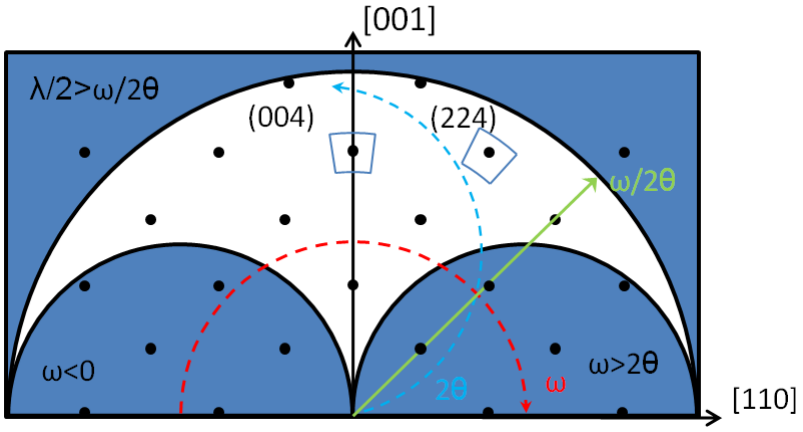

Figure 3.3: A diagram revealing the accessible Bragg reflections for a (001) grown crystal. The arrows indicate the scan movements for shifting values of $\omega, 2\theta$ and $\omega/2\theta$. Adapted from [73].

Like the (004) coupled scan, a (004) RSM allows the extraction of a_z as well as the tilt of epitaxial layers with respect to the substrate. With a (224) scan it is possible to extract both a_x and a_z. In this case $a_x = 2\sqrt{2}/q_x$ and $a_z = 4/q_z$. Once both these parameters are known, both the composition and strain of the layer can also be determined with equations 2.1, 2.3, 2.4.

Figure 3.4 gives an example of (004) and (224) RSM scans for a Ge quantum well on a reverse graded $Si_{1-x}Ge_x$ buffer, in which the composition 'x' is gradually changed from $x = 1$ to a smaller value. The RSM can be interpreted as follows, peaks on the right (top) will have smaller a_x (a_z) values. In these heterostructures, the Si substrate is fully relaxed as well as the Ge buffer layer due to the relativity

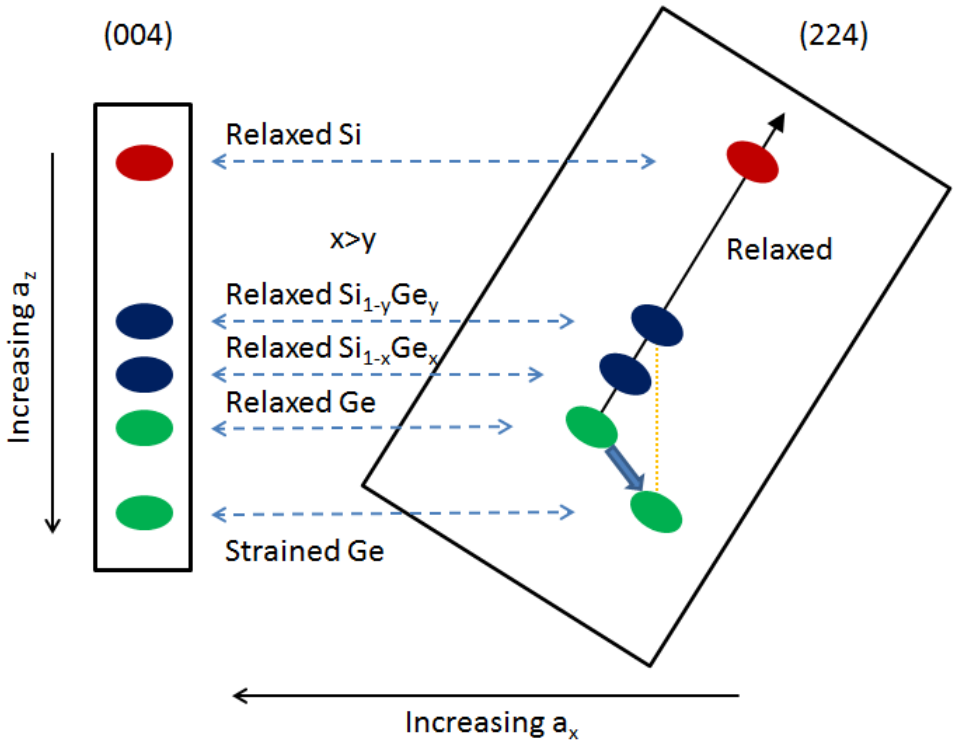

Figure 3.4: An illustration of (004) and (224) RSMs of a Ge quantum well strained to a graded SiGe buffer. The SiGe peaks with Ge concentrations such that x>y are fully relaxed and thus positioned between the relaxed Si and Ge peaks. The strained Ge quantum well peak is fully strained to the $Si_{1-y}Ge_y$ and thus shifts to match a_x and whilst increasing a_z.

large thickness of the buffer compared to its critical value, it follows that the $Si_{1-x}Ge_x$ alloy layers that lie on the line between the relaxed Si and Ge peaks are also fully relaxed. When a layer is strained, in this case the Ge quantum well, the a_x value of this layer will shift towards the value of that of the (virtual) substrate, matching it when fully strained. The quality of the epilayers measured in XRD can also be indicated by the width of the peaks, with diffuse scattering from defects causing the peaks to broaden.

3.2.2 Transmission Electron Microscopy

Electrons allow us to surpass the resolution limitations of optical microscopes set by the wavelength of visible light. The wave particle duality gives electrons an effective wavelength determined by the energy of the electron ($\lambda = h/p$). Transmission electron microscopy (TEM) is a powerful technique often used to take cross-sectional images of structures and devices from the micron scale down to lattice resolution. This is particularly useful for confirming the crystallinity, quality and thickness of layers in heterostructures post growth or processing. The TEMs employed in this study are the Jeol JEM-2000FX, capable of down to nm resolution and the Jeol JEM-2100 with lattice resolution capabilities.

TEM requires the sample of interest to be thin enough for the majority of electrons directed towards the sample to be able to pass through the material. The electrons that pass through the sample are then either projected onto a florescent screen or CCD to form an image.

Sample Preparation

The studies covered in this thesis use cross-sectional images of either heterostructures or deposited materials and thus required substantial sample preparation to thin the sample to a thickness suitable for TEM. The preparation method used a combination of mechanical grinding/thinning and ion beam milling/polishing to

achieve electron transparency.

The size of the sample used is typically two of 15 mm by 5 mm sized sections of wafer which is cleaned using acetone. The surface of the two wafers are bonded together using Araldite epoxy, the two pieces used can either be the same sample or two significantly different structures so long as they are distinguishable from each other when viewing in the TEM. A piece of Si wafer of the same size is then bonded to the substrate sides of the sample. These plain wafer pieces are to serve as structural support in the later stages of preparation, to prevent the slice of sample(s) from collapsing.

The stack of wafers are then mounted on its side onto a Cu block using wax and ground down (such that the width of the stack is reduced) to typically $\sim$0.5 mm. The grinding is performed using a series of SiC grinding papers with different coarseness. The coarseness of the papers is reduced such that the first three are used to grind down and smooth the sample and the remaining two are used to polish the surface. The final thickness of the ground down stack is determined by the thickness of glass square slides placed around the sample on the copper block. These are primarily used to ensure the sample is ground down evenly and to a satisfactory thickness. The stack is then transferred to a glass slide with the smoothed surface facing down. The grinding process is then repeated to the untouched side of the stack until to a thickness typically on the micron scale.

The sample holders for the TEMs used with these samples accept 3.05 mm diameter Cu rings with a 2 mm by 1 mm slot/window. A number of these rings are glued to the thinned sample stack such that the sample/sample interface of the stack runs through the centre of the slot, perpendicular to the long edge. The excess material outside the rings are removed using a scalpel, the rings are then lifted off the surface of the glass slide by gently heating the adhesive wax before bathing the rings in a warm acetone bath for the complete removal of wax from the material.

The final thinning process employs a precision ion-beam polishing system

(PIPS), in which two focused Ar ion beams are directed at shallow angles (2.5-5 °) along the sample/sample interface in a high vacuum environment (10^{-6} mbar). The process is complete when a pit forms along the majority of the surface, leaving the ends of the pit thin enough for TEM.

Alternately a focused ion beam scanning electron microscope (FIB-SEM) can be used for sample preparation. This technique involves the use of a focused ion (Ga) beam to cut a thin wedge shape into the sample material. The top of the wedge is attached to a probe tip by deposition of C on the surface and the tip. The FIB is then used to cut the bottom of the wedge from the rest of the sample, such that the wedge can now be lifted free. The sample is then attached to a sample holder by C deposition and the probe is then cut free. The wedge must be cut thin enough for the material to be electron transparent. Care must be taken during the process to prevent significant damage and ion implantation from the FIB to the sample. The top-most layers are often protected by depositing a metal cap on the surface of the sample. FIB-SEM sample preparation in this project was performed by Gerard Colston.

TEM Equipment Operation

A TEM consists of a column containing (from the top) an electron gun followed by a series of electromagnetic lenses (quadra or hexapole magnets), apertures, sample stage and a phosphorescent screen/CCD, as depicted in figure 3.5. The electron gun is used to source the electron beam, typically using either thermionic emission or field electron emission and an anode is used to accelerate the emitted electrons towards the sample and down to the bottom of the column with an acceleration voltage on the order of 200 kV. The beam formation is aided with a Wehnelt cup used to initially focus the electrons.

The first series of lenses are known as the condenser lens, used to focus the beam into the condenser aperture, which limits the width and intensity of the

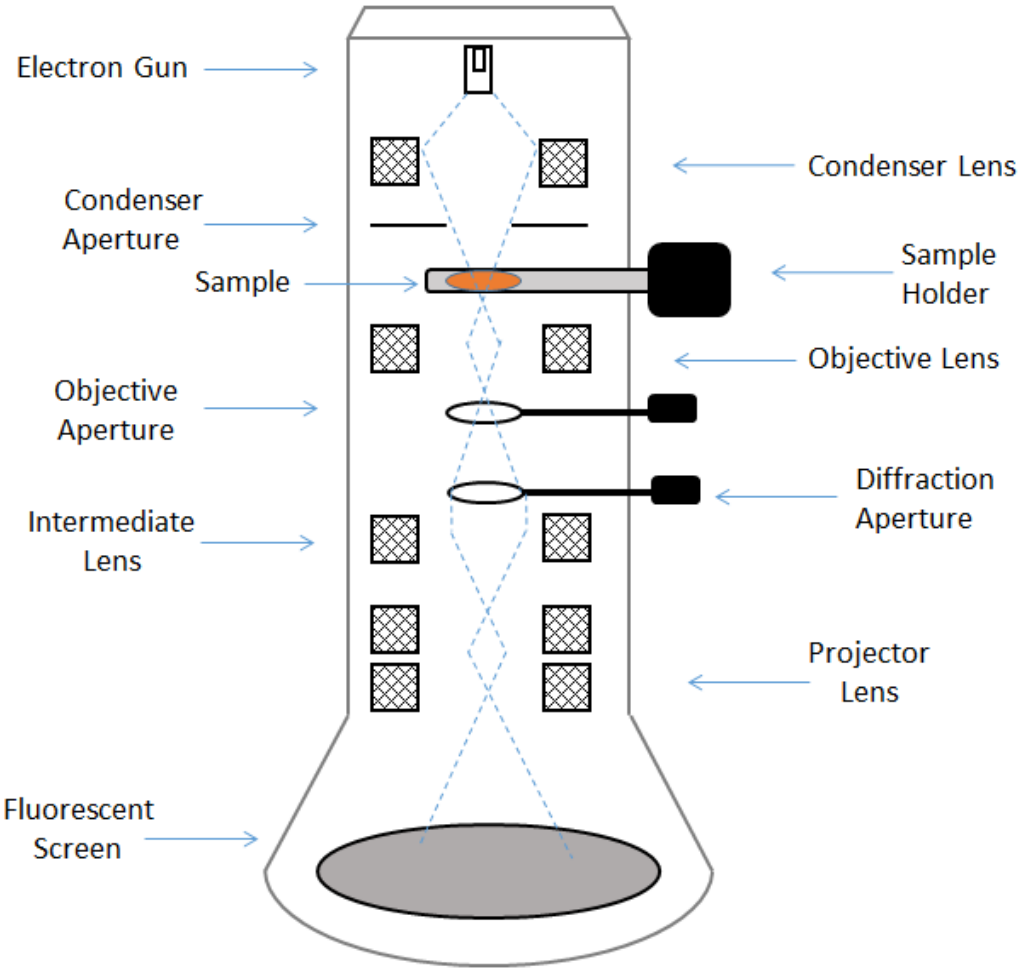

Figure 3.5: A simplified schemaic of a TEM column.

beam. The beam then passes through the sample at the centre of the column before reaching the objective lens at which the beam is expanded to magnify the image projected by the sample. A series of additional lenses are used to correct for aberrations and adjust the orientation of the image onto the viewing stage which is an interchangeable system between a phosphor screen (used for focusing and positioning the image) and CCD for image capture. The column is kept under high vacuum ($<10^{-7}$ mbar) to prevent unwanted interaction with air molecules.

3.2.3 Imaging Modes

Bright field (BF) imaging is the most commonly used imaging mode in TEM, where the image contrast is dictated by the absorption of electrons through the sample. High absorption areas correspond to either thicker areas of the sample or higher 'Z' numbered atoms, resulting in darker areas in the image.

Rotating the sample using a multi-axis stage allows for the diffraction condition of different planes to be achieved. Diffraction imaging employs the use of additional apertures to exclude and include the electrons diffracted by a chosen crystallographic plane. The back focal plane is the point at which the electrons leaving the sample parallel with each other meet at a single point, in the TEM column, this corresponds to electrons diffracted from a particular plane. Adjusting the power of the objective lens, such that the back focal plane now lies on the viewing screen, results in a pattern of dots corresponding to the different exit angles of the electrons and thus different crystallographic planes that satisfy the Bragg condition. The sample is tilted such that two spots are included, the straight through beam (000) and the desired reflection plane.

BF imaging in diffraction mode uses the diffraction aperture to allow the straight through image through whilst blocking the second spot, causing the electrons reflected from the chosen plane to be blocked and appear dark in the image. Dark field (DF) blocks the (000) reflected electrons, producing an image with areas not within the crystallographic plane to appear dark.

In this thesis I have used the (004) and (220) conditions for imaging layers. The (004) plane is typically used for thickness measurements of layers points along the interface planes, where as the (220) plane is used to highlight dislocations. Dislocations in diamond structures can form at either 0°or 60°to the (110) plane [75], the deformation of the crystal due to these dislocations thus appear as contrast in the (220)-condition micrograph.

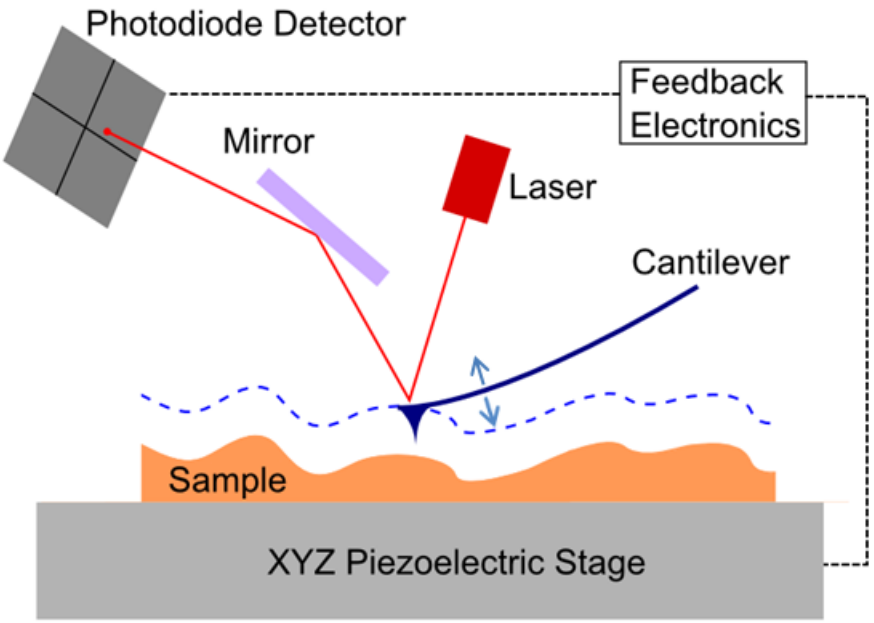

Figure 3.6: A simplified AFM set up.

3.2.4 Atomic Force Microscopy

Atomic force microscopy (AFM) is a technique used for analysing the topography of a material. The surface roughness of a material can be an indicator of the quality of the material, furthermore the roughness of the surface can also affect device fabrication and operation, particularly when dealing with surface/interface sensitive processes, such as quantum tunnelling.

Figure 3.6 shows a simplified AFM set up. A typical AFM consists of a tipped cantilever (AFM tip) which is placed either in contact or close to the surface of the sample. The sample rests on a two-axis piezoelectric stage, used to move the sample and raster the scan. A laser is focused onto the cantilever and the reflected spot is aligned onto a photodiode detector. Changes or deformations on the cantilever are tracked by looking at the motion of the laser spot on the detector.

In the studies covered in this thesis, two types of measuring modes were used, contact and tapping mode. In contact mode the tip is lowered close to the surface

such that the tip is held down onto the surface. As a raster scan is performed, the tip deforms to the shape of the topography and the deformation is recorded an interpreted into an image. Alternately, a feed-back loop can be used to keep the deformation constant, thus using the feedback signal to form the image.

Tapping mode was originally demonstrated by Zhong et al [76] to avoid damage to soft sample surface. In tapping mode, the tip is oscillated at its resonant frequency and kept close to the surface of the sample. As the tip is scanned across the sample, the Van der Waals force between the tip and the surface changes significantly with the separation of the trip. This in turn changes the amplitude of the oscillations. Like the deformation of the tip in contact mode, the amplitude is kept constant by sending a feedback signal to the piezoelectric stage. Tapping mode is typically used for smoother samples with a root mean square (RMS) roughness below 1 nm, as the tip can find it difficult to recover its amplitude after encountering a large feature, producing stripe like artefacts.

3.2.5 Secondary Ion Mass Spectroscopy

Secondary ion mass spectroscopy (SIMS) is a material characterisation technique which is used to identify the elemental composition of a sample and produce an elemental depth profile. Although compositional analysis with SIMS is not as accurate as XRD, SIMS has an additional advantage of not requiring the sample to be crystalline and can detect elements at relatively lower concentrations. This was particularly useful for the analysis of dopants and impurities of which are typically too low in concentrations to produce pure/alloy Bragg peaks or cause a shift in Ge or $Si_{1-x}Ge_x$ peaks due to induced strain. Depending on the target material, the background can be between 10^{12}-$10^{16}\,cm^{-3}$. In addition to dopant and impurity analysis, SIMS was also used to map $Si_{1-x}Ge_x$ concentrations in more intricate heterostructures.

In SIMS, an ion beam is targeted at the surface of a material to sputter and

ionise the surface. The resulting ejected secondary ions from the material are then collected and identified using mass spectroscopy to measure the mass/charge ratio. The equipment consists of an ion gun and a series of ion lens to focus the beam onto the sample. The source used for the beam of ions is dependent on the type of material used, such as the use of O ions for electropositive ions (B ions) and Cs for electronegative ions (P ions), beam size and current. The ejected ions are then guided to a mass spectrometer via a second series of ion lenses, before reaching a detector such as a Faraday cup or electron multiplier.

This technique is particularly useful in combination with XRD which provides accurate information on lattice parameters (and therefore composition) and TEM which can provide information on layer structures and thickness. Although the latter techniques are more accurate in these types of measurements, the compositions extracted from XRD are not easily matched with the layer structure identified in TEM micrographs, particularly when the image contrast is determined by the 'Z' number of the atoms (which differs only slightly between variations of Si:Ge ratios) as well as the thickness of the prepared sample. The compositional depth profile obtained in SIMS can therefore be matched with the layer and composition information from TEM and XRD to produce a complete understanding of the sample structure.

3.2.6 X-Ray Photoelectron Spectroscopy

X-ray photoelectron spectroscopy (XPS) is a surface sensitive technique able to probe and quantify the elements found close to the surface of a material. XPS relies on the photoelectric effect in which the absorption of a photon by an atom is used to eject an electron with a work function smaller or equal to the energy of the photon (hf). Knowing the frequency of the photon (simply by using a known specific wavelength) and measuring the kinetic energy (E_K) of the ejected electron allows the calculation of the binding energy (E_B) of the electron prior to ejection

due to the conservation of energy. In practice, the work function of the electron detector (ϕ_{SP}) must also be taken into account, the expression used to extract E_B is given in equation 3.3.

$$E_B = hf - E_K - \phi_{sp} \tag{3.3}$$

The binding energy of an electron is specific to the element and shell/state, thus the resulting binding energy spectra can be used to identify the elemental composition of the sample. In addition to the photoelectrons ejected in the process, Auger electrons are also given off, due to the excess energy resulting from an outer shell electron dropping to fill the new vacancy left by the photoelectron. As with photoelectrons, Auger electron peaks in XPS spectra are identifiable by their signature energy, spectroscopy which concentrate on the analysis of these peaks is known as Auger electron spectroscopy.

The depth at which the material is probed is limited by the inelastic mean free path (λ_i) of the photoelectrons, as loss of kinetic energy results in inaccuracies when calculating E_B. The probing depth is thus defined as the depth at which 95% of emitted electrons are scatted by the time they reach the surface of the material (typically $3\lambda_i$). The probing depth is also controlled by the angle of incidence for the x-ray photons, using shallower angles increases the sensitivity of the measurement to the upper-most layers of the material.

XPS Experimental Set Up

To allow for accurate determination of E_K, XPS is conducted under ultra high vacuum (UHV) to prevent energy loss via scattering off atmospheric particles. A typical basic XPS set up (given in figure 3.7) consists of an x-ray source, often Al K_α (1486.6 eV) or Mg K_α (1253.6 eV), an electron energy analyser and an ion gun used for sample cleaning or sputtering. In this study, an Omicron XPS and Kratos

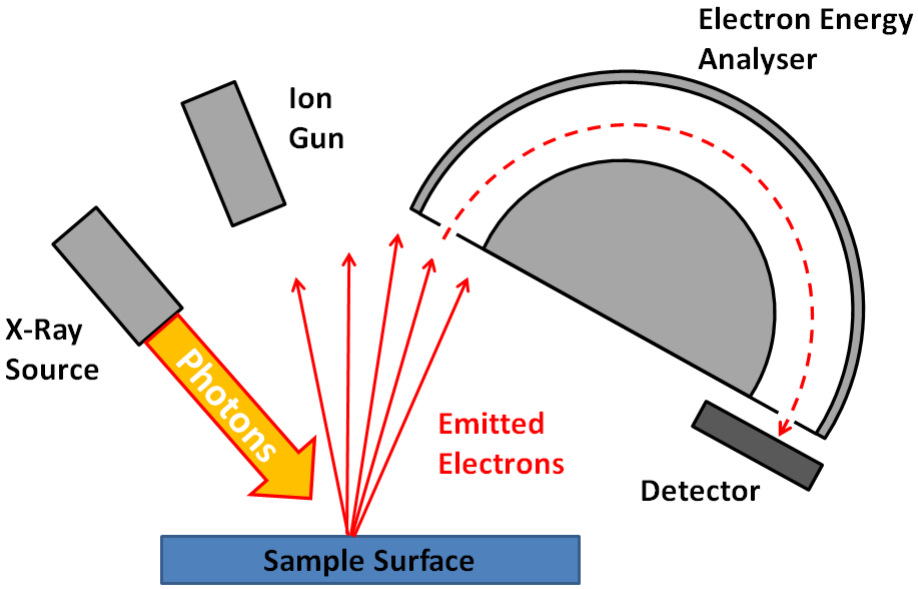

Figure 3.7: A simplified XPS experimental set up.

XPS systems were used.

Peak Identification

A large amount of published experimental data makes it possible to identify peaks by comparing the binding energy with known experimental data. Furthermore the SOI can also cause a noticeable spin splitting in the binding energy for some states. The energy splitting between the spin-split peaks as well as the relative intensities between the two spin peaks are again specific to the electron state for each element and is well documented. The relative peak areas of the spin-split peaks (I_{j+}/I_{j-}) is given by equation 3.4 where j is the total angular momentum ($l+s$) and the +/- refer to the sign of the spin, s.

$$\frac{I_{j+}}{I_{j-}} = \frac{2j_+ + 1}{2j_- + 1} \tag{3.4}$$

Chemical composition of the sample may also be inferred by the position

of the elemental peaks. As the binding energy is dependent on the electrostatic interaction of the electron and the positive nucleus, if the atom is bonded to another element a shift in the binding energy occurs due to the removal or addition of an electron. In oxidation, a valence electron is donated to the O atom, with the removal of an electron from the element's valence band there are fewer electrons to screen the positive charge of the nucleus from other electrons, thus increasing the binding energies. Like the elemental peaks, chemical shifted peaks are also well documented allowing the identification of various chemical bonding.

The concentration of elements in spectra are related to the peak intensity or rather the area under the elemental peak. The concentration is simply the ratio of intensity for the element in the sample to the ratio of the peak for the pure element. This is impractical due to the large database required, instead sensitivity factors S_x, defined as the relative intensity of an element for a single known standard such as Ag. The concentration, can thus be determined using

$$C_x = \frac{I_x/S_x}{\sum_i (I_i/S_i)} \tag{3.5}$$

where I_x and S_x are the intensity and sensitivity factor of the element of interest and the denominator is the summation of I/S ratios for the remainder of the elements in the sample. The XPS spectra and concentration analysis in this thesis was processed using the CasaXPS program.

3.3 Fabrication

A number of devices have been used throughout this thesis to conduct electrical measurements on grown material. The devices used were fabricated in-house using a number of techniques described in this section.

3.3.1 Optical Lithography

Optical lithography is a fabrication technique used to produce micron scale features for devices. The process involves transferring a polymer (resist) pattern onto a wafer through the using a mask and UV exposure. This patterned resist is then used as a stencil for deposition of etching processes used to fabricate micro devices.

Before lithography, the sample surface is rinsed with a primer to clean the surface and improve resist adhesion. The resist is dripped onto the sample, to completely cover the surface. Uniform spreading of the liquid resist is achieved by spinning the sample, the speed used also determines the thickness of the resist layer. This is then solidified by baking the sample on a hot plate. The desired pattern is transferred onto the resist, by placing a quartz and chrome mask containing the pattern over the sample and exposing the surface not covered by the chrome covered pattern to UV light. The UV light can either strengthen or weaken the polymer bonds depending on whether the process is negative or positive. Submerging the wafer in a 'developer' solution removes the weaker resist, to form the final patterned surface, ready for material deposition or etching. Additional flood exposures and baking may also be used for some resists for the formation of undercuts in the patterned resist. This is typically used to prevent deposition onto side walls which can cause problems in lift off. The general schematic for optical lithography is given in figure 3.8.

3.3.2 Deposition Techniques

Deposition of metals and oxides in this project were preformed by either sputtering, electron beam evaporation or thermal evaporation. Deposition typically requires low pressures ($<10^{-6}$ mbar) to prevent the incorporation of impurities into the evaporated layer. The surface of the material receiving the evaporated metal must also be cleaned by either limited sputtering or submersion in a weak acid to remove surface impurities or native oxides. During deposition, a crystal monitor can be used to

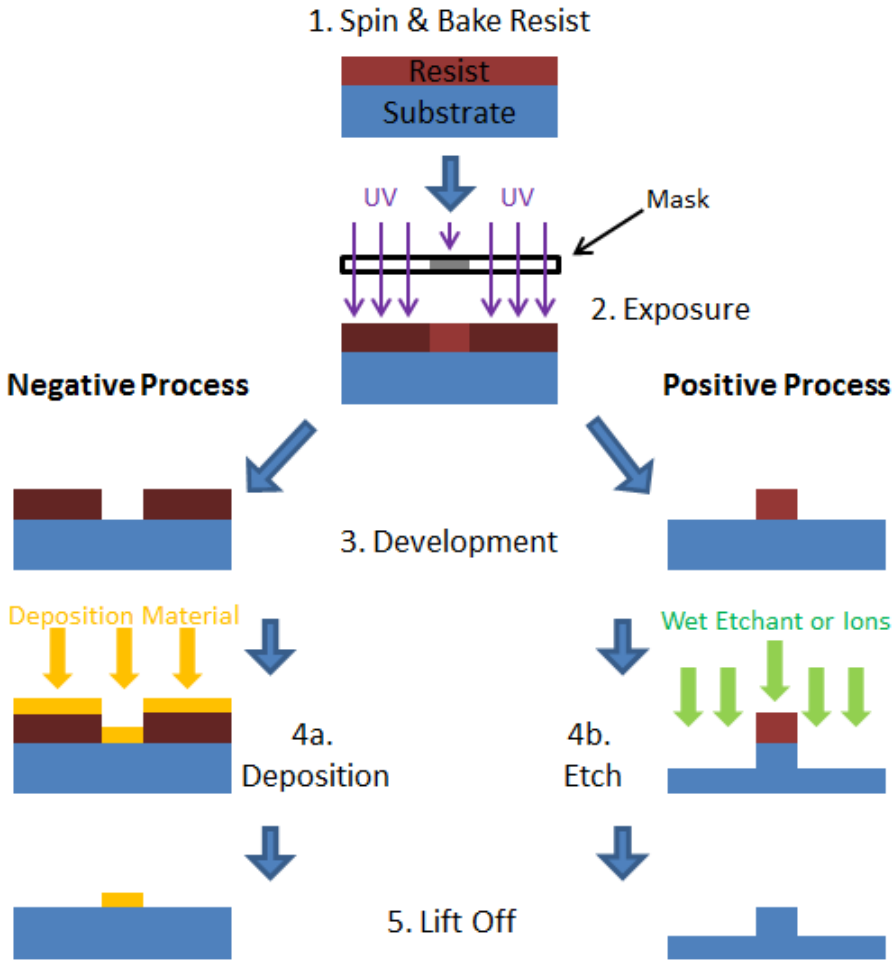

Figure 3.8: A demonstration of a negative process typically used for metal contact deposition and positive lithography process used for defining a mesa.

measure the thickness of the deposited layer in-situ and achieve precise thicknesses.

Evaporation

In thermal evaporation, the target material is placed in a W or alumina crucible and the patterned substrate is mounted directly above. A shutter is positioned between the target material and the substrate. Once the chamber is at the appropriate pressure, a current is passed through the crucible to induce Joule heating of the filament/crucible and the target material. Typically the current is ramped up

gradually until the desired deposition rate is reached to prevent flash evaporation of the target material. Typically, the shutter is held in place for a short amount of time once the desired deposition rate is reached, to allow the evaporation of any contaminants on the surface of the target material. Deposition onto the surface of the substrate is initiated and stopped by operating the shutter. Thermal evaporation is limited by the melting point of both the target material and the crucible. The thermal evaporator did not facilitate multiple sources and was not fitted with a crystal monitor, for this reason it was used to deposit single layer metallic contacts where thickness was not important.

Electron-beam evaporation follows a similar procedure, instead of Joule heating, an electron gun is used to fire a beam of electrons and accelerate them onto the target material to produce heat. The e-beam evaporator contained multiple sources and had a minimum deposition rate of 0.1 $\text{Å}\text{s}^{-1}$. This technique was used for thin film deposition and multilayer depositions to minimise contamination between deposited layers. Both electron beam and thermal evaporation typically produce amorphous samples when evaporating oxides.

Sputter Deposition

The basic concept of sputter deposition is the acceleration of ions towards a target material in order to knock the target atoms free, to be deposited onto a substrate, this is illustrated in figure 3.9. In a sputterer, the target material is placed on a cathode, whilst the substrate is mounted opposite to the target on an anode. A small amount of inert gas is released in the vacuum chamber and ignited into a plasma. The ions in the plasma are accelerated towards the cathode and collide with the target. The transfer of kinetic energy ejects the neutral target atoms which proceed to travel in straight trajectories and deposit on the substrate. A magnetron sputterer uses magnets situated under the cathode to confine the free electrons in spiral like paths above the target to encourage the re-ionization of the plasma gas

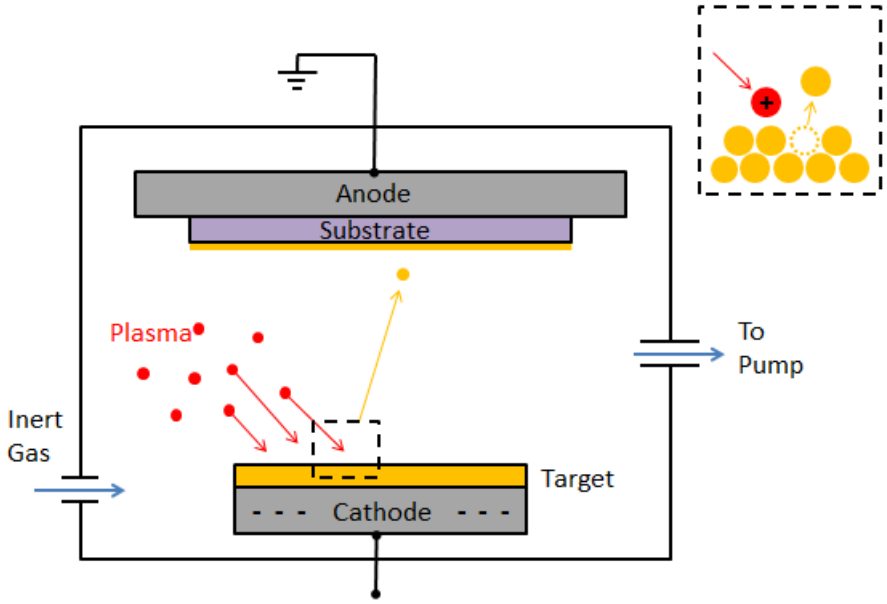

Figure 3.9: A simplified diagram of DC sputtering deposition. The insert shows the ejection of a target atom after the impact of an ion.

and enhance sputtering rates.

The process described is defined as DC sputtering, which is not effective for insulating materials as a positive charge can build up on the target material and oppose the motion of sputtering ions, instead insulating films are deposited using radio frequency (RF) sputtering. RF sputtering alternates the potential (on the order of MHz) of the cathode such that the positive charge build-up can be dissipated on the reversal of the cathode.

3.4 Electrical Characterisation

Material characterisation is limited to assessing the physical properties of samples, providing no information on the motion of electrical carriers in the system, required for application in devices. A number of types of devices can be fabricated using the material of interest to directly measure important electrical properties such as the number of electrically active carriers, the conductivity (σ) of materials and the

mobility (μ) of carriers. This type of information is crucial for extracting other parameters such as characteristic times and lengths which define the length scales at which electrical devices can operate.

3.4.1 Cyromagnetic Systems

Cryomagnetic systems were used in this thesis which allowed electrical measurements to be performed over a wide range of temperatures in the presence of perpendicular magnetic fields.

Closed Cycled Cryostat

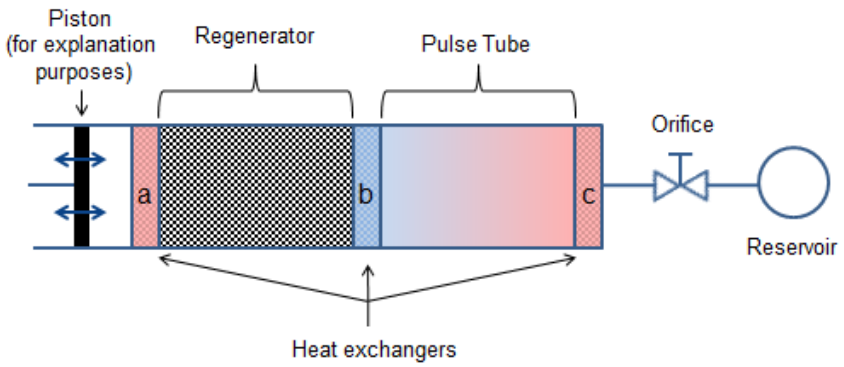

Figure 3.10: A simplified diagram of a pulse tube refrigerator, the compressor is replaced by a piston for explanation purposes.

Two closed cycled cryostat (CCC) systems were employed, one operated over a range of 14-300 K and could apply a perpendicular magnetic fields of intermediate strengths (<1 T). This CCC uses a pulse tube refrigerator (PTR) as a cooling mechanism and a He^4 compressor to recycle and cool the He^4. A simplified PTR schematic is given in figure 3.10, consisting of three heat exchangers ('a', 'b' and 'c'), of which 'a' and 'c' are in thermal contact with the surroundings and 'b' is cool and in thermal contact with a stage. Between 'a' and 'b' is a regenerator, a metallic mesh which maintains the thermal gradient between 'a' and 'b'. The compressor acts like a piston, compressing or expanding the gas in the PTR. As the gas is com-

pressed it attempts to pass through 'c' and an orifice into a reservoir. The limited gas flow into the reservoir causes the gas to heat adiabatically, passing the excess heat through heat exchanger 'c'. When the gas moves into the opposite direction, the reduction of pressure leads to the cooling of the gas. The gas in the vicinity of heat exchanger 'b' becomes cooler than the heat exchanger and thus draws heat from the stage through 'b', cooling the stage on which a sample is loaded. The temperature is varied by applying heat to the sample stage from an electronic heater, whilst the temperature is monitored using a Cernox temperature sensor calibrated for use in magnetic fields in the temperature range 0.1-320 K.

Multi-Stage He^3 Closed Cycle Cryostat

A second cryomagnetic system, an Oxford Instruments Heliox AC-V was used for lower temperatures (0.3-300 K) and high magnetic fields (<12 T). He^3 systems can reach down to ∼1.2 K. A diagram of the Heliox AC-V system is given in figure 3.11.

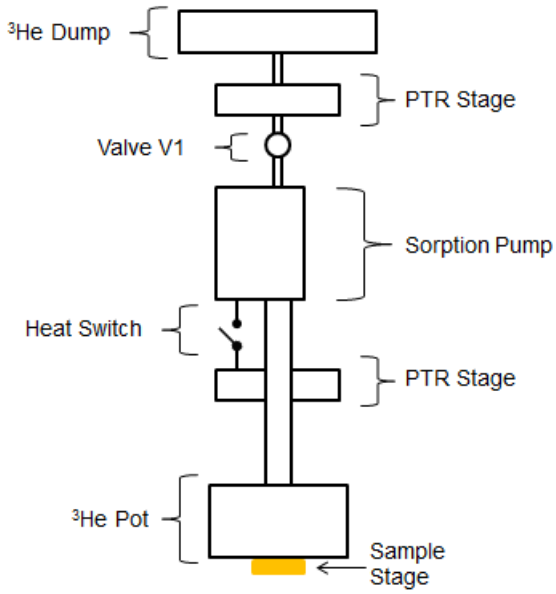

Figure 3.11: A simplified diagram of the Heliox AC-V multi-stage CCC, adapted from the Oxford Instruments operators manual.

Above 3 K, the cryostat operates by using the PTR stages to cool the wiring and He^3 and a heater for temperature control whilst leaving valve between the dump and the pot open. Lower temperatures are reached using the adsorption pump to reduce the pressure in the He^3 pot. The process begins by opening the heat switch (which thermally links the second PTR stage with the adsorption pump) and heating the adsorption pump to 40 K, releasing any absorbed He^3 from the pump. The PTR stages cool the He^3, which is further cooled by opening the valve, 'v1' to allow expansion into the dump and encouraging condensation of He^3 into the pot. After 30 minutes, the dump is sealed once again and the heat switch is closed to cool the adsorption pump to 15 K. At 15 K the adsorption pump adsorbs the remaining He^3 gas reducing the pressure and cooling the pot down to base temperature.

The sample stage is located at the end of the pot with a Cernox temperature sensor and heater for temperature control. The insert can be lowered into a superconducting which can supply a perpendicular field up to 12 T. The system is also set up with a number of lockins, source meters and volt meters to accommodate low field AC and DC measurements.

3.4.2 Hall and Resistivity Measurements

Hall measurements are a powerful tool for semiconductor characterisation, yielding information on the resistivity, carrier density and mobility of the material as well as exhibiting different interesting phenomena such as WL/WAL, SdH and the integer/fractional quantum Hall effect in low dimensional materials.

The Hall effect is the creation of a transverse potential difference (V_H or V_{xy}) to an electrical current (I_x) on the application of a perpendicular magnetic field (B_z). This arises from the Lorentz force experienced by the charge carriers due to B_z. This force is perpendicular to both current and B_z, causing the oppositely charged carriers to deflect to opposite ends of the material and accumulate as depicted in figure 3.12. The accumulation of charge produces an electric field (E_y) to

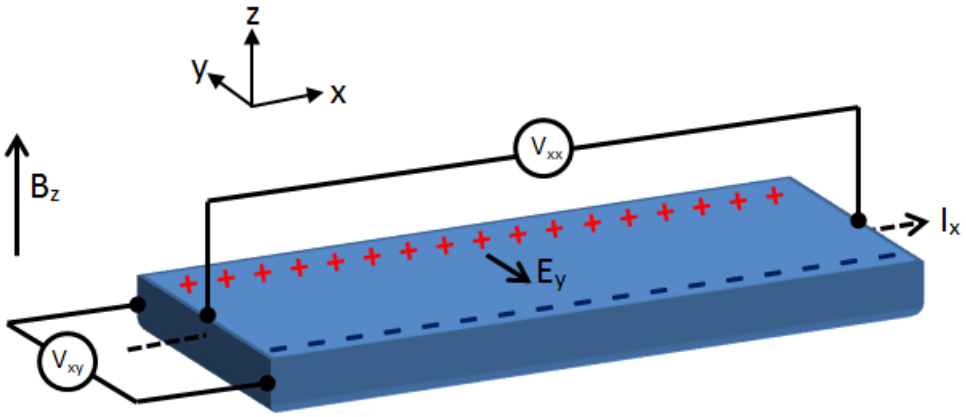

Figure 3.12: A schematic diagram of the Hall effect. The perpendicular magnetic field induces a Lorentz force which causes charge carriers to accumulate at the edges of the bar, thus producing a Hall voltage given here as V_{xy}.

oppose the Lorentz force and allow the current to flow.

For a material in the shape of a bar with the current applied along the x-axis as seen in figure 3.12, the sheet resistivity ρ_{xx} is given by

$$\rho_{xx} = \frac{V_{xx}}{I_x}\frac{w}{l} \tag{3.6}$$

where w and l are the width and length of the bar (the resistivity is found by multiplying by the thickness, t). In terms of drift velocity (ν_d) the current is given as $I = nqA\nu_d = n_s q\nu_d w$ where n is the carrier density related to the sheet density as $n_s = nt$ and q is the electron/hole charge. When dealing with 2D systems, n_s is often more convenient than n. The force exerted by the magnetic field can be thus expressed by

$$F_B = q\nu_d B_z = \frac{IB_z}{n_s w} \tag{3.7}$$

When considering that the Lorentz force is in equilibrium with the force exerted by

E_y ($F_E = V_H q/w$), V_H can be given in terms of I and B_z

$$V_H = \frac{IB_z}{n_s q} \tag{3.8}$$

or alternately

$$n_s = \frac{IB_z}{V_H q} \tag{3.9}$$

The Hall coefficient (R_H) is a quantity that describes the resulting E_y that balances out the Lorentz force given by

$$R_H = \frac{E_y}{J_x B_z} \tag{3.10}$$

where J_x is the current density along the x-axis. Combining this with equation 3.8, shows the carrier density dependence of R_H

$$R_H = \frac{E_y}{J_x B_z} = \frac{V_H t}{IB_z} = \frac{1}{nq} \tag{3.11}$$

By knowing both V_{xx} and V_H it is possible to extract μ which is defined as $\mu = \sigma/nq$ for low fields ($\mu B << 1$) where the conductivity $\sigma = 1/\rho$. Taking this definition into account using equation 3.6 and 3.9, the Hall mobility can be calculated.

$$\mu = \frac{\sigma}{nq} = \frac{I}{V_{xx}} \frac{l}{wt} \frac{1}{nq} \tag{3.12}$$

$$\mu_H = \frac{V_H}{V_{xx}} \frac{l}{w} \frac{1}{B_z} \tag{3.13}$$

In the case of high magnetic fields or mobilities i.e. $\mu B >> 1$ the resistivity is given as

$$\rho(B) = \frac{\sigma_{xx}}{\sigma_{xx}^2 + \sigma_{xy}^2} \tag{3.14}$$

In practice, heterostructures unintentionally have both electrons and holes contributing to conduction due to background impurities. Hall measurements do not distinguish between the different carriers or layers in the structure, the Hall coeffi-

cient when both types of carriers are present is given as [77]

$$R_H = \frac{p\mu_h^2 - n\mu_e^2}{e(p\mu_h + n\mu_e)} \tag{3.15}$$

which in high fields can be approximated as

$$R_H = \frac{1}{e(p-n)} \tag{3.16}$$

Device Geometries

Hall measurements assume the material is of uniform thickness and that ohmic point contacts are used. Two different types of device geometries are typically used in these types of measurements, bar geometry and Van der Pauw (VdP) geometries.

Hall bar geometries require at least six contacts, two current contacts located at the ends of the bar and a minimum of two pairs of opposing contacts along the length of the bar connected by extended arms, as depicted in figure 3.13. V_{xx} is measured between adjacent contact arms where as V_{xy} is measured from opposing contacts. The standard Hall equations discussed above apply with w as the width of the bar and l as the separation between the measurement contacts. To prevent the shorting of contacts and for accurate measurements, voltage measurement contacts must be placed away from the current contacts and a l/w ratio must be at least 5.

VdP geometries are symmetrical in shape such as squares, crosses and circles, with four point-like contacts located at the edges of the sample. Figure 3.14 demonstrates the resistivity and Hall measurement orientations for a VdP square. The sheet resistivity is given by

$$\rho_{VdP} = \frac{\pi}{ln(2)} \frac{V_{xx}}{I} \tag{3.17}$$

where the voltage V_{xx} is measured by applying a current along adjacent contacts and measuring the voltage across the other two contacts. The Hall voltage, V_{xy} is

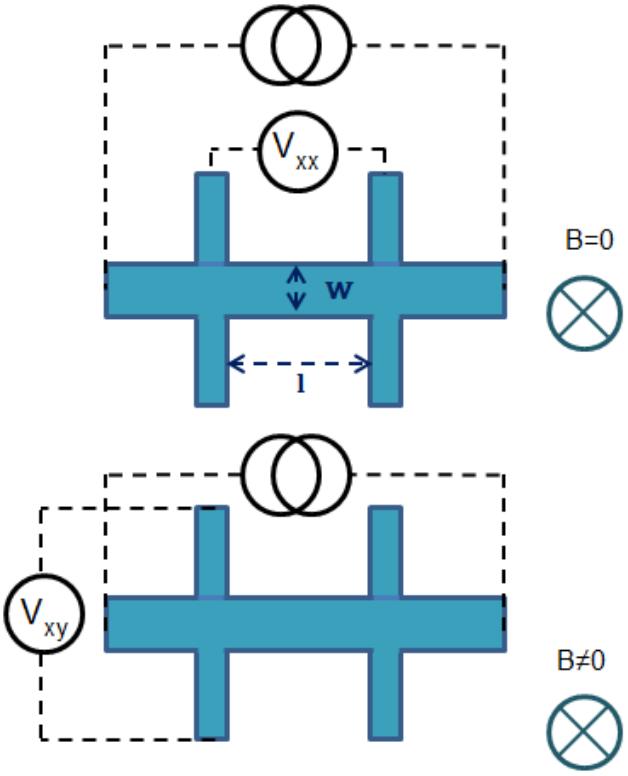

Figure 3.13: A simple six arm Hall bar set-up for magnetoresistivity (top) and Hall (bottom) measurements.

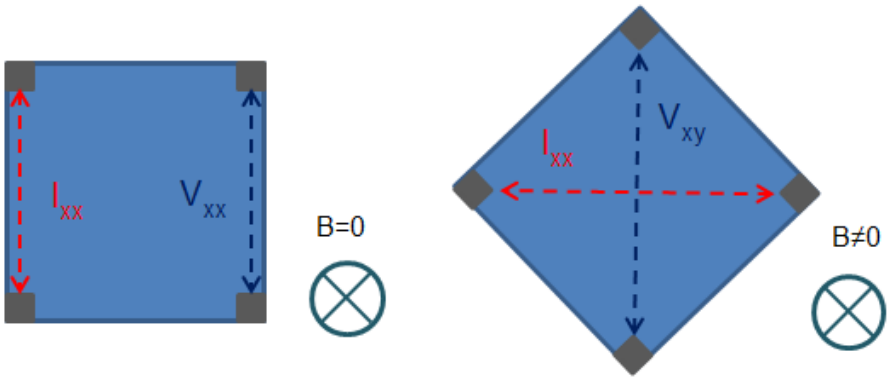

Figure 3.14: A VdP square magnetoresistivity (left) and Hall (right) measurement set-up.

measured by applying I across two opposing corners and measuring the voltage in the remaining contacts. The major source of error in this geometry is the finite size of the contacts.

3.4.3 Sources of Error

Hall bars avoid the issue of finite contact size by using well defined contact arms, the use of optical lithography fabrication techniques also avoid errors associated with misalignment. Voltage measurements can also suffer from additional thermal effects which can contribute the apparent Hall voltage such as the Seebeck effect, Ettingshausen Effect, Nernst effect and Righi-Leduc effect, the origin of these effects are described in references. These additional voltage sources can however be negated by using AC signals and/or reversing the applied magnetic field.

3.4.4 Transmission Line Measurements

Transmission line measurements (TLM) are used to measure the resistance of a contact on a semiconductor. The technique relies on a series of identical contacts spaced at different distances from each other, as depicted in figure 3.15. The resistance of adjacent contacts are measured and plotted as a function of contact separation. The resistance between the metal and semiconductor interfaces (R_{c_i}, R_{c_j}) and the resistance of the semiconductor between contacts ($R_{sc_{ij}}$) act as resistors in series, the total resistance measured between contacts is given by $R_{tot} = R_{c_i} + R_{c_j} + R_{sc_{ij}}$. As the contacts are identical $R_{c_i} = R_{c_j}$ and the resistance of the semiconductor channel is $R_{sc,ij} = \rho_{sc} l_{ij}/w$ the total resistance is given as

$$R_{tot} = 2R_c + \frac{\rho_{sc} l_{ij}}{w} \tag{3.18}$$

where w is the width of the bar. The contact resistance is thus exacted by fitting a straight line and halving the resistance at $l = 0$. Furthermore the gradient is equal

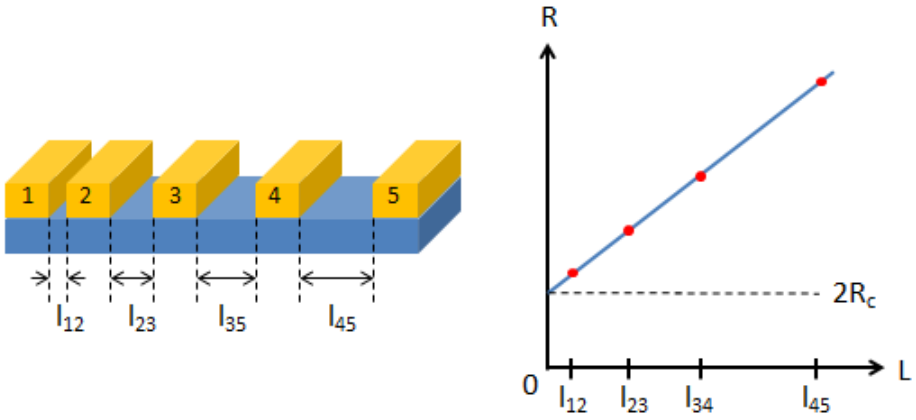

Figure 3.15: An illustration of a TLM device (left) and a typical resistance vs. contact separation plot.

to ρ_{sc}/w.

For standard TLM measurements the contacts are fabricated on a mesa to ensure the current path is only between the contacts. Alternately, circular TLM (CTLM) which use concentric ring contacts can be used without a mesa, the resistances must be normalised by contact area for calculations.

3.5 Electrical Spin Transport Measurements

Spin transport measurements are used to quantify τ_s and L_s. These can be performed using equipment routinely used in magnetotransport measurements.

3.5.1 Hanle Measurements

The Hanle effect initially was used to refer to the phenomenon in which the application of a magnetic field, results in the reduction of emitted polarized light from atoms due to the finite lifetime of atomic states [78][79], more recently the Hanle effect has been applied to accumulation of spin polarised carriers in semiconductors for spin lifetime measurements [28][80]. The application of a magnetic field perpen-

dicular to the spin axis (B_z) induces Larmour precession. Due to the finite spin lifetime, to accumulate spin, spin must be constantly injected. The spin precession causes the spins already in the material to dephase from those just injected from the FM. As the field increases so does the rate at which the spins dephase, until spin accumulation is fully suppressed. The resulting spin accumulation dependence on B_z is a Lorentz curve.

Spin accumulation is measurable as a potential difference. Similar to an accumulation of charge, an accumulation of spin at a point will have a electrochemical potential dependent on the ratio of spin up and spin down carriers $\Delta\mu_{spin} = \mu_{up} - \mu_{down}$. The voltage associated with $\Delta\mu_{spin}$ is given by equation 3.19 where γ is the spin polarisation of the spin injection process.

$$\Delta V_{spin} = \frac{\gamma \Delta \mu_{spin}}{2e} \tag{3.19}$$

The dependence of this voltage on the magnetic field is given by equation 3.20.

$$\Delta V_{Hanle}(B_z) = \frac{\Delta V_{Hanle}(0)}{1 + (\Omega_L \tau_s)^2} \tag{3.20}$$

where $\Delta V_{Hanle}(0)$ is the total spin accumulation single and Ω_L is the Larmour frequency. This equation was originally derrived for optical Hanle experiments [81] and adapted for electrical detection.

In a fully electrical Hanle measurement, spin is accumulated through spin injection/extraction by applying a bias current between a NM contact and a FM-contact. The spin accumulation associated potential difference is measured between a FM-contact and a separate reference NM-contact placed far away from the detector contact such that the carriers below this contact have zero net spin polarisation to maximise ΔV_{spin}. In this type of set-up, there are two possible measurement orientations, local and non-local measurements. The local measurement employs a single FM-contact for both the spin injection/extraction and the detection contact,

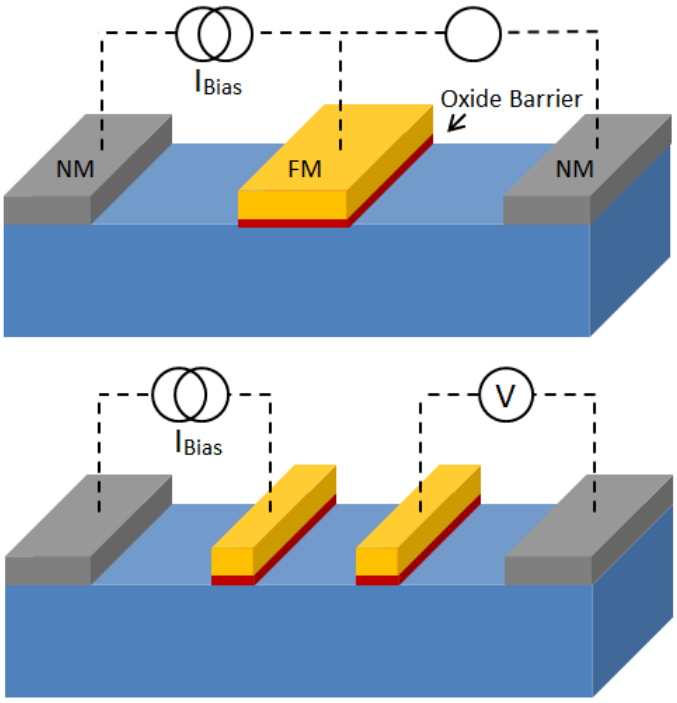

Figure 3.16: An example of a local (top) and non-local (bottom) Hanle set-up. The grey contacts represent ohmic non-magnetic contacts where as the yellow and red stacks are FM tunnel contacts.

as shown in figure 3.16. The local design, also referred to as the three-terminal design was the first fully electrical Hanle studies. This design has since been found to have flaws in terms of measuring an accurate spin signal. Tran et al suggested that the use of a single contact for both injection and detection suffers from an enhancement of the spin signal due to the tunnelling of spins into states either in the barrier or at the barrier/FM interface when using spin tunnel contacts [17]. The occupation of these states by spin polarised carriers thus add to the spin signal being detected in the semiconductor. This phenomenon however, remains a debated subject as there has been no empirical proof of such states enhancing signal.

Non-local Hanle measurements, also known as four-terminal (4T), uses separate FM-contacts for injection and detection as seen in the lower half of figure 3.16. In this case the spins accumulate below one FM-contact and diffuse isotropically

within the material to reach equilibrium. The detector contact is placed away from the injector/extractor contact and measures the potential difference caused by the diffusing spins that are directly below the contact. Due to spin relaxation, as the carriers diffuse away from the site of accumulation, the signal measured in this design is smaller. It is this reason why the separation between the two FM-contacts must be of the order of the SC spin diffusion length for a signal to be measurable.

Chapter 4

Spin-Orbit Interaction in p-Type Quantum Wells

4.1 Introduction

As discussed before, the SOI is a phenomenon central to the operation and mechanisms in spintronic devices and processes such as spin relaxation. In semiconductor spintronics the strength of the SOI dictates the ability of spin modulation as well as the effectiveness to produce a pure spin current via the spin Hall effect. In section 2.2.3, WAL was explained to be a manifestation of a strong SOI in MR measurements and can therefore be used as an indicator of a material's suitability in spintronics where the SOI plays a vital role. The SOI is dependent on the 'Z' value of an element, although Ge does have a larger SOI than Si due to its larger nucleus, this alone is not particularly strong. The use of structural asymmetry in 2DHG and 2DEG heterostructures can enhance the SO strength via the Rashba SOI which can then be tuned externally by a gate, furthermore the low dimensional confinement of carriers have been shown to greatly enhance the mobility of carriers which in turn enhances spin diffusion lengths.

In this chapter I investigate the strength of the SOI in a 2DHG enhanced by

the Rashba interaction through low field MR measurements. In standard electrical measurements, SdH beatings and WAL are both quantum phenomena in which the strength the SOI can be extracted if significant. Although these types of studies are common in III-V materials, Δ_0 has only been published for $Ge/Si_{1-x}Ge_x$ in two systems [48][82] using these methods. Reference [48] was the first published observation of WAL in Ge, which the appearence in itself is an indicator of strong SOI. This chapter will focus on the observation of WAL in a high mobility Ge 2DHG, which was summarised in the published paper [83] (first author) and again analysed briefly in [58] (second author).

4.2 Ge/SiGe Heterostructure and Material Characterisation

Through out this project a number of heterostructures were grown, designed to form a 2DHG in a thin Ge layer, strained to a $Si_{1-x}Ge_x$ alloy buffer with a typical x value of ∼80%. The doping for the quantum wells were chosen to be located adjacent to the Ge epilayer and separated by a spacer (modulated doping). The remote doping was intended to reduce the number of ionised impurities within the conduction channel, which promote momentum scattering and thus reduce mobility. As Ge has a smaller band gap than Si, the non-zero Si content in the $Si_{1-x}Ge_x$ layers causes band discontinuity with the Ge conduction layer and forms a well in the valence band. This is further enhanced by the compressive strain which shifts both the conduction and valence bands in the Ge to higher energies, thus deepening the well. The carriers located in the modulated doping in the upper $Si_{1-x}Ge_x$ layer flow into the lower energy Ge valence band, leaving behind the ionised impurities in the doped layer. The ions generate the electric field across the heterostructure, and thus forms the asymmetry in the Ge channel which in turn induces the Rashba SOI. An example sketch of the band diagram for such a structure is given in figure 4.1.

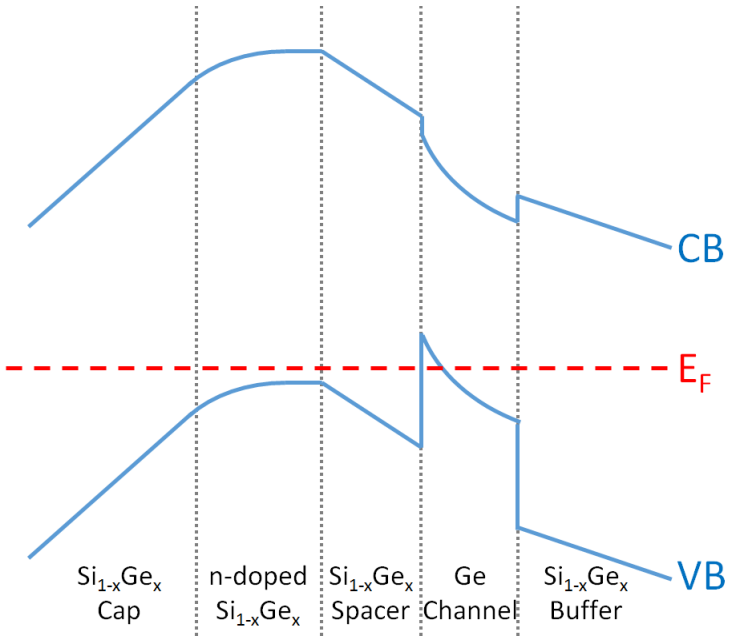

Figure 4.1: An example band diagram for a modulation doped $Ge/Si_{1-x}Ge_x$ p-type QW.

In addition to the electric field, the band discontinuity at the boundary of the well also contributes to the Rashba SOI.

The material of interest is a 22 nm Ge quantum well strained to a $Si_{1-x}Ge_x$ alloy buffer, grown via RP-CVD on a n^--Si substrate (with resistivity 1-20 Ωcm). Growth was first initiated with a low temperature Ge seed layer followed with a thicker high temperature layer with a larger growth rate. The total thickness of this fully relaxed Ge buffer is 500 nm, this is required to ensure a minimal amount of dislocations resulting from the mismatch of lattice parameter between the Si substrate and the Ge. The pure Ge layer forms the base of the linearly reverse graded (LRG) buffer used to gently change the Si to Ge ratio from 100% Ge down to the preferred alloy content to which we want to strain the Ge QW layer. The Ge content is typically decreased by 5% over a thickness of 250 nm. In this sample the Ge content was graded from 100% down to 76%, the growth is continued with the growth of a constant composition layer at 76% for 400 nm. The composition then unintention-

ally switches to 80% Ge, grown at a slower rate to promote higher quality growth with minimal dislocations directly beneath the electrically active section of the heterostructure. Above this, a 22 nm layer of pure Ge was grown, and kept undoped. In this case, carriers from the doping supply layer separated by a spacer, are donated to the quantum confined region, avoiding problems associated with directly doping the conduction channel such as increased momentum scattering which is a source of Elliot-Yafet spin relaxation (described in section 2.3) as well as being detrimental to mobility. The doped layer consisted of a B-doped δ-layer with an additional 20 nm of B-doped (2×10^{18} cm^{-3}) $Si_{0.2}Ge_{0.8}$ layer separated from the Ge QW by a 20 nm $Si_{0.20}Ge_{0.80}$ spacer layer. The heterostructure was capped with a 30 nm $Si_{0.2}Ge_{0.8}$ layer and a 2 nm Si capping layer. The cross-section of this structure is illustrated in figure 4.2.

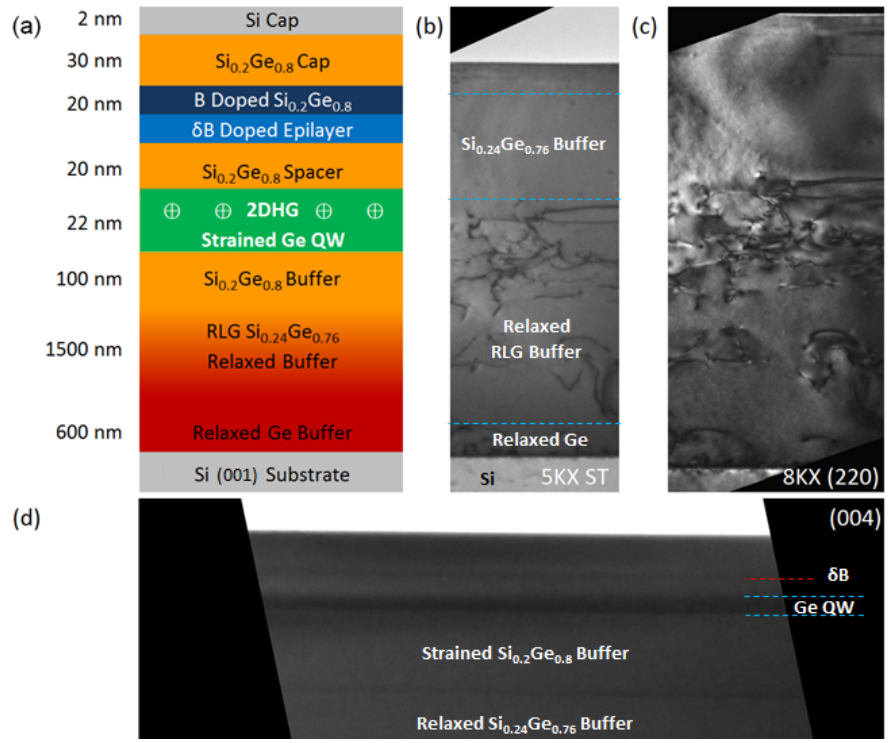

Figure 4.2: (a)A cross-sectional diagram of the sample. (b) The cross-section of the sample as seen at 5kX magnification in the straight through beam condition in TEM. (c) The full sample as seen in the (220) DF condition emphasizing the dislocations in the buffer regions. (d) The QW region in the (004) condition.

The thicknesses of these layers were confirmed by both cross-sectional TEM and SIMS given in figures 4.2 and 4.3. The Ge at the interface with the Si substrate can be seen to have a large amount of dislocations, caused by the lattice mismatch between Ge and Si and release of strain upon relaxation, the remainder of the fully relaxed Ge buffer remains largely defect-free for high quality growth. The LRG buffer is easily picked out from the image due to the large amounts of dislocations for similar reasons, the layers above this buffer are much higher quality with little or no visible dislocations, this is required to achieve high mobilities. High magnification TEM micrographs reveal that the upper interface of the QW is not as well defined and shows evidence of a diffusion of Si from the upper alloy layers, which may be detrimental to the mobility of carriers in the channel. Other features to note in these micrographs are the darker lines above and below the QW. These mark stages in the growth procedure where Ge had segregated to the surface during a pause in growth, this is also evident in the SIMS data (figure 4.3) where there are unexpected spikes of Ge. The upper line occurs at the interface between the spacer layer and doped layer, whilst the lower line separates high and low temperature growth stages.

The Ge composition of the $Si_{1-x}Ge_x$ alloy was determined through both XRD and SIMS. The (004) symmetric scan given in figure 4.4 along with the asymmetric (224) scan, confirms the presence of the Si substrate, Ge buffer, as well as strong $Si_{0.05}Ge_{0.95}$, $Si_{0.2}Ge_{0.8}$, $Si_{0.24}Ge_{0.76}$ peaks and a number of fringe peaks from a strained layer. The smearing of signal between the Ge and $Si_{0.2}Ge_{0.8}$ peak represents the smooth change in Ge content in the relaxed LRG buffer, whilst the $Si_{0.05}Ge_{0.95}$ peak was confirmed to be present at the beginning of the fully relaxed LRG buffer by SIMS. The (224) asymmetric scan provides the additional information on the strain of the different layers, extracting the in-plane lattice parameter revealed that the Ge buffer was 105% relaxed with respect to the Si due to the thermal contraction of the lattice post growth. The peaks representing the $Si_{0.05}Ge_{0.95}$ and the

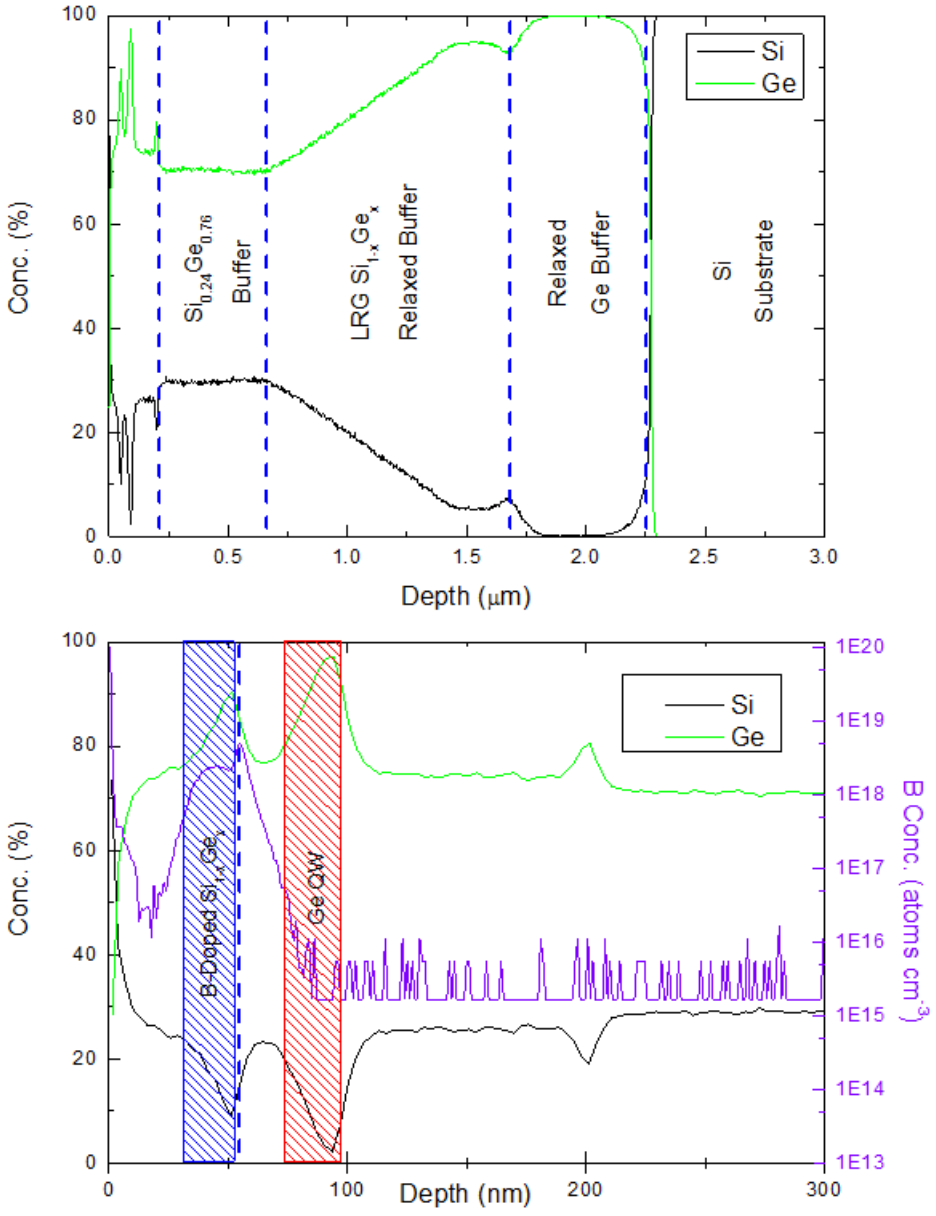

Figure 4.3: Top: SIMS depth profile for Si and Ge concentrations throughout the heterostructure. Bottom: Si Ge concentrations in the top 300 nm of the structure with B concentration (violet) on the right axis.

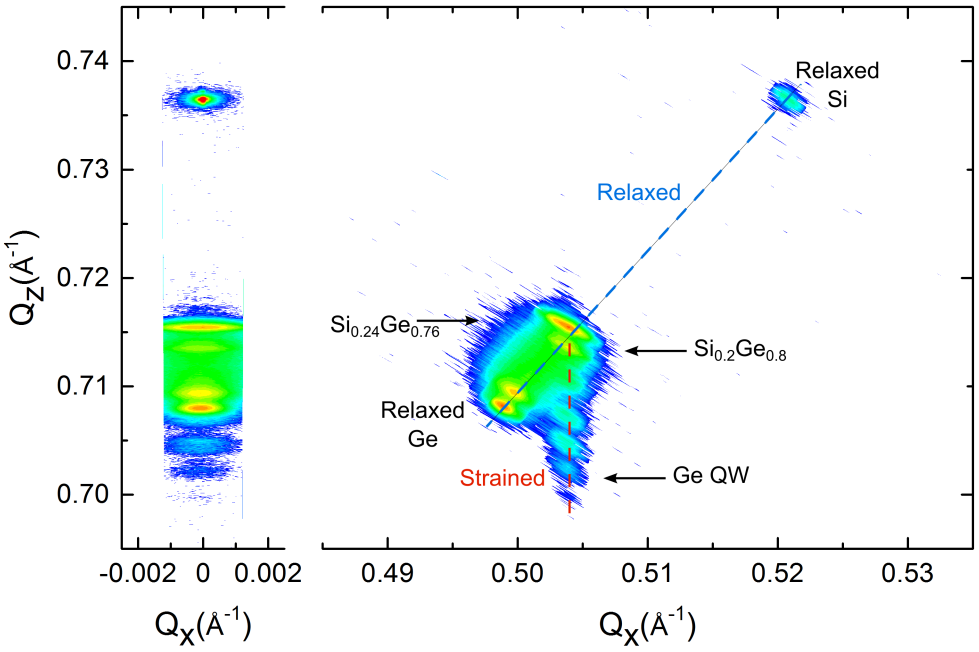

Figure 4.4: Symmetrical (004) and asymmetrical (224) RSM scans of the sample.

$Si_{0.24}Ge_{0.76}$, as well as the smearing of counts representing the LRG buffer all lie on the line of relaxation between the Si and Ge peaks, indicating full relaxation in these layers, with the $Si_{0.24}Ge_{0.76}$ layer being at 108% relaxation with respect to the substrate. The $Si_{0.2}Ge_{0.8}$ peak however is located directly beneath the $Si_{0.24}Ge_{0.76}$ indicating that the $Si_{0.2}Ge_{0.8}$ layers above the LRG buffer remain fully strained to the $Si_{0.24}Ge_{0.76}$. Due to the low thickness of the Ge QW layer, we expect the QW to also be fully strained to the $Si_{0.2}Ge_{0.8}$ layer below and in turn fully strained to the $Si_{0.24}Ge_{0.76}$. In this case the peak should appear below the $Si_{0.24}Ge_{0.76}$. Unfortunately this is obscured by the presence of interference fringes. As there are no additional $Si_{0.2}Ge_{0.8}$ peaks seen, it can be assumed that the top most $Si_{0.2}Ge_{0.8}$ layers are also fully strained, the fringes can thus be from either one of the strained $Si_{0.2}Ge_{0.8}$, the strained Ge QW or additionally a combination of fringes from the three different layers. The peak representing the QW (marked in figure 4.4) was determined by calculating the supposed composition of each peak to find one that

represented a Ge composition of 100%. The identified Ge QW peak was found to be under ∼1% lattice mismatch strain.

As noted in the above sections, SIMS profiling was used in parallel with XRD and TEM for the confirmation of layer thickness and $Si_{1-x}Ge_x$ composition. The thickness obtained using SIMS data agreed well with the those obtained in TEM measurements. The compositions obtained using SIMS however was consistently 4-5% lower in Ge compared to XRD measurements, the errors associated with SIMS accounts for this discrepancy. As well as alloy composition, a SIMS profile of the first 400 nm was taken to produce an accurate B-doping profile given in figure 4.3. The doping supply layer is recorded to have a B-concentration of $\sim 2.4\times10^{18}\,cm^{-3}$ with a peak concentration of $\sim 5\times10^{18}\,cm^{-3}$ in the δ-doped region, it is important to not that the initial high level of B concentration is an artefact of the scan. The B-doped modulation layer is shaded in blue on the SIMS profile. For the most part, the doping seems fairly uniform across this region with some degree of segregation (9 nm/dec) reducing the B-concentration at the uppermost interface. The spike of B to the right of this peak, marked by the blue dashed line is the δ-doping. It is clear that the QW, represented by the red shaded region in figure 4.3 remains largely undoped. Other profiles of contaminants such as O, Cl, C, H, F and N were also scanned for but remained below the detection level.

A number of 50μm×50μm and 20μm×20μm AFM surface scans taken across various areas of the sample give an RSM roughness of (2.5 ± 0.5) nm. In industry, a typical roughness of 1 nm is commonly realised, however the roughness observed here is typical for high mobility structures which employ virtual substrates for strain engineering. Cross-hatching on the surface is clearly visible in the scans and is associated with the formation of dislocations in strain relaxation processes [84] [85].

The band structure for the top 250 nm of the heterostructure, generated from a self-consistent 1D Poisson-Schrödinger simulation is given in figure 4.6. Due to the Si content in the $Si_{0.2}Ge_{0.8}$ buffer and spacer layers, the band gap in these regions

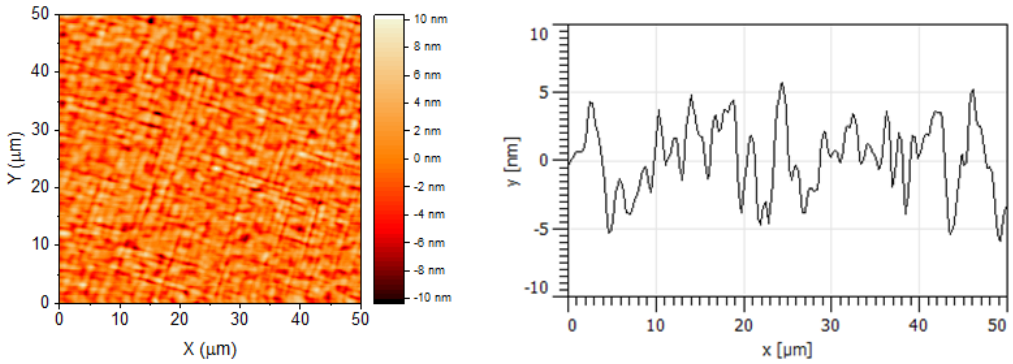

Figure 4.5: A 50µm×50µm AFM scan (left) of the sample displaying the crosshatch pattern and a line profile (right) taken through the centre (left to right) of the scan.

are larger than that of Ge, furthermore the compressive strain of the 22 nm Ge conduction layer shifts the Ge valence band up, allowing the formation of a QW in the valence bands. The modulation doping layer provides a potential which creates an electric field across the QW to produce the asymmetry giving rise to the Rashba interaction.

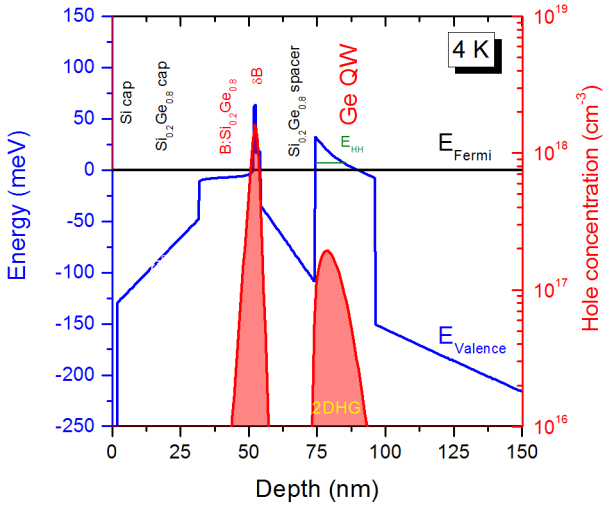

Figure 4.6: Valence energy band diagram (blue) and hole carrier concentration (red) as given by self-consistent Poisson-Schrödinger simulation at 4 K. E_{HH} corresponds to the filled HH3 energy levels in the Ge QW, at this temperature, the LH energy levels remain unoccupied.

4.3 Magnetotransport Measurements

4.3.1 Fabrication

Resistivity and Hall measurements for the sample were performed using an 8-contact Hall bar type device as seen in figure 4.7, with a bar width of 50 µm and a separation of 250 µm between contact arms. The Hall bars were fabricated using optical lithography techniques discussed in section 3.3.1.

The first stage of fabrication focused on defining and depositing the contact pads using a negative mask and AZ512E negative resist. The resist was spun at 4000 rpm and baked at 115 °C for 60 s, before a 2 s mask exposure corresponding to 33 mJcm^{-2} exposure energy. The AZ512E resist can act as both a positive or negative resist. After the initial exposure, the pattern defined in the resist layer is positive, the pattern is reversed by baking the sample at 120 °C for 120 s. A final flood exposure of the full sample is then carried out for 10 s (165 mJcm^{-2}) to allow undercut side walls for improved lift-off after deposition. The pattern is developed for 60 s in MF-319 developer. Before deposition, the exposed surface is cleaned to avoid contamination or impurities at the metal semiconductor interface. Initially the surface undergoes a 30 s Ar plasma ash and is then dipped in 2% HF solution to remove any native oxides, this also produces a H-terminated surface which in the short term prevents surface oxidation during the transfer to the deposition stage.

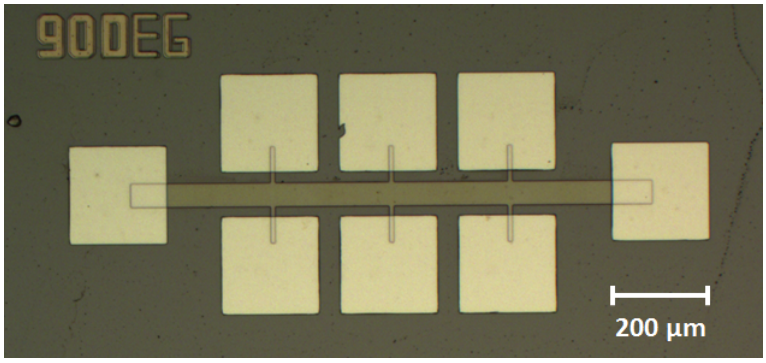

Figure 4.7: The Hall bar type device fabricated and used in experiments.

The contact material used is Al, of which 300 nm was thermally evaporated onto the material and lifted off using acetone.

Lithography of the bar mesa uses a positive process with S1818 resist. This is spun at 4000 rpm and baked at 120 °C for 180 s. A positive pattern is exposed for 10 s (165 mJcm^{-2}) and developed in MF-319 for 60 s. A 95% SF_6 with 5% O_2 dry etch allows the formation of the mesa with sloped side walls due to the additional O_2. The remaining resist is removed using an acetone bath.

The depth of the QW in the structure makes it difficult for deposited contact material to form ohmic contacts. For this reason, the sample is annealed at 375 °C for 25 minutes in an N_2 atmosphere to allow the diffusion of Al into the sample such that direct contact is made with the conduction channel. In electrical measurements, the contacts remained ohmic for all temperatures.

4.3.2 Transport Measurements and Parameters

Typical MR measurements, using standard lockin techniques used to extract Hall mobilities, carrier densities, sheet resistivities and Hall coefficients were carried out using a ^{4}He CCC in a temperature range of 10-300 K with a 1.2 T (perpendicular field) electromagnet at both positive and negative fields. This used a single lockin set to 119.33 Hz in series with a 10 MΩ resistor to source and 100 nA current. A switching box also allowed the measurement of voltage across different contacts of the Hall bar to obtain v_{xx} and v_{xy} with the single lockin. A Heliox AC-V ^{3}He CCC with a 12 T superconducting electromagnet was also used over a range of 0.3-300 K. The increased temperature range allowed observation of quantum phenomena such as WL/WAL and SdH oscillations, furthermore, the 12 T superconducting magnet also allowed more in-depth measurements of SdH oscillations, whilst also providing higher resolution for low fields where WL and WAL dominates the resistivity. The electrical set up consisted of four lockin amplifiers set to 119.33 Hz to ensure minimum noise. One lockin in series with a 10 MΩ resistor provided a sourcing current

of 100 nA as well as the reference frequencies for the remaining three lockins, whilst also measuring the potential across the current contacts. Two lockins simultaneously recorded v_{xx} across two pairs of adjacent contacts, with the last measuring v_{xy} across two opposing contacts. In these measurements, the perpendicular magnetic field is swept to ± 12 T.

The obtained magnetotransport parameters are given in figure 4.8. The temperature dependence of the sheet resistivity gave clear evidence of 2D behaviour, with ρ_{xx} decreasing with temperature. This is related to the strong dependence of mobility on carrier concentration. As the temperature decreases carriers begin to freeze out, leading to a reduction of carrier-carrier scattering as well as phonon scattering. The most significant scattering mechanism contributing to electrical resistance however is ionized impurity scattering, the majority of which should be located in the modulation doped layer. Ideally the carriers from background impurities located through out the structure, as well as the carriers located in the doping supply layer will freeze out at sufficiently low temperatures, leaving carriers confined solely to the relatively dislocation-free and impurity-limited Ge conduction layer. The extracted sheet carrier Hall density (p) closely follows this type of behaviour starting at $\sim 3\times10^{12}$ cm^{-2} at 300 K gradually dropping with temperature as carriers begin to freeze out, down to 1.93×10^{11} cm^{-2} at $\sim$45 K. Below 45 K, further freeze out stops, stabilising the carrier concentration. This effect is mirrored in the temperature dependence of mobility given in figure 4.8 (right axis), starting at 1035 cm^{2}V^{-1}s^{-1} at 300 K rising to a maximum of 777,000 cm^{2}V^{-1}s^{-1} below $\sim$45 K.

Subnikov de Haas Oscillations and Effective Mass

SdH oscillations in ρ_{xx} can be used to extract m^*. These oscillations are described by equations 2.12a, 2.14 for high and low fields respectively. A glance at the SdH behaviour in figure 4.9 shows no obvious beating attributed to spin splitting and some complex behaviour of the oscillations at fields >0.5 T. For now we will concentrate

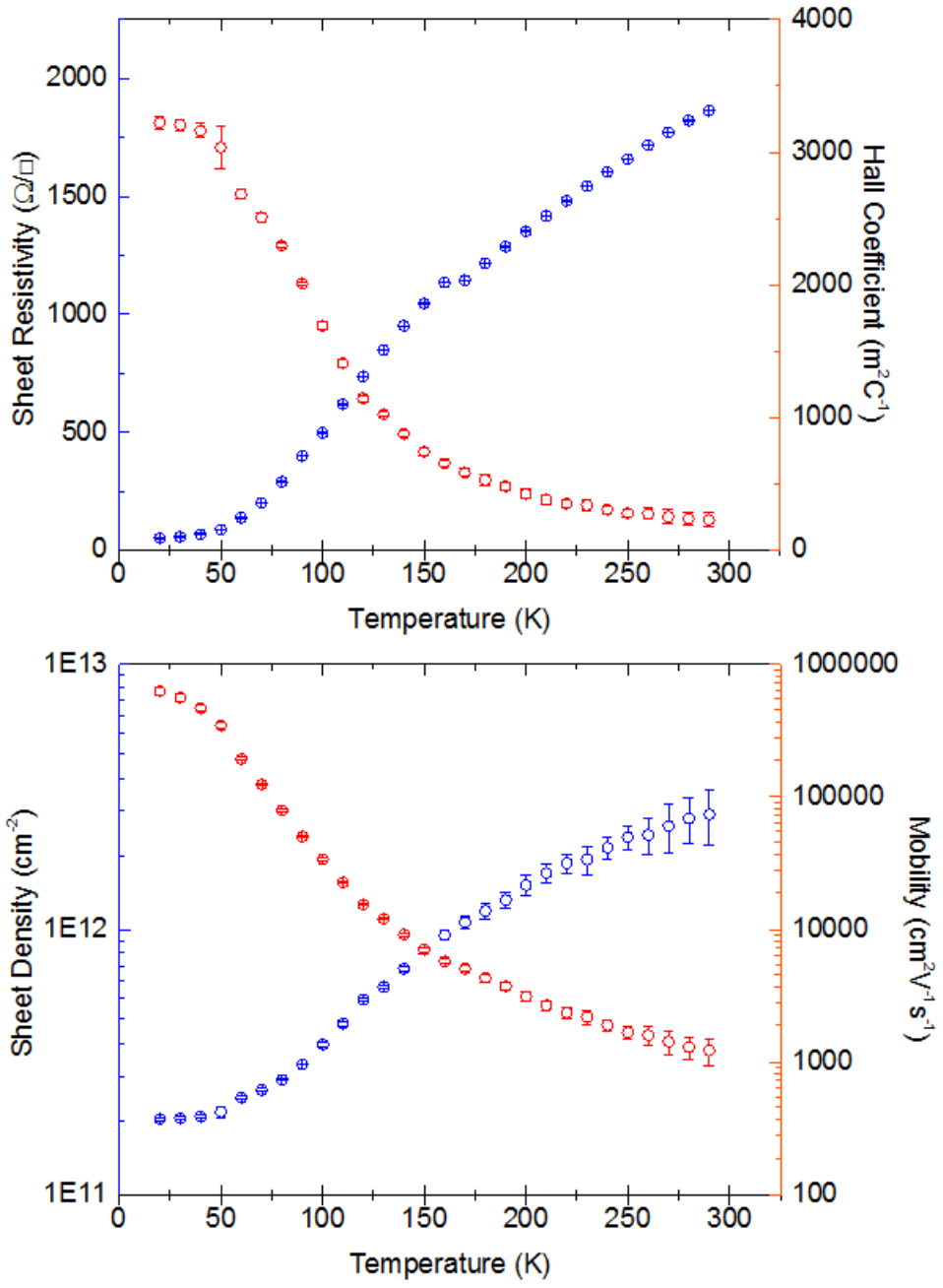

Figure 4.8: Top: Temperature dependence of sheet resistivity (blue) and Hall coefficient (red) for the sample. Bottom: Temperature dependence of Hall sheet carrier density (blue) and Hall mobility (red).

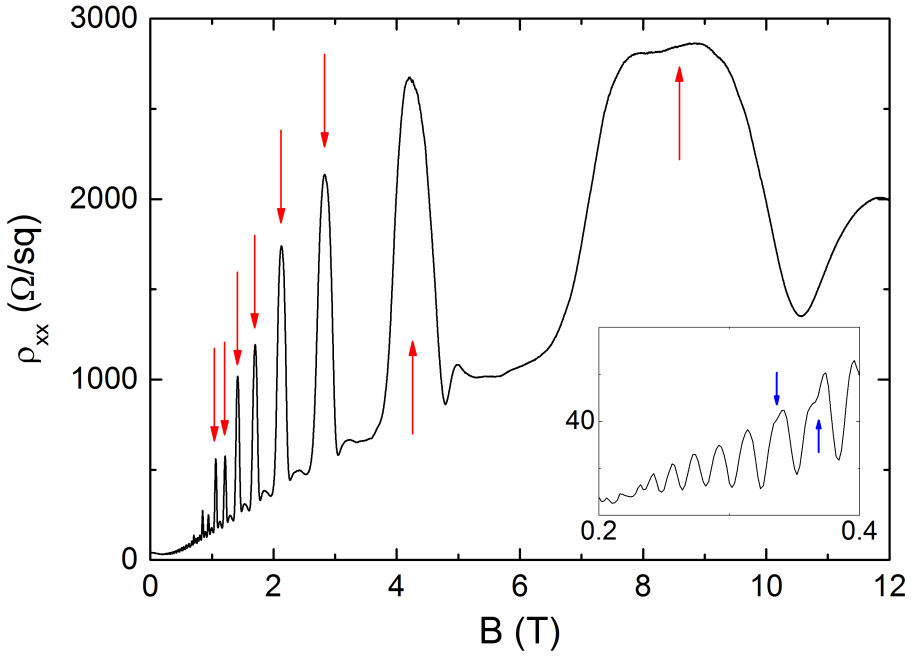

Figure 4.9: A plot of sheet MR displaying SdH oscillations at high fields and low fields (inset) for 0.388 K. Anomalous SdH peaks that suggest a contribution from the presence of a parallel conduction layer are indicated by red arrows and the blue arrows in the inset mark the first observable effects of Zeeman splitting.

on the oscillations at low fields where behaviour is closer to normal. The absence of beating allows us to use equation 2.12a, here the parameters left unknown to us are m^* and α_D, the Dingle ratio. Both of these can be deduced in an iterative process which will not be discussed here. These values were calculated by C. Morrison in references [58][82] and were found to be $m^* = (0.065 \pm 0.05)m_0$ and $\alpha_D = 18 \pm 2$.

4.3.3 Parallel Conduction

When examining the MR of the sample, two abnormalities are noticeable, firstly there is a slight asymmetry is visible in the MR curve with respect to the direction of the perpendicular field, secondly is the anomalous behaviour of the SdH oscillations at higher fields. The source of asymmetry in these measurements are

often attributed to parallel conduction in the heterostructure, and the anomalous behaviour in the SdH oscillations is a result of multiple frequencies in the oscillations. Using equation 2.12a, it can be seen that the frequency is dependent on m^*, indicating the presence of multiple carriers with different mobilities. In these particular structures there are two possibilities for this to occur [86], first is the presence of active carriers in a separate layer and second is the occupation of more than one sub-band. For a p-type QW the latter means the occupation of both the HH and LH-bands. Due to the compressive strain of the Ge channel the HH and LH-bands are non-degenerate thus for intermediate levels of carrier concentrations, the LH-band should remain unoccupied. At low temperatures, the self consistent 1D Poisson Schrödinger simulation revealed that the sheet carrier concentration required a level that exceeded $10^{12}\,\mathrm{cm}^{-2}$ for the LH band to be occupied, the sheet carrier concentration extracted from Hall measurements fall safely below this level and thus dismisses the latter possibility.

The second possibility is commonly seen at higher temperatures where background impurities in the buffer/bulk layers are active, leading to multiple carrier types (both electrons and holes), with different mobilities in different layers. At low temperatures, the most likely source is from the over-doping of a supply layer [86] in which the concentration is too high for all dopants within the layer to freeze out. As seen in figure 4.3, the segregation of Ge at the δ-layer resulted in a higher Ge content than the adjacent layers, effectively producing a relatively shallow $Si_{1-x}Ge_x$ QW. The high doping level of the δ-layer allow for the population of the unintended $Si_{1-x}Ge_x$ QW, providing an additional conduction path at lower temperatures. The concentration of carriers were also simulated for the top 150 nm of the structure and is given in figure 4.6, which also shows the presence of carriers in the doped region. Detailed analysis of the parallel conduction and MR in this sample is discussed in reference [57].

It is important to note that the parameters extracted via Hall measurements

are the averaged over all of conductions channels present in the sample. Due to the nature of the parallel conduction, it is expected that this doped channel will have fairly poor transport properties, bringing down the overall measured values. Indeed, this was analysed in detail by M. Myronov in reference [36] for this sample at room temperature in which the Ge channel's mobility was calculated to be $4230\,\mathrm{cm^2V^{-1}s^{-1}}$, the highest mobility measured for a Ge 2DHG at room temperature. It follows from this that the underestimation of μ_H occurs at low temperatures due to the continued presence of parallel conduction from adjacent layers.

4.4 Evidence of Weak Anti-localisation in Low Field Magneto-Resistivity

The low-field, low temperature MR plots are given in figure 4.10. The MR at the lowest temperatures ($0.44\,\mathrm{K} \leq T < 1.9\,\mathrm{K}$) formed a peak about the zero field synonymous to the WL conductivity quantum correction, that becomes completely suppressed at $\sim$1.8 T. However at 1.9 K a small dip, 4 mT either side of the zero field appears in the central peak, this overall shape of a large peak with the addition of a central minima is a common form of WL/WAL like behaviour in which WAL dominates at the lowest fields before ceding to WL at intermediate fields. As the temperature increases, the dip in MR appears to become wider whilst maintaining relatively the same depth, between $1.9\,\mathrm{K} \leq T \leq 7.1\,\mathrm{K}$. This apparent transition into WAL from WL as temperature is increased is non-consistent with current WAL theory or past experiments. As WAL effects are dominant when $L_{SO} < L_\phi$, it is expected that WAL should be present at the lowest temperatures. As temperature increases, L_ϕ decreases due to the increase of inelastic scattering, thus it is expected that WAL should weaken with increasing temperature, giving way to a purely WL negative MR correction at higher temperatures, where $L_\phi < L_{SO}$. Past 7.1 K, the WAL-like feature becomes shallower, with the larger WL-like peak also decreasing

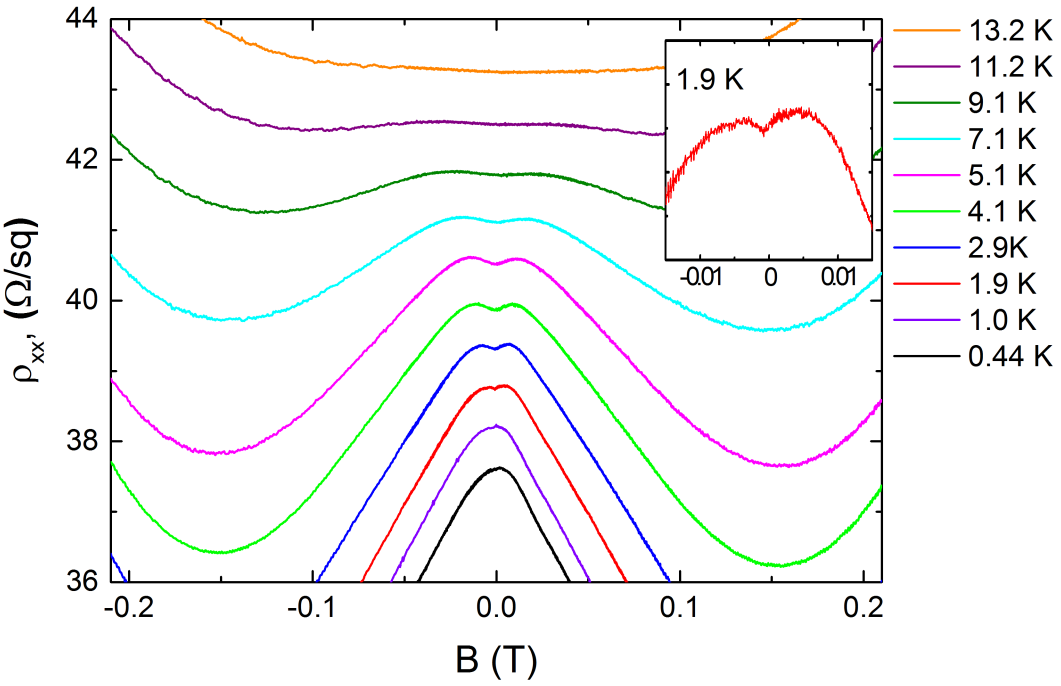

Figure 4.10: Low-field magnetoresistivity in the temperature range of 0.44 K-13.2 K, with curves offset for clarity. The positive magnetoresistivity at the smallest fields indicates a presence of WAL, the inset shows the positive MR at 1.9 K at the lowest fields.

in amplitude, until all WL/WAL corrections to the MR disappear above 11.2 K, reflecting the condition where $L_{tr} > L_{\phi}$.

Discussion on the Abnormal WAL-WL Transition at Intermediate Temperatures

The apparent transition from WAL to WL at intermediate temperatures may be explained with the presence of the parallel conduction layer. If we assume the modulation doped layer does indeed contribute to the conduction at these temperatures, MR measurements would not be able to distinguish the two conduction layers from each other and the measured resistivity will be a summation of the conductivities of both layers. It can also be expected that the parallel conduction layer may also

have a quantum correction to the conductance at low fields.

As stated in section 2.2.3 the behaviour of WL/WAL is dependent on the parameters τ_{tr}, τ_{ϕ} and τ_{SO}, it is clear that these parameters are vastly different with respect to the two conduction channels. On top of the much smaller τ_{tr} (due to μ being small), we expect the spin splitting in this layer to be negligible when compared to that of the Ge QW. The source of the SOI in the Ge QW stems from the electric field generated from the potential of the charge impurities in the doping supply layer. Being located within the supply layer and at the peak density of charge centres, the SOI in the unintended $Si_{1-x}Ge_x$ QW does not benefit from an internal electric field in addition to having a lower Ge content. This layer thus should not exhibit WAL as τ_{SO} will be too large to satisfy the condition $L_{SO} < L_{\phi}$. At the lowest of temperatures the WL MR peak will be at its strongest and sharpest, this could effectively mask the central WAL dip from the Ge QW contribution to the MR.

Along with the different characteristic times of the two layers, one also expects a different temperature dependence to the WL/WAL effects. The gradual appearance of a WAL-like dip suggests a cross-over from the quantum correction being dominated by the conductivity in the supply layer to that of one being dictated by the transport in the Ge QW. For this to happen, the quantum effects in the supply layer must have a stronger temperature dependence. The transport in the supply layer however can be assumed to be diffusive. Although one expects the carrier-phonon scattering to be effective in the supply layer due to the relatively high density charge impurities, the dominating phase breaking mechanism for 2D materials at low temperatures is believed to be the quasi-elastic Nyquist e-e scattering with phonon-carrier scattering becoming significant at high temperatures above 30 K [59]. This type of scattering mechanism may be stronger in the supply layer owing this to its smaller width and higher carrier density.

The clean limit is defined as $k_B T \tau_{tr} > \hbar$ and is satisfied for all temperatures

measured, when using $\tau_{tr} = 29\,\text{ps}$ (which is constant below $\sim$40 K), the transport in the Ge QW is therefore ballistic. The same cannot be said for the QW in the supply layer, which is thought to have a significantly lower τ_{tr}. The Nyquist e-e scattering rate $1/\tau_{ee}$, in 2D systems has been shown to be stronger in the ballistic regime with a temperature dependency of $T^2 \ln T$ whilst $1/\tau_{ee} \propto T \ln T$ in the dirty limit [59], although this is contradictory to what we are suggesting in the previous paragraph, it does not take into account the vastly different environment of the carriers.

Estimation of the Spin-Orbit Splitting

Next we attempt to extract the SO-splitting and Rashba parameter. Experimentally, the spin splitting is extracted by fitting WL/WAL models to the low field magnetoconductivity (MC) using the fitting parameters B_ϕ, B_{SO1}, B_{SO3} or alternately $\tau_\phi, \tau_{SO1}, \tau_{SO3}$. Depending on the transport properties, separate models for diffusive [62][63] and ballistic [64] systems exist. Past studies in high mobility materials found fits to the MC using a diffusive model quickly deviated from experimental data at B_{tr} [87][88], the upper field limit for diffusive transport. B_{tr} is calculated with equation 2.22 using the diffusion coefficient $D = \nu_F^2 \tau_{tr}/2$ for which the Fermi velocity $\nu_F = k_F \hbar/m^*$ and $k_F = \sqrt{2\pi p}$. For this sample B_{tr} $\sim$0.01 mT, much smaller than half the width of a typical WAL feature, highlighting the importance of the model developed by Golub. Figure 4.11 shows the quantum conductance correction ($\Delta\sigma = 1/\rho_{xx}(B) - 1/\rho_{xx}(0)$) as a function of B/B_{tr} at 2.9 K where the WAL feature survives at fields orders of magnitudes larger than B_{tr}. Indeed we expect B_{tr} for the Ge QW to be smaller as τ_{tr} is underestimated for the Ge QW channel due to the indiscriminate nature (in terms of multiple conduction channels) of Hall measurements. Sub mT values of B_{tr} have been reported in other high mobility structures [47][87][89] on the order of $\sim 0.5\,\text{mT}$, the fact that the value we see here is smaller is a testament to the high mobility/quality of the material.

The use of a single model to fit the behaviour of this sample is difficult.

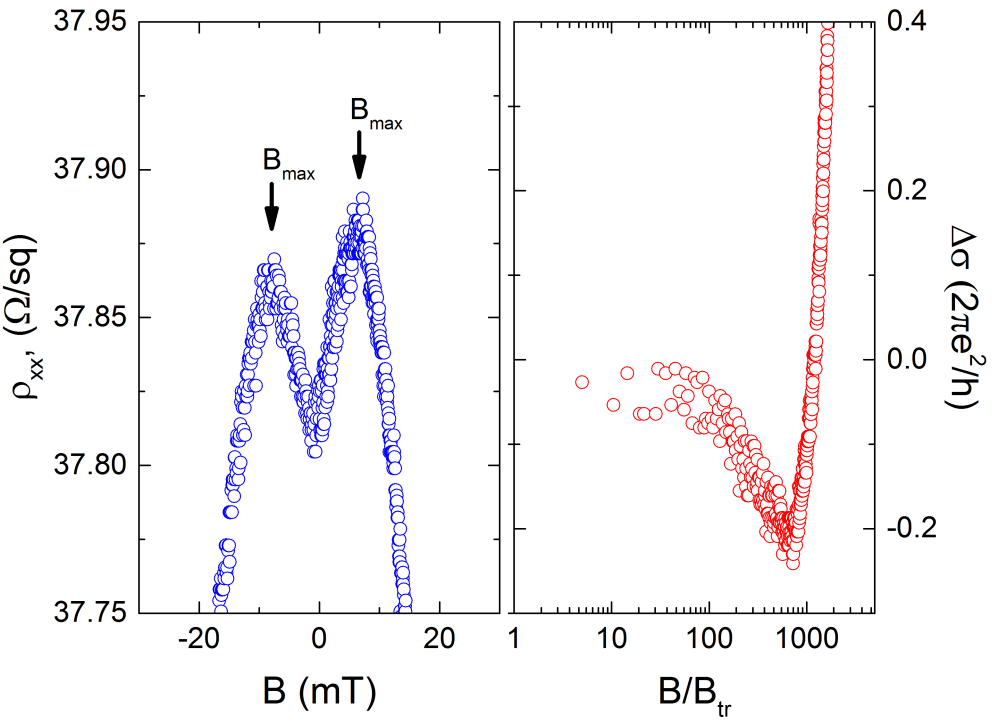

Figure 4.11: The low field MR at 2.9 K (left) and the quantum conductance correction, $\Delta\sigma = 1/\rho_{xx}(B) - 1/\rho_{xx}(0)$ as a function of B/B_{tr}(right). B_{tr} is much smaller than the width of the WAL feature as well as the magnet's minimum field.

Firstly, we have the problem of the contribution of two channels to the WL/WAL correction, doubling the fitting parameters. Secondly, the parameter τ_{tr} which is known prior to fitting is unknown here for the separate channels. Instead we choose to estimate B_{SO} by looking at the value to be the field at which WAL crosses over to WL in the MR curve (i.e. the position of the maximum B_{max} in the low field MR) as this field is clearly related to the strength of the SOI [90]. A number of studies have found the estimation $B_{so} \approx B_{max}$ to be effective [88][89][90]. As indicated in figure 4.11, B_{max} and by extension B_{SO} is ~0.7 mT. Equations 2.9 and 2.21c are utilized to extract Δ_0 =0.84 meV. As stated earlier, the compressive strain lifts the four fold degeneracy of the HH-LH bands, along with the low hole density, these provide the conditions required for the single band occupancy of the HH-band states.

It follows that the Rashba interaction in the Ge QW will be $\boldsymbol{k}$-cubic and thus the spin splitting will take the form in equation 2.8, corresponding to a cubic Rashba parameter of β_R =3.2×10^{-28} eVm^3. At this point we remind the reader that these calculated values characterising the Rashba spin splitting are only approximations particularly as the values τ_{tr} and p used in the calculations are taken from the whole heterostructure at low temperatures and not just the Ge QW.

Comparison the Rashba SOI With Similar Structures

Values of Δ_0 has been published only for two other strained Ge QW systems, one from WAL fittings [48] and the other from SdH beatings [58][82] and will be referred to as 'sample A' and 'sample B' respectively. Δ_0 and transport parameters are given in table 4.4 for these samples. All three structures are under compressive strain and claim to have cubic Rashba, allowing for a close comparison between the systems.

It is encouraging that the Δ_0 obtained here is of the same order as the two Ge systems, whilst also boasting a significantly higher mobility (approximately ×2 for sample A and $\sim$ ×150 for sample B). Δ_0 for this heterostructure also sits between the values given for samples A and B. There is a negative trend in mismatch strain and Δ_0 for the three structures, this points to the competition between the LH-HH splitting and the SO splitting, a larger strain mismatch results in a larger separation between LH and HH bands, suppressing Δ_0 [49][53]. The sample studied here also has a significantly lower hole density (<1.9×10^{-11}cm^{-2}) than the other two structures ($\sim$6×10^{-11}cm^{-2}). A lower hole density will also reduce Δ_0 as $\Delta_0 \propto k_F^3$ for cubic Rashba and $k_F \propto \sqrt{p}$, despite this Δ_0 is relatively strong. If β_R is compared, the sample studied here is actually the strongest of the three, possibly due to a large internal electric field from the high levels of doping. It is difficult to attribute this to either the relative dependency of k_F or HH-LH splitting on Δ_0 as one must also take into account of the doping density/profile which generates the field within the heterostructure. For a detailed analysis of the Rashba SOI in these systems it is

Material	**$Ge/Si_{0.24}Ge_{0.76}$ 2DHG [83]**	$Ge/Si_{0.2}Ge_{0.8}$ 2DHG [82]	$Ge/Si_{0.5}Ge_{0.5}$ 2DHG [48]	$In_{0.2}Ga_{0.2}As/GaAs$ 2DHG [91]	$GaAs/Al_{0.31}Ga_{0.69}As$ 2DHG [92]
Mismatch Strain (%)	**1.1**	0.8	2.1	-	-
Low T Mobility ($cm^2V^{-1}s^{-1}$)	**777,000**	450,000	5,000	80,000	160,000
Carrier Concentration ($\times 10^{11} cm^{-2}$)	**<1.93**	5.9	6	5	3
Δ_0 (meV)	**0.8**	1.4	0.3	2.5	0.7
β_R ($\times 10^{-28} eVm^3$)	**3.2**	1.0	0.3	2.2*	2.5

Table 4.1: A summary table of SO-strengths and transport parameters in various 2DHG systems. * denotes values calculated using the parameters given in the publication.

recommended that a single front and back-gated heterostructure is used to investigate the effect of the internal electric field without altering carrier density or HH-LH separations [93][94].

Other values of Δ_0 for other 2DHG materials [91][92] have been provided as well in table 4.4. Once again our value of Δ_0 is of the order of the other materials, with only reference [91] boasting a value three times ours, but with a smaller β_R. Like sample A, we believe this to be an enhancement due to the hole density. Furthermore, these two structures will also have a cubic contribution to the SOI from the BIA induced Dresselhaus SOI. Our value of β_R supports our claim for Ge to be a suitable platform for spin modulation in semiconductor spintronics as we still observe an appreciable Rashba SOI in our material comparable to other popular candidates, whilst not having the inclusion of an untuneable Dresselhaus SOI.

Lack of Spin Splitting Induced SdH Oscillation Beatings

It is interesting that the SOI in the sample studied is able to produce WAL and not have any visible beatings in the SdH oscillations, indeed high mobility materials that exhibit WAL effects also produce spin-split beatings in SdH oscillations [47][88][95]. The reason behind this is explored in reference [58] where SdH oscillations are simulated using the measured transport parameters and the Δ_0 for sample B (due to their similarities). It was noted that the point at which beatings become sizeable enough to observe is dependent on τ_q, pointing to a small value. However when compared with sample A, τ_q is significantly larger ($> \times 3$) suggesting a beating should be visible at lower fields ($<1.7\,\mathrm{T}$) in the sample studied here. It was also suggested that the effect of Zeeman splitting could complicate and obscure the beating pattern. It is observable in figure 4.9, that the Zeeman splitting becomes notable at $\sim 0.3\,\mathrm{T}$. In light of the estimation $B_{SO} \approx B_{max}$, I repeat the simulation here with our calculated Δ_0 using equation 2.14 for more accurate analysis.

Substituting E_F, m^*, α_D and Δ_0, we get the plot in figure 4.12. The simu-

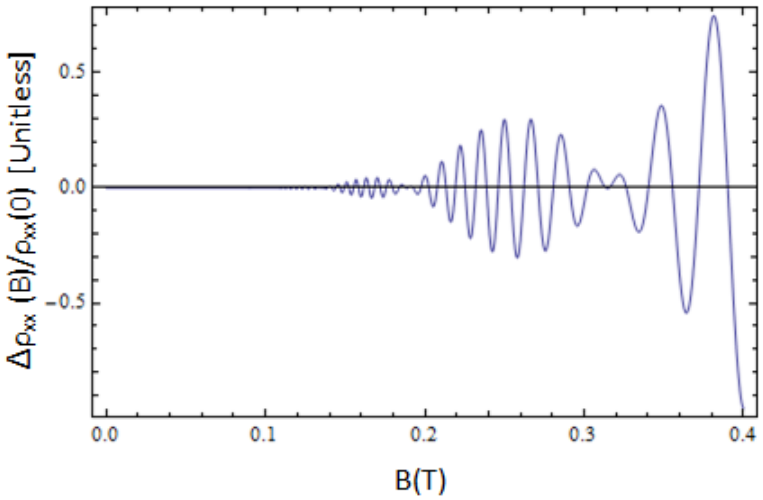

Figure 4.12: A simulation of the normalised SdH correction in our sample using equation 2.14 and calculated parameters.

lated plot of SdH oscillations is normalised to $\rho_{xx}(0)$ and ignores Zeeman splitting as well as other quantum contributions. From the plot we see that the initial beatings are very insignificant at a resistivity <4% of $\rho_{xx}(0)$. The beatings only begin to become noticeable at fields 0.3 T for which the Zeeman splitting is also noticeable and free to interfere with the beating behaviour.

4.5 Summary

Here we present the observation of WAL in a modulated doped strained Ge 2DHG, for which was measured prior to the first observation reported in publications. The presence of WAL is a manifestation of a strong SOI in the material for which in group IV materials only originate from the Rashba interaction, in this case asymmetrical modulation doping. Here the Rashba SOI is expected to be cubic in $\boldsymbol{k}$, as the 1.1% mismatch strain lifts the degeneracy of the HH-LH bands, leaving only the HH-band occupied at lower hole densities. The transport properties of the sample studies already boasts very high mobilities for low temperatures (μ_{LT} >777,000 $\mathrm{cm^2V^{-1}s^{-1}}$). as well as having the largest recorded mobility at room temperature for Ge. This

already makes Ge a great candidate for general high performance electronics particularly as these mobilities also compete well with p-type III-V and II-VI rival materials.

First impressions of the low field, low temperature MR revealed the presence of WL at lowest temperatures, before transitioning to WAL at >1.9 K, which then began to become suppressed at higher temperatures. This non-standard behaviour was attributed to the effect of a parallel conduction layer found in the modulated doping supply layer, due to over doping. We believed the effect to be a superposition of WL-behaviour in the low mobility supply layer QW and WAL in the Ge QW, with different temperature dependencies.

The complexity of the low field MR meant the data was not suitable for fitting to WL/WAL models in which the strength of the SOI can be extracted from. Instead we make the estimation $B_{SO} \approx B_{max}$ and from this calculated Δ_0 =0.8 meV and β_R=3.2×10^{-28} eVm^3. Not only does our value of Δ_0 agree well with others seen in similar structures, but our cubic Rashba coefficient β_R, is amongst the highest recorded for both group IV and III-V 2DHGs.

Our observation of a strong Rashba SOI in a high quality, high mobility Ge 2DHG promotes Ge as a candidate platform for the proposed spin-FET and other spin modulation devices such as the Aharonov-Casher ring [96], for which a strong Rashba SOI is required, preferably in the absence of the Dresselahaus SOI.

Chapter 5

Optimisation of Tunnel Barrier Fabrication on Ge

Non-equilibrium spin currents are achievable in non-FM materials with a number of methods namely spin pumping [8], optical injection [12], electrical injection [9] and the SHE [97]. Of the four, the latter two are the only practical techniques that can be implemented in a device suitable for application purposes, furthermore electrical spin injection is also key to the operation of the Datta Das spin-FET [32].

The conductivity mismatch problem stands to be a major problem for achieving sizeable spin polarised currents in semiconductors and for this reason spin tunnel contacts are favoured. Spin tunnel contacts are sensitive to the quality of the barrier and it has been demonstrated that crystalline barriers produce superior spin polarisation due to their interface quality [98][99]. Rough interfaces can result in reduced spin polarisation [28] of the tunnelling current, whilst defects in the barrier itself can provide traps for spins to tunnel into where they can relax before tunnelling into the bulk semiconductor [17][100]. In research this has prompted a move towards the growth of highly crystalline barriers, typically MgO grown by MBE [30][100][101]. Although this is useful for day-to-day research, MBE cannot be used to produce larger scale devices in industry, instead industry favours electron beam evaporation

as well as magnetron sputtering followed by annealing treatments for fabrication in MTJ technology.

In this chapter I concentrate on the development of tunnel contacts on Ge deposited by common deposition techniques as well as annealing for improving barrier and interface quality. Oxide barriers, when deposited by evaporation or sputtering in standard vacuum conditions, results in an oxygen deficiency and poorer barrier characteristics, this is usually rectified with the use of O_2 plasma [102] or post annealing to reduce trap density [103]. Due to the limitations of fabrication equipment at Warwick, the following oxide films studied have not undergone an O_2 plasma treatment.

5.1 XPS Study of Annealed Ferromagnet/Oxide Films on Ge

At high temperatures the barrier layer can be destroyed either by the movement of bulk material upwards (segregation), or the metal contact downwards (diffusion). Some metallic impurities in Si and Ge can diffuse particularly fast in high temperatures such as Ni and Fe, which are both common materials used in spintronics. In pure Ge at temperatures >800 °C, Fe has a diffusion coefficient $>10^{-11}\,m^2s^{-1}$ and Ni, $>10^{-9}\,m^2s^{-1}$, compared to Ge self diffusion at $>10^{-17}\,m^2s^{-1}$ [104].

Closer attention must also be paid in heterostructures, particularly for 2D channels where high temperatures can cause significant changes due to the diffusion of dopants and the diffusion of pure elemental layers to areas of lower composition [43]. In the case of $Ge/Si_{1-x}Ge_x$, such as the ones discussed in the previous chapter, this leads to a broadening of interfaces and a reduction of Ge content which will have detrimental effects of the transport in the 2D layer. Past studies within the Warwick Nano-Silicon group have found the diffusion of pure Ge layers in $Ge/Si_{1-x}Ge_x$ heterostructures at temperatures >550 °C. The temperatures at which these processes

occur limit the annealing treatments available to the oxide layers during fabrication.

The study of the diffusion of Ni and NiFe in Ge at low temperatures (<500 °C) has been extremely limited, particularly in the context of insulating oxide barriers and their limitations to annealing treatments. Here I look at the diffusion behaviour these two metals on Ge with and without oxide barriers and the limitations of these barriers to annealing temperature.

XPS Study of Step Annealed NiFe/Ge

In this section, an XPS study of annealed NiFe/metal-oxide films on Ge is analysed. XPS measurements in this study were performed by Dr. M. Walker at Warwick using an Omicron XPS system with an Al K_α source (15 kV anode voltage) with a resolution of 0.4 eV. The measured spectra were analysed by myself using the software CasaXPS.

Initial measurements look at the behaviour of NiFe films on epitaxially grown i-Ge (∼1.3 µm), on Si substrates. The films were prepared by sputtering; prior to deposition the Ge surface was cleaned with 2% HF solution to provide a H-terminated surface and prevent native oxides from forming. A sputtering rate of 0.5 $Å s^{-1}$ was used to deposit a (7.5 ± 0.5) nm layer of NiFe on two samples simultaneously (as confirmed by TEM). The schematics of these structures are given in figure 5.1 (left).

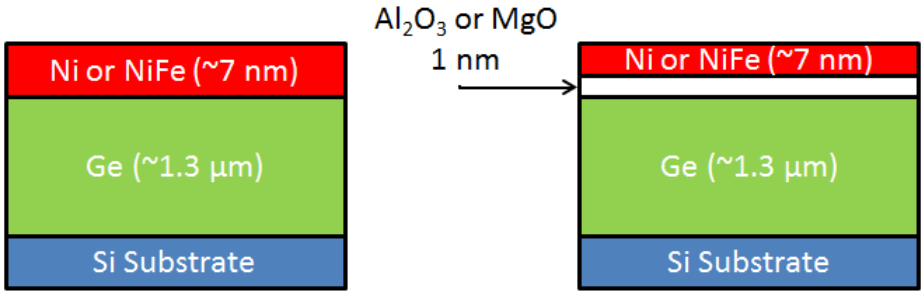

Figure 5.1: A schematic of the type of structures used in the XPS annealing studies for FM/Ge and FM/Oxide/Ge stacks.

The samples were step annealed in-situ at UHV for 1 hour at 150 °C, 200 °C, 250 °C, 300 °C and 400 °C. Depth resolution was achieved by using 30° and 90° take-off angles (TOA).

Analysis of the XPS spectra obtained from the pre-annealed sample, revealed visible Ge 3d peaks with minimal/no noticeable oxide peaks for the 90° TOA scan and no visible Ge peaks at the same energy for 30° TOA scan, allowing a sensitive study of the Ge surface. The evolution of the Ge 3d peaks are given in figure 5.2.

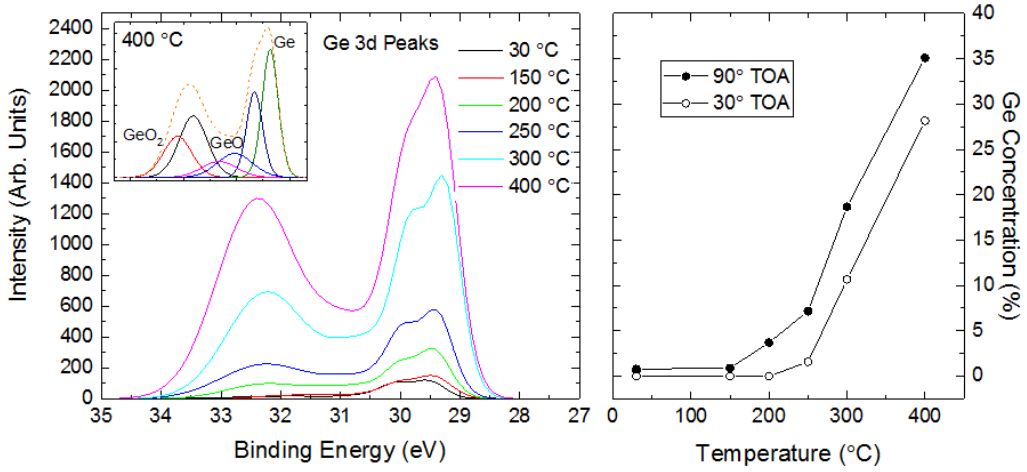

Figure 5.2: The fitted XPS spectra (TOA 90°) curves for the Ge 3d peaks for annealed NiFe on Ge (left) and the calculated Ge concentration as a function of annealing temperature (right). The inset shows the various Ge and GeOx (spin-split) peaks used in the fitting at 400 °C.

The Ge 3d peaks consisted of three pairs of spin-split peaks (with a splitting of 0.59 eV), corresponding to the Ge-elemental (29.3 eV), GeO (30.3 eV) and GeO_2 (34.4 eV) peaks. It can be seen that in the 90° scan, the associated Ge peak intensities begin to increase at temperatures >150 °C. The calculated content starts to increase gradually for 150 °C<T≤200 °C, whilst the surface sensitive 30° scan only begins to register a change in the Ge concentration above 200 °C. The calculated Ge concentration (elemental and oxide combined) against Ni and Fe was calculated, where the concentration is seen to experience a sharp increase above 200 °C.

For Ni and Fe, we focus on the Ni and Fe 3p peaks, as the stronger 2p peaks

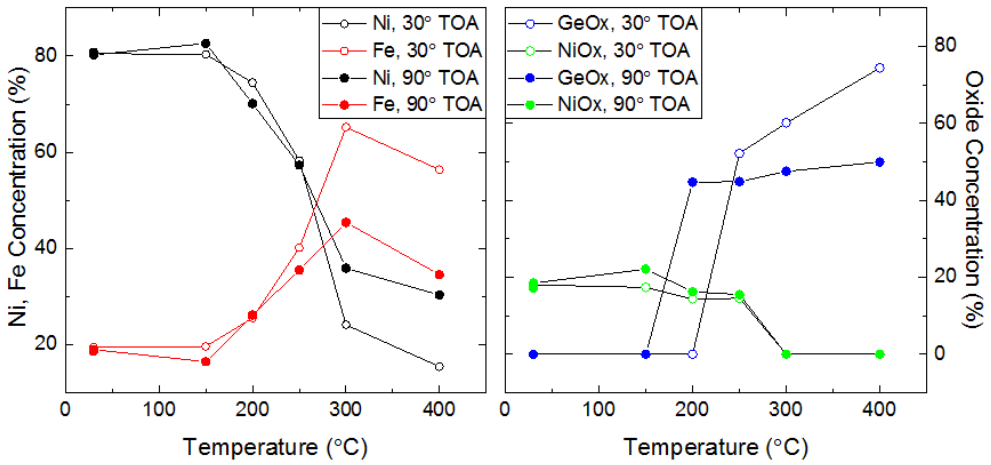

Figure 5.3: Ni and Fe concentrations as a function of annealing temperature (left) and the percentage of oxidised Ni and Ge, compared to their pure elemental composition.

are complicated by an overlapping Ni LMM Auger peak. The ratio of Ni to Fe as a function of annealing temperature is given in figure 5.3.

The ratio of Ni to Fe initially stays at 8:2, this is representative of the standard ratio for permalloy. Above 150 °C, the concentration of detected Ni drops whilst, both Fe and Ge increase corresponding to a diffusion of Ni into the bulk. Fe appears to segregate to the surface as the surface sensitive 30° scan rises quicker than the 90° scan. The small drop at high temperatures may correspond to the continuous movement upwards of Ge. It is interesting to note that the percentage of oxide to pure element (also given in figure 5.3) for Ge when diffusion occurs, is fairly large (>40%) despite cleaning the Ge surface prior to deposition and the UHV of the XPS chamber. The reduction of Ni oxides, leads us to believe that the Ge is absorbing the O atoms from the diffusing Ni.

The separation of Ni and Fe in the annealed sample may prove to be problematic, as the segregation of Fe may lead to a Ni-rich FM/Ox layer and therefore a reduced spin polarisation.

Real Time Annealing XPS Study on Metal/Ge and Metal/Oxide Thin Films on Ge

The study continues with real time annealing (RTA) scans of four different thin films; sputtered NiFe/Ge, and electron beam evaporated Ni/Ge, Ni/Al_2O_3/Ge and Ni/MgO/Ge with oxide thicknesses of 1 nm (as illustrated in the right of figure 5.1). As stated before, these samples were cleaned with 2% HF solution prior to deposition for which oxides were deposited at a rate of 0.2 $Å s^{-1}$ and 0.5 $Å s^{-1}$ for metals. In this study, the temperature of the sample was quickly ramped up to 200 °C at which point spectra was collected before ramping to 350 °C (in the space of 15 minutes) for RTA scans. The range of the spectra collected was 25 eV-80 eV, encompassing the Ge 3d, Ni 3p, Fe 3p, Al 2p and Mg 2p peak energies, this was completed every 134 s for 5.5 hours. This will gives more information on the process of diffusion during annealing, as well as the time required for diffusion to occur. In addition to this, a step anneal measurement was completed for the NiFe/Ge stack as described in the previous study.

Figure 5.4 shows the different peaks used for the fitting the NiFe/Ge RTA. The Ge 3d peaks used the same components (Ge, GeO, GeO_2) as in the stepped annealed samples. The Ni 3p peaks consisted of a spin-split Ni elemental component (66 eV) and a NiO component pair (69 eV). The Fe peaks however, were more difficult to analyse, appearing as mostly an Fe oxide peak at ∼56 eV (possibly $NiFe_2O_4$ or Fe_2O_3) with a minor contribution of the elemental peak as well as being located on a wide plasmon loss peak.

The concentration of the elements/compounds as a function of annealing time, plotted in figure 5.5 and as expected shows a rapid increase of Ge to the surface of the stack and a decrease in Ni and Fe concentrations. Initially the concentration of Ge is very low, despite being significantly above 200 °C, this is attributed to the NiFe layer being thicker than those in the previous measurements as the Ge peak was not visible with a 90° TOA prior to annealing. In addition, this sample was

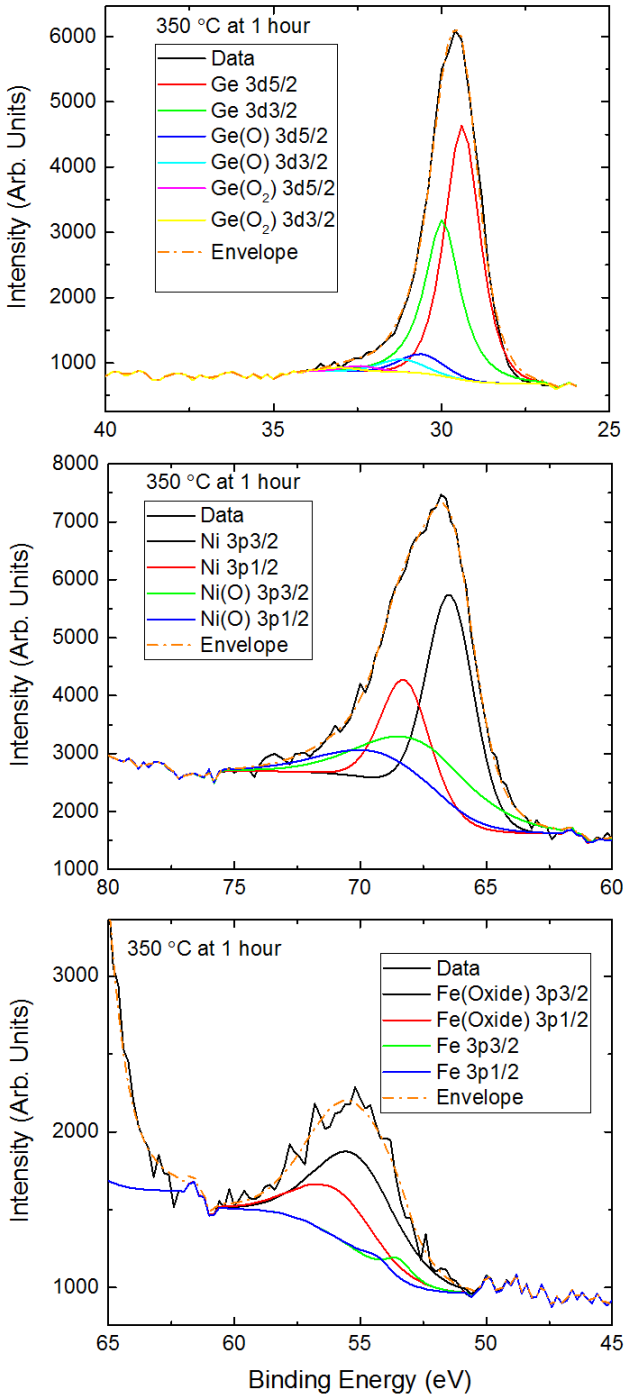

Figure 5.4: A plot of the measured XPS spectra annealed after an hour at 350 °C, including the fitted components for Ge 3d (top), Ni 3p (centre) and Fe 3p (bottom) peaks.

also rapidly annealed to 350 °C as opposed to being step annealed for an hour at different intervals, leaving less time for diffusion. The diffusion of Fe into the bulk at this temperature suggests a transition to a different regime for the behaviour of Fe occurs at T>300 °C, explaining the drop in Fe we see in figure 5.3. The disappearance of Fe from the scan region appears to be constant up until 100 minutes at which point there only remains trace amounts of Fe and the rate at which Ge segregates slows down, as it in now only dependant on the diffusion of Ni.

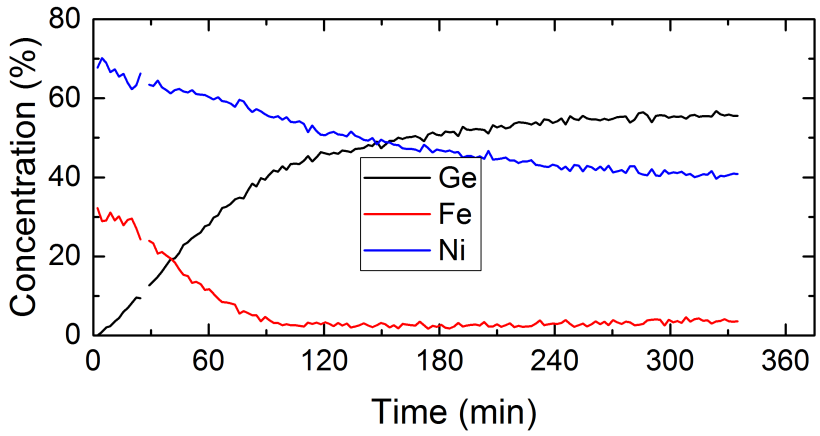

Figure 5.5: A plot of Ge, Ni and Fe concentrations against annealing time for the NiFe/Ge stack at 350 °C.

The behaviour of pure Ni on Ge was found to be more radical, with the Ni-NiOx:Ge-GeOx ratio changing from 95:5 as deposited to 55:45 at 200 °C, before the RTA. This is unsurprising as Ni is routinely annealed on Ge at temperatures less than 300 °C to form Ni-Germanide for low Schottky barrier/ohmic contacts [105]. A comparison of the collected spectra, given in figure 5.6 along with the compositions calculated for the RTA measurement. Over the course of the RTA scan the Ge-GeOx concentration rises from 56% to 63%. It is clear from these that the Ni component of NiFe alloys are the most destructive factor to the surface of Ge during annealing.

The additional oxide layers act as a physical barrier to prevent diffusion of

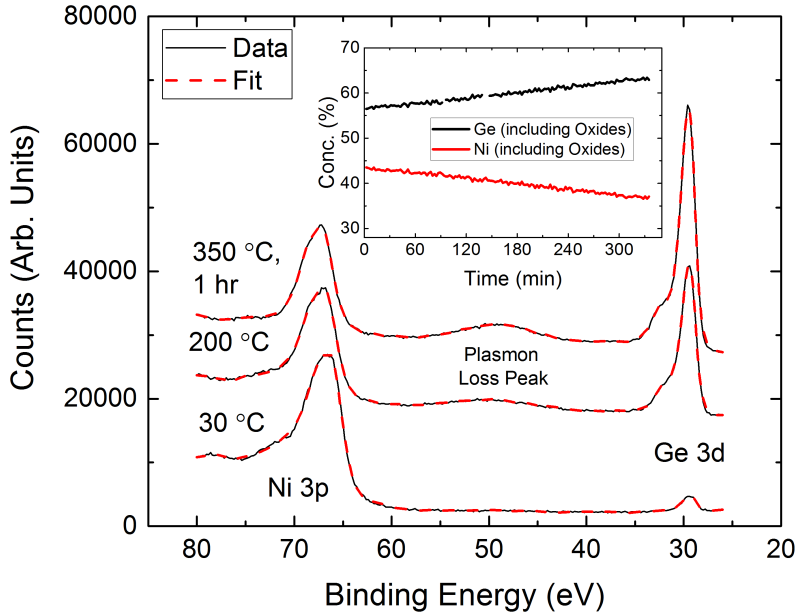

Figure 5.6: The Ni/Ge XPS spectra at 30 °C, 200 °C and 350 °C, 1 hour into annealing (offset for clarity). Inset: A plot of Ge and Ni (combined element and oxide) concentrations against annealing time for the Ni/Ge stack at 350 °C.

metal into the bulk, this concept was effective to different degrees when annealing the two samples with metal-oxide barriers. The same fitting parameters were used for the Ni and Ge peaks, with the additional peaks for Mg 2p and Al 2p.

The spectra obtained for the MgO and Al_2O_3 barrier samples at the three temperatures and a plot of element concentration against time for the RTA are given in figures 5.7 and 5.8 respectively. Both oxide structures underwent no change between the room temperature and 200 °C stages, with no visible change in Ge or Al/Mg, already improving upon the Ni/Ge and NiFe/Ge samples. A small MgO peak and prominent Ge peaks were however visible at 350 °C. The MgO concentration remained at a constant level through out the anneal whilst Ge content only increased by 2%. From this we can establish that the barrier had broken down rapidly whilst ramping up to 350 °C.

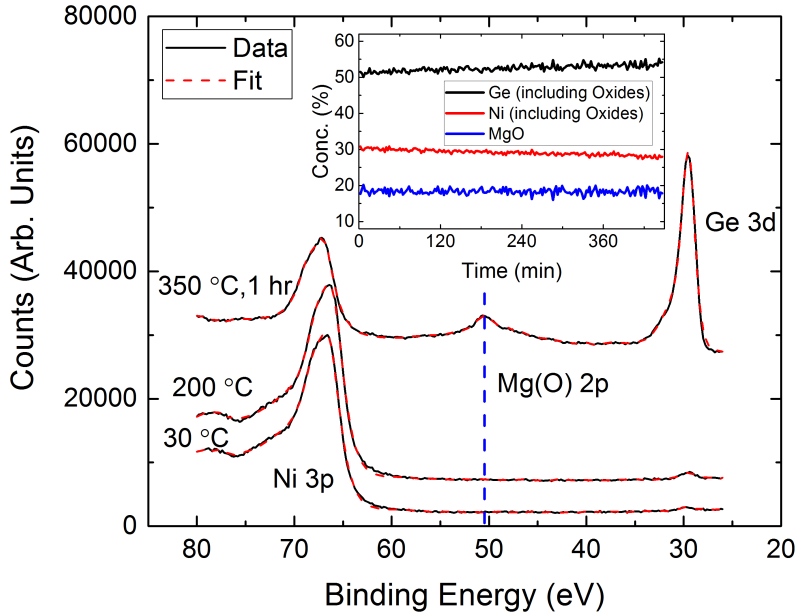

Figure 5.7: The Ni/MgO/Ge XPS spectra at 30 °C, 200 °C and 350 °C, 1 hour into annealing (offset for clarity). Inset: A plot of Ge, Ni (combined element and oxide) and MgO concentrations against annealing time for the Ni/MgO/Ge stack at 350 °C.

The Al metal and oxide 2p 3/2 peaks are typically located at binding energies ~72.4 eV and ~74.1 eV respectively, which overlap with the positioning of the Ni 3p oxide peaks visible for all samples measured. In the initial stages of the RTA, only the Ni peaks are visible, it is only after 45 minutes when a Ge peak begins to appear and a small hump representing the $Al(_2O_3)$ 3p peaks becomes visible in the vicinity of the Ni(O) 2p spin-split peaks. From this point onwards there is a steady rise in both Ge and Al content until 240 minutes into the anneal at which the concentration curves stabilise.

What is also of note for the Ni/Al_2O_3 annealed sample is the absence of an extended shoulder at the higher energy of the Ge 3d peak representing Ge oxides also seen in the other samples, even after the scan finishes. For temperatures $\leq$200 °C in the other samples, the feature begins to rise. This feature is part of an Ni oxide

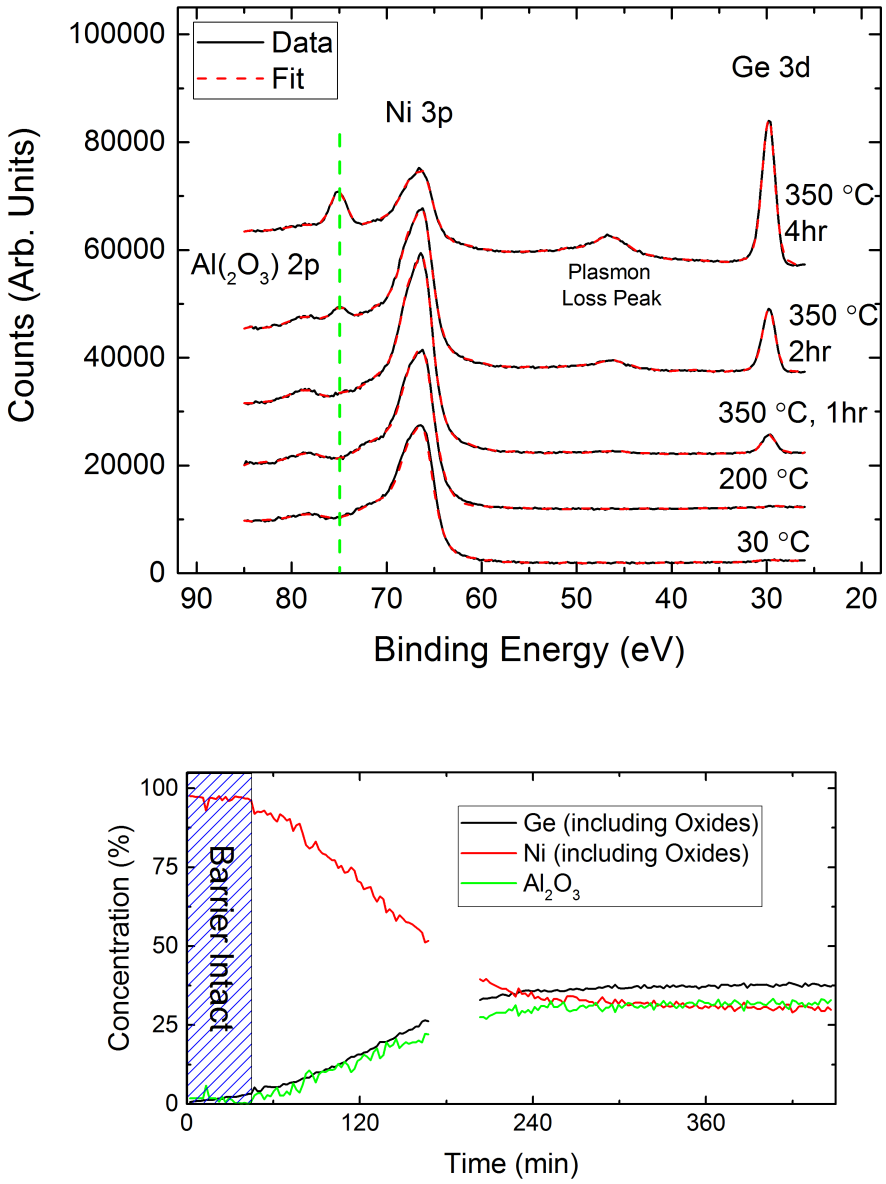

Figure 5.8: Top: The $Ni/Al_2O_3/Ge$ XPS spectra at 30 °C, 200 °C and 350 °C 1 hour into annealing (offset for clarity). Bottom: A plot of Ge, Ni (combined element and oxide) and Al_2O_3 concentrations against annealing time for the $Ni/Al_2O_3/Ge$ stack at 350 °C. Gaps in the concentration are due to corrupt scan files.

(likely Ni_2O_3), seen in the Ni/Al_2O_3 sample due to its extended scan range of 5 eV to accommodate the observation of the Al 3p peak. The exclusion of this peak in the previous scans is acceptable as it has a relatively low intensity and vanishes before the RTA. This peak however is still visible in the Ni/Al_2O_3 annealed sample and only begins to shrink after 3 hours of annealing. The absence of Ge oxides suggests that the oxide is instead absorbed by the (limited) presence of the oxygen deficient Al in the barrier layer, as opposed to being absorbed by the segregating Ge. We do not see this happen in the other scans due to a significant amount of segregation before the RTA.

The failure of the 1 nm MgO barrier below 350 °C is troubling, however the Al_2O_3 barrier can survive at this temperature for ∼45 minutes allowing it to be integrated with minimal changes into our current fabrication processes which use a 25-45 minute 375 °C anneal to diffuse Al into the bulk or heterostructure.

It is clear from the concentration plots analysed here, that increases of bulk and barrier material at these temperatures only occur when the metal layers are diffusing into the bulk and not due to thermal induced processes in the bulk or barrier itself. Indeed a step annealing study performed on a thin film (10 nm) of Al_2O_3 on Ge for 30 minute anneals at 200 °C up to 600 °C in 50 °C intervals, showed no change in concentration ratios between the different atomic concentrations. The spectra taken at all stages contained weakly visible Ge 3d peaks ensuring that changes to the material content should be detectable.

The use of NiFe is more common in spintronic studies and devices, particularly due to its superior spin polarisation over Ni, widely studied in FM/I/FM structures. Here we have directly observed that the presence of Fe in this alloy also reduces the amount of diffusion of the metal layer into bulk materials. Hence it is also expected that NiFe/Ox/SC stacks will be more resistant to Ni analogues and therefore more suitable for annealing treatments and processing typical to semiconductor device fabrication techniques.

Lastly we look at a NiFe/Al2O_3/Ge stack. A stepped (30 minutes) anneal at temperature intervals 30 °C, 200 °C, 250 °C, 300 °C, 350 °C, 375 °C, 400 °C and 425 °C, encouragingly showed no significant changes. The appearance of a slight Ge 3d peak at T>375 °C was attributed to the removal of atmospheric C surface contamination commonly seen in XPS. This was corroborated by the disappearance of the C 1s peak with the initial emergence and the constant intensity of the Ge 3d peak.

Long (18 hour) RTA XPS scans at 345 °C and 450 °C, revealed no changes to the spectra. It was only at 475 °C, after over 3.5 hours of annealing when there were detectable changes of Ge and Al. The evolution of elemental concentration at 475 °C is plotted in figure 5.9. Even when there was a growth of Ge concentration, levels remained relatively stable for another 2.5 hours, before rapid diffusion and segregation indicated a complete breakdown of the barrier. This intermediate stage of slow growth could be diffusion of Ni and Fe through pin holes in the oxide layer.

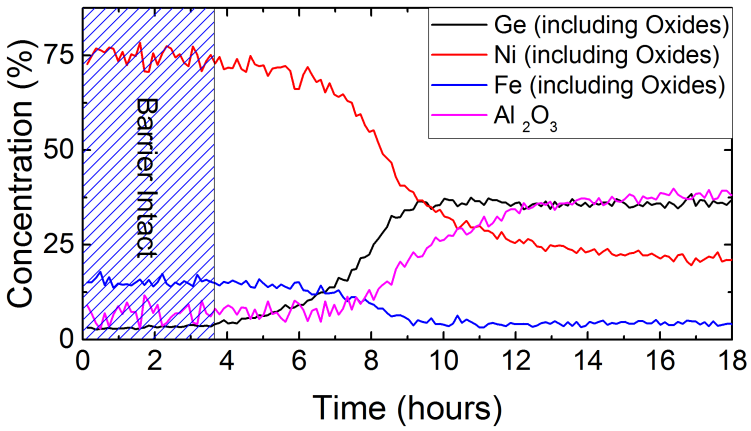

Figure 5.9: Top: A plot of Ge, Ni, Fe (combined element and oxide) and Al_2O_3 concentrations against annealing time for the Ni/Al_2O_3/Ge stack, at 475 °C. The blue shaded reason covers the time periods in which atomic concentrations appear to be stable, reflecting ratios consistent with intact FM/Barrier stacks.

Minimum Barrier Thickness

We have seen that even at these relatively low temperatures, the oxide barriers used are susceptible to damage from Ni and Fe diffusion into the bulk. The robustness of a barrier is clearly sensitive to the thickness of the layer, with thicker layers providing more protection from diffusion. The effectiveness of spin injection however is also highly sensitive to the thickness of the tunnel barrier, where thinner barriers provide larger tunnelling probabilities, thicker barriers with a larger resistance-area product have been shown to produce larger spin accumulation in electrical Hanle measurements [100] and larger thicknesses stop tunnelling processes all together. Most electrical Hanle experiments use barrier thicknesses of 0.5 nm$< t <$3 nm, here we look at MgO/NiFe/Pd stacks sputtered on Si and epitaxial Ge and annealed at 375 °C for 60 minutes. The annealing temperature and duration was selected to match similar conditions used in our current processes used to fabricate ohmic contacts to Ge QW. Three different thicknesses were used for the MgO layers (intended thickness 1 nm, 2 nm, 3 nm), where the NiFe and Pd layers were kept constant at 20 nm. These samples will be referred to as Ge samples 1-3 and Si samples 1-3, 1 denoting the thinnest barrier and 3 the thickest. A diagram of these structures are shown in figure 5.10.

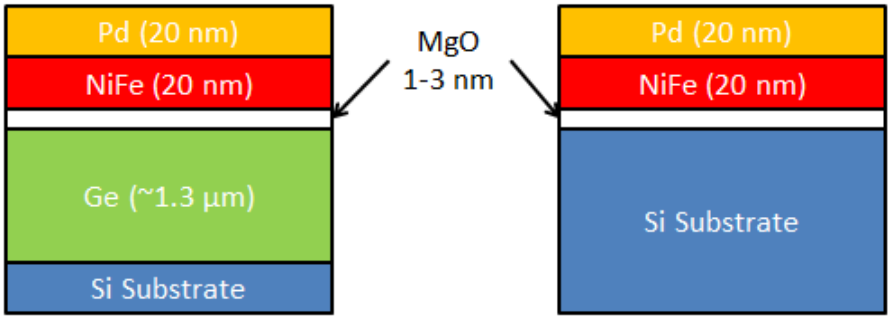

Figure 5.10: A diagram of the type of structures used in the MgO thickness XPS annealing studies.

The wide range survey scans for the Ge samples are shown in figure 5.11 with associated Ge, Mg, Ni, Fe, Pd, C and O peaks labelled. The C 1s peak located at ∼284 eV is routinely observed in XPS measurements when the sample is not annealed in-situ and is associated with atmospheric contamination. The presence of a strong Mg KLL Auger peak in only Ge sample 1 suggests that the Mg from the barrier layer had segregated towards the surface, on performing higher resolution scans about the Mg 1s peak (∼1300 eV) a signal peak was only observed for Ge sample 1. In addition to this, Ge sample 1 survey scan also contains significantly weaker Ni, Fe and Pd peaks and enhanced Ge peaks due to significant diffusion of the upper two layers into the bulk.

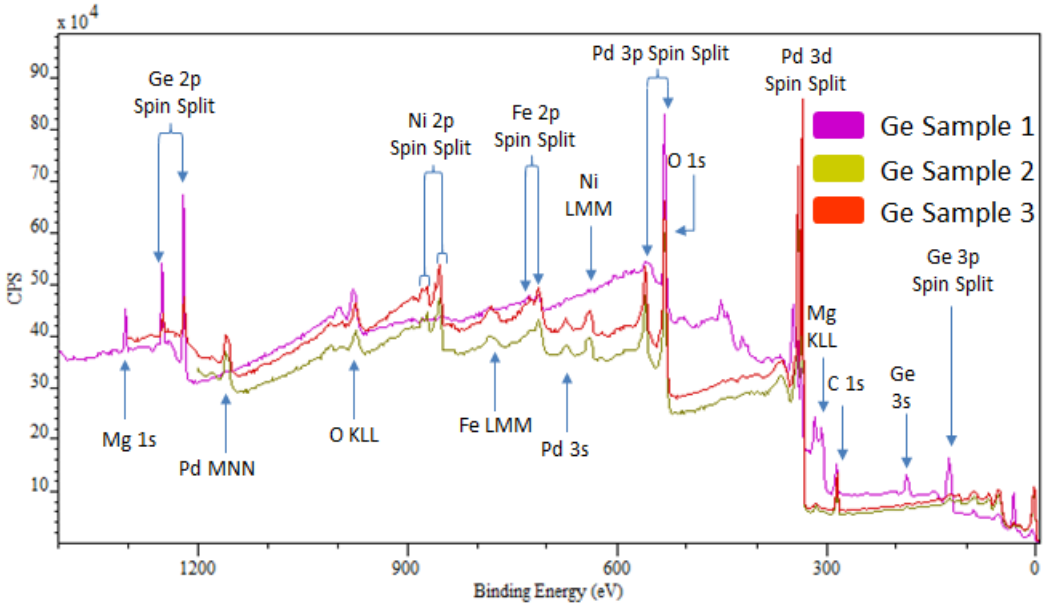

Figure 5.11: XPS survey spectra for Ge samples 1, 2 and 3.

The survey scan for the Si samples (figure 5.12) gave similar results. The Ni peaks were noticeably reduced in Si sample 1 when compared to samples 2 and 3, however Fe and Pd associated peaks showed only minimal to no reduction. The total absence of Mg and Si peaks for all three samples suggest that only Si sample 1 experienced a breakdown in the MgO barrier. The Si 2s and 2p peaks should be

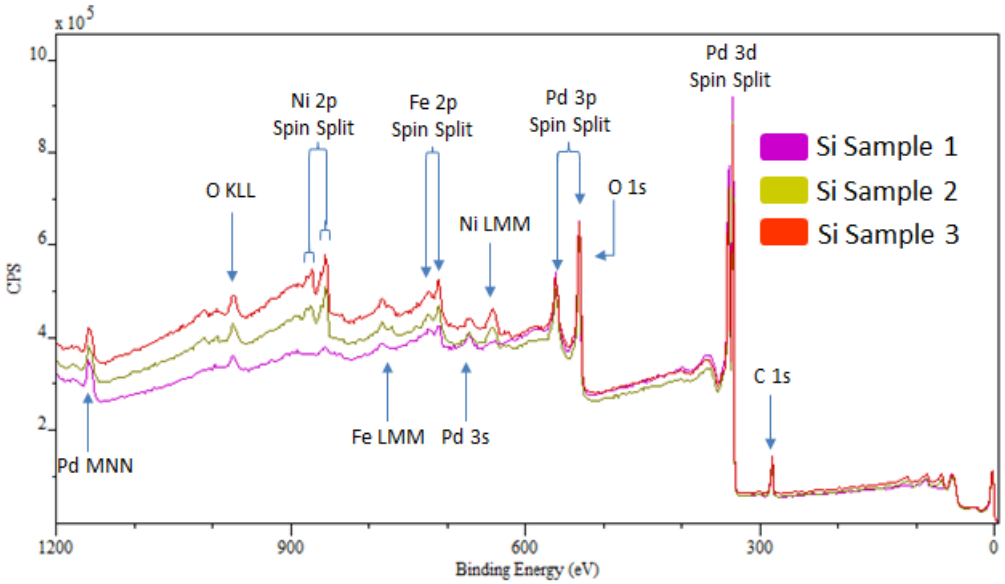

Figure 5.12: XPS survey spectra for Si samples 1, 2 and 3.

in principle visible in this scan range but are located at very low binding energies (<160 eV) and thus will be obscured by other peaks such as the Ni 3s and Mg 2s peaks. The absence of the MgO KLL Auger peak suggests that segregation of Mg towards the surface is a slower process.

High resolution (HR) X-TEM was performed on the Ge samples and is shown in figures 5.13, 5.14, 5.15 respectively, we find the micrographs obtained, agree with the XPS analysis. The three deposited layers in sample 1 are not distinguishable, instead only the bulk Ge and a darker, non-uniform layer with thickness 100-120 nm. It is clear from this that the sample experienced significant diffusion and intermixing particularly due to the large deviation of thickness of this layer from the expected total combined thickness of 40 nm. The uniform contrast across this layer also indicates that the atomic concentrations of the deposited materials are equally distributed.

HR-X-TEM on Ge sample 2 and 3 shows that the barriers remain intact following the annealing process, measuring at 3.3 nm and 3.7 nm. Atomic resolution of sample 2 shows a highly crystalline Ge layer with close to an atomically smooth

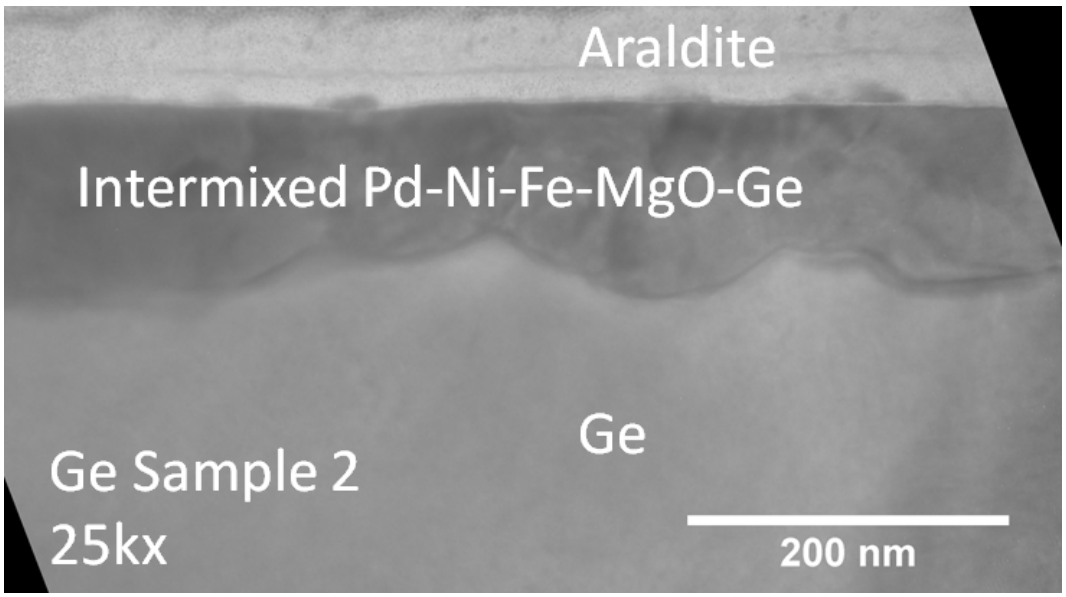

Figure 5.13: A X-TEM micrograph of Ge sample 1. The MgO/NiFe/Pd sputtered layers have diffused into the bulk forming a 100-120 nm layer. The uniformity of contrast in this upper most layer suggests that this intermixed layer has uniform density.

interface with the MgO layer and an NiFe/MgO interface with similar smoothness. The majority of the MgO layer in the micrograph is amorphous, however regions of order can be seen, most notably in the bottom-right in figure 5.14 (circled). This is corroborated by the (004) DF micrograph of sample 3 in which areas of the MgO layer are visible. The Pd and NiFe layers, however, were indistinguishable from each other due to the intermixing of the two layers. This limited improvement of the barrier indicates that either higher temperatures or longer annealing times are required for significant improvements, however caution is required in regards to the capping layer to prevent intermixing of a non-magnetic material into the FM layer below.

The limited transition to partially polycrystalline MgO is promising for the prospect of easily deposited, higher quality spin tunnel barriers, although longer annealing times may be required. This process however, sets a lower limit to barrier

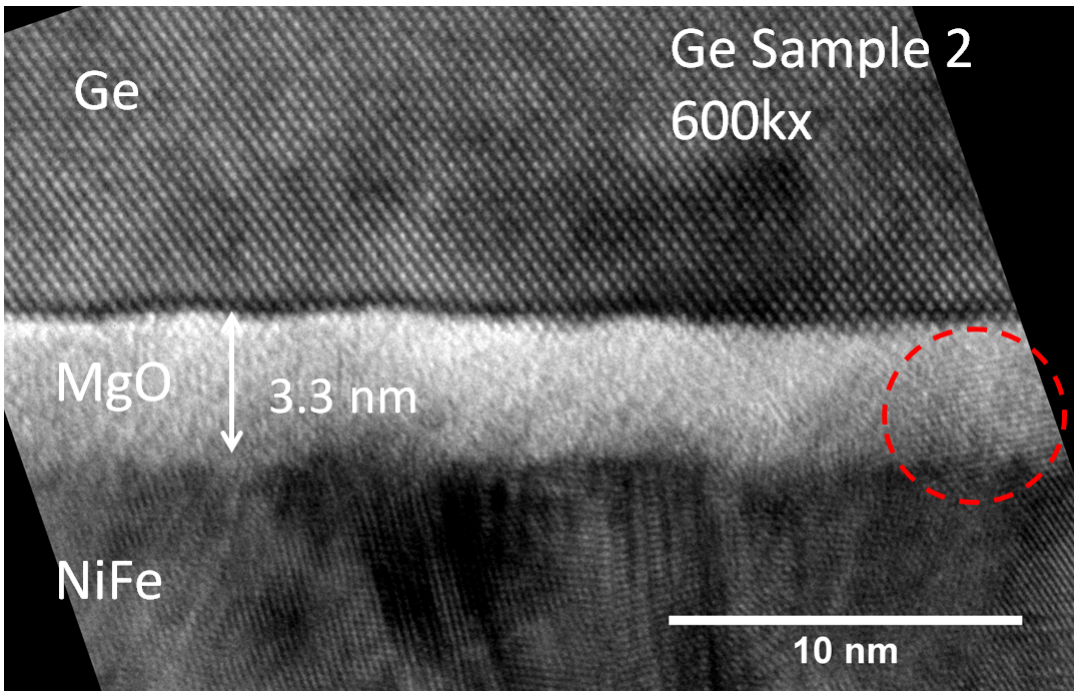

Figure 5.14: HR-X-TEM of Ge sample 2, showing the NiFe/MgO/Ge stack. The Ge appears to be fully crystalline, whilst multiple crystalline domains are visible in the NiFe. The MgO layer is atomically smooth at both interfaces, with some areas of the MgO appearing to have some order (noticeably on the right side of the micrograph) suggesting the beginning of a transition into a polycrystalline phase.

thickness and suggests that the thinnest barriers of ∼1 nm may not be used in fabrication processes in which annealing is required for other fabrication stages. One example being devices requiring ohmic contacts on buried quantum wells which typically use similar temperatures to diffuse contact material into the heterostructure to provide direct contact. Sputtered MgO may therefore be an unsuitable spin tunnel barrier material to use in 2D Ge/SiGe systems which are favoured in semiconductor spintronics for spin manipulation based devices.

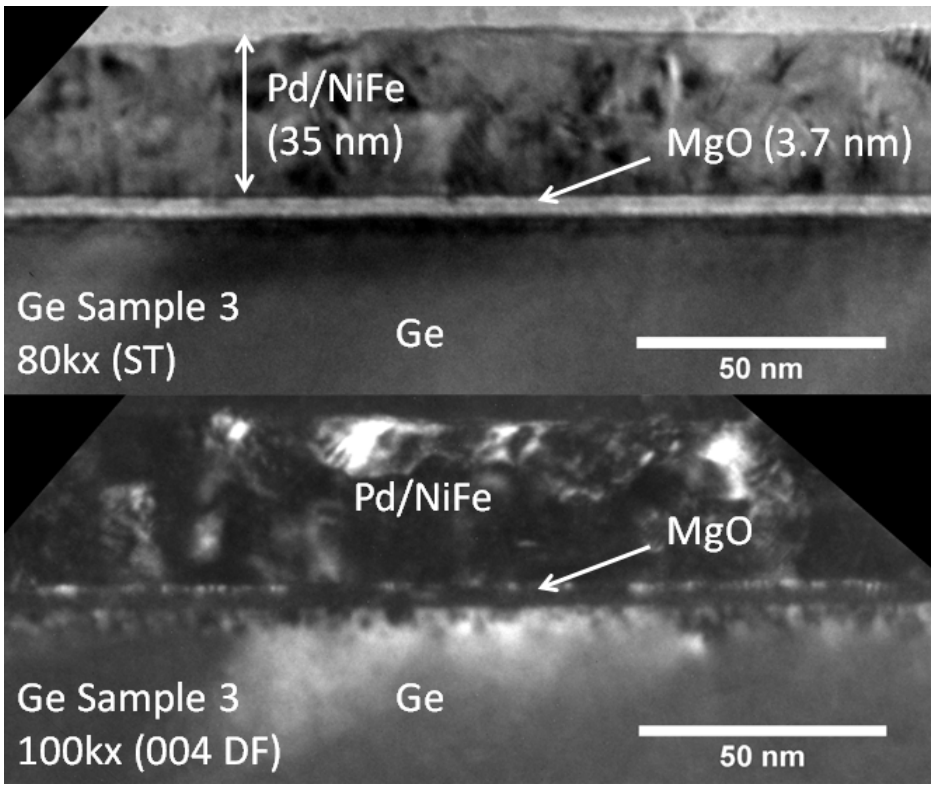

Figure 5.15: HR-X-TEM of Ge sample 3, in the ST-condition (top) and (004) DF-condition. The MgO barrier remains intact and uniform post annealing, the Pd/NiFe layer appears as a single polycrystalline layer. In diffractive mode the areas of the MgO is visible due to areas of crystallinity.

5.2 Electrical Properties of Ferromagnet/Oxide Tunnel Contacts

Next we briefly look at the electrical properties of annealed FM/Ox contacts on n-Ge. The bulk Ge material was grown on p-Si substrate (with resistivity 1-20 Ωcm), an initial 1.25 μm i-Ge (with background P-doping of $<1\times10^{15}\,\mathrm{cm}^{-3}$) followed by either a 50 nm n^+ Ge region with P-doping $0.5\text{-}1\times10^{-19}\,\mathrm{cm}^{-3}$. The devices used in this study were TLM type structures. These consisted of a series of identical 50 μm×150 μm contacts spaced by increasing distances from 1-512 μm on a rectangular mesa.

5.2.1 Fabrication of TLMs

The devices were fabricated by UV-lithography, in which the contacts were defined in the first stage of fabrication and the mesa last. The process and fabrication parameters are identical to those used in the Hall bar fabrication process discussed in chapter 4. The contacts consisted of an oxide layer (Al_2O_3 or MgO) of variable thickness, a 100 nm FM layer (Ni or NiFe) and a 5 nm NM cap (Au or Ti), deposited using e-beam evaporation, without breaking vacuum (10^{-7} mbar) between depositions. In addition to this, simple NiFe (sputtered) and Ni (e-beam evaporated) contacts were also fabricated. As above, the deposition rates used were 0.2 Å s^{-1} for oxides and 0.5 Å s^{-1} for metals.

An optical micrograph of a TLM device is given in figure 5.16. As stated before, the device designed contained a minimum contact separation of 1 µm. When developing the contact pattern in resist, the thinner areas of resist between contacts were susceptible to lifting off the surface or bowing, forming large or deformed contacts as seen in figure 5.16. This effect was worsened by difficulty in minimising the distance between the patterning mask and resist surface, if this distance is too large the UV incident on the exposed resist spreads out into a larger area than intended. A reduction of UV exposure energy density results in a less stable negative resist. Deformed contacts were omitted from measurements.

The fabrication mask used also included CTLM structures, which allow for TLM type measurements without the use of a defined mesa. These devices consist of a series of concentric ring contacts (of width 50 µm) with increasing contact separation (8 µm$> s >$512 µm). The mesa in a standard TLM is required to define and restrict current paths between contacts, in a circular configuration, the current is expected to flow radially. Both TLM and CTLM measurements assume the contacts are ohmic. Here we use TLM devices to study the contact resistance-area product (RA), although the contacts are not ohmic, we take the resistance from the low voltage range where the I-V curves appear to be linear. When plotting the

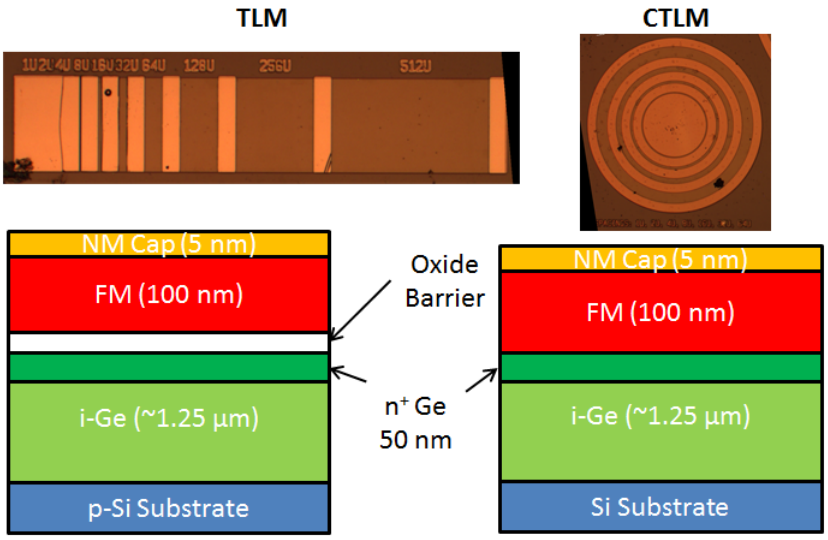

Figure 5.16: Top: An optical image of a TLM and CTLM device. The deformed/large contacts on the left side of the TLM device is a result of the thinner areas of patterned resist bending or lifting off completely. Bottom: Cross-sectional schematics of the TLM contact/mesa structure for both FM-tunnel contacts (left) and FM-metallic contacts (right).

RA against contact separation, the intercept at $s = 0\,\mu$m is double the RA of the contact material. CTLM devices proved to be unsuitable for measurements extracting RA involving the tunnel contacts studied here, this will be discussed in section 5.2.3. Due to equipment faults during the study, not all devices underwent dry etching to form a mesa, for the inclusion of all samples we therefore compare only I-V characteristics of a CTLM contact measurements with $s = 32\,\mu$m then examine the extracted contact-RA (R_cA) from TLM type devices.

5.2.2 HR-X-TEM Analysis of Oxide Barriers

HR-X-TEM was performed on a number of different samples to confirm the thickness of layers and the quality of the FM/Ox/Ge interfaces. The X-TEM samples were obtained by simultaneously evaporating tunnel contact material on both patterned Ge to be processed into the TLM devices and a blank Ge wafer piece (from the same wafer) which were then prepared as described in section 3.2.2.

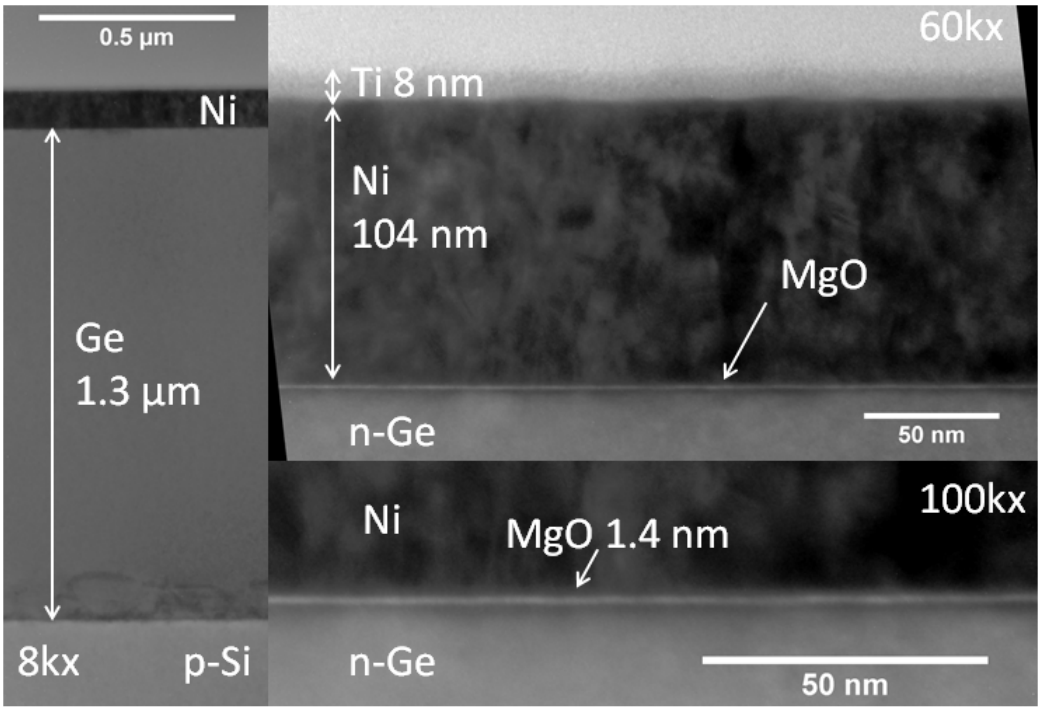

Figure 5.17: HR-X-TEM micrograph images in the straight through condition of a Ti/Ni/MgO stack e-beam evaporated on Ge/Si. Left: 8k magnification showing the complete structure. Mismatch dislocations are localised at the Si/epitaxial Ge interface. Upper Right: 60k magnification of the evaporated material, the MgO layer is visible as a thin uniform white line. Bottom Right: 100k magnification at the MgO interface, measuring at a total thickness of 1.4 nm. The dark edge below the MgO is a fringe effect from the focusing of the image.

The complete cross-section of a Ti/Ni/MgO on Ge is given in figure 5.17. At 60k magnification the complete tunnel contact stack is visible, although the thickness of the prepared X-TEM sample has limited the available resolution. The thickness of the upper Ti and Fe layers are close to the intended values. The MgO layer appears as a white line separating the dark coloured Ni and the lighter Ge. It is important to note that the dark line visible between the MgO and Ge layer is not a separate layer but a fringe effect from focusing and sample thickness. The MgO layer appears to be uniform in thickness at ∼1.4 nm, however due to the limited resolution of this sample, the roughness of the interface cannot be commented upon.

The cross-section of a 3 nm Al_2O_3 barrier, with Ni electrode and Ti cap is

shown in figure 5.18. At 80k magnification, the oxide layer appears to be uniform in thickness. Both the Ni and Ti layers are seen to have rough surfaces with valleys as deep as 4 nm. At 500k magnification, (right side of figure 5.18) atomic resolution of the Al_2O_3 interface is given, revealing a fully crystalline Ge layer and multiple orientations of ordering in the Ni (polycrystallinity). The Al_2O_3 layer is as expected, amorphous, with a relatively smooth Ge interface with a variation of only 1-2 atomic plains in this section of the sample. The Ni/Al_2O_3 interface however is rougher, this roughness is problematic as the variation in thickness across thin samples can produce shorting. Further complications arise when considering these structures for spintronic applications. The interface roughness of the barrier and FM-contact introduces localised out-of-plane fields which contribute to increased spin relaxation at the interface.

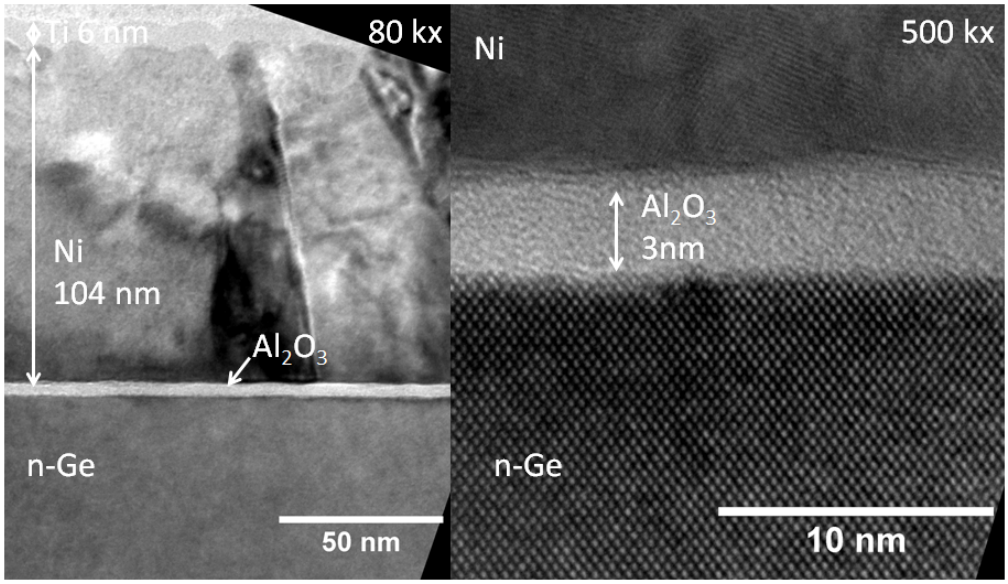

Figure 5.18: HR-X-TEM micrograph images in the straight through condition of a Ti/Ni/Al_2O_3 stack e-beam evaporated on Ge/Si. Left: 80k magnification at the surface of the Ge sample. The surface of the evaporated Ni appears to be rough, with the deposited Ti conforming to the Ni morphology. At this magnification, the Al_2O_3 is fairly uniform in thickness. Right: 500k magnification at the oxide interface with atomic resolution. The Ge is fully crystalline, whilst the Ni layer contains multiple orientations of crystal order. The Al_2O_3 is amorphous and has a thickness of $\sim$3 nm.

5.2.3 Current-Voltage Characteristics and Contact Resistance

Ideally, the I-V characteristic of a tunnel junction should be measured between the tunnel junction and an ohmic contact, this may either be done in a lateral configuration with both tunnel and ohmic contacts on the surface, or vertical configuration, where an ohmic back contact is used. Unfortunately, due to the design of the mask, a lateral measurement is not available and the vertical configuration is also made difficult due to the use of a p-type substrate. When growing n-Ge on Si, it is common practice to use a p-Si substrate, this in effect creates a p-n or p-i-n junction for the purpose of preventing leakage currents through the substrate. This effective p-i-n junction, will dominate the I-V characteristics in the vertical orientation and thus it cannot be used. Instead I measure the I-V characteristics between two tunnel contacts. As stated before, the use of tunnel barriers is to remove or significantly reduce the effect of a Schottky barrier. The I-V characteristic of a Schottky contact in practice is asymmetrical, however when measuring an I-V curve between two Schottky contacts, the contacts will always be in opposite biases regardless of the direction of the voltage bias, this results in symmetrical tunnel-like I-Vs.

First I look at the effect of the barrier thickness on the I-V characteristics between two concentric ring contacts from CTLMs (contact separation of 32 μm). The devices measured have a Ti/Ni/Al_2O_3 stack on n-Ge with P-doping concentration $5 \times 10^{-18}\,\mathrm{cm}^{-3}$ and barrier thickness $0\,\mathrm{nm} < t < 5\,\mathrm{nm}$. I-V measurements were taken by sweeping voltage (from negative to positive) and measuring current using a Karl Suss PM5 electric probe station and an Agilent 4156C precision semiconductor parameter analyser. The curves for these devices, including repeat measurements are given in figure 5.19.

All contacts displayed symmetric tunnel junction-like behaviour including a plain Ni contact. The linear region at low voltages ($|V| < 0.1\,\mathrm{V}$) was fitted to extract the low voltage resistance and plotted against Al_2O_3 thickness in figure 5.20. The thinnest barriers with $t \leq 3\,\mathrm{nm}$, appear to make little difference to the low

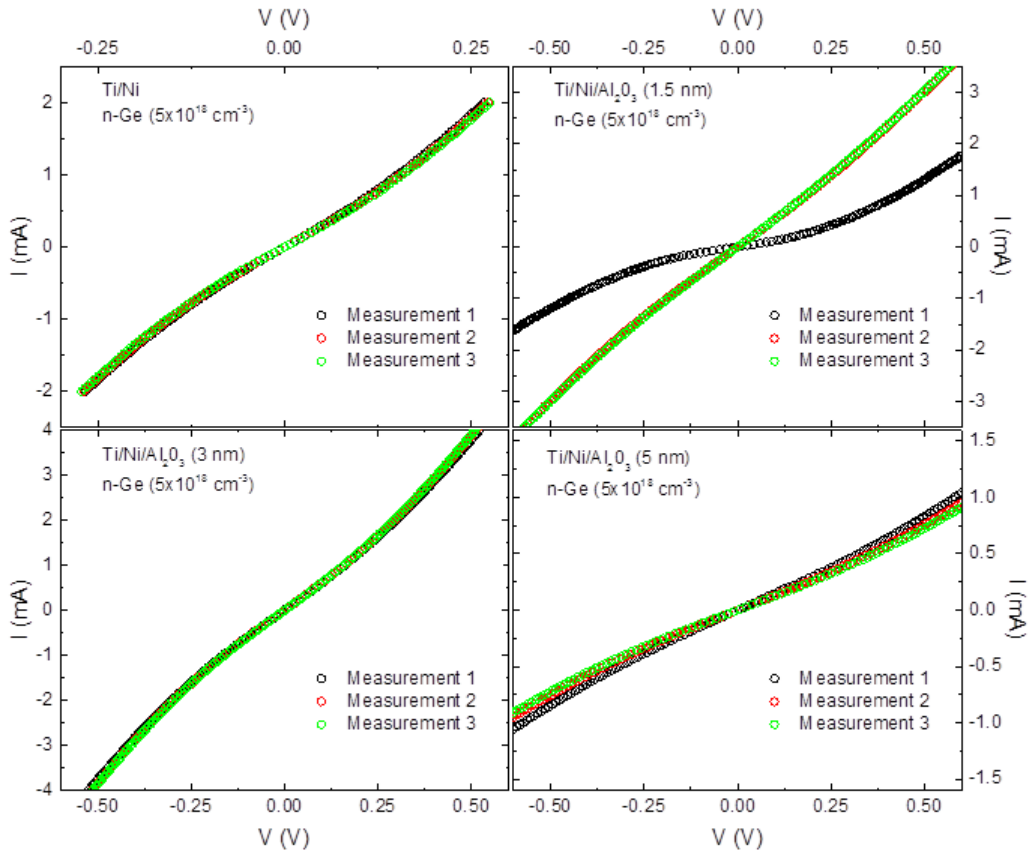

Figure 5.19: I-V characteristics of CTLM contacts with 32 µm separation for Ti/Ni (top right) and Ti/Ni/Al_2O_3 with oxide thicknesses 1.5 nm, 3 nm, 5 nm (top right, bottom left, bottom right respectively) on n-Ge. Multiple measurements for each device is plotted, with some devices showing fluctuations in I-V characteristics.

voltage resistance, all three sharing similar values of $R \sim 0.2\,\mathrm{k\Omega}$ to the simple Ti/Ni contact. At $t = 5\,\mathrm{nm}$ we finally see a jump in resistance to $\sim$0.75 kΩ. The resistance of a FM/Ox/SC contact is expected to be highly sensitive to barrier thickness due to the exponential decay of the tunnelling probability with increasing thickness. This sensitivity to barrier thickness in this range has been demonstrated for similar structures in Si reference [100], for which an exponential increase in the RA was observed with growing thickness. The stable low voltage resistance of these contacts is therefore surprising, particularly as X-TEM micrographs of the 3 nm barrier (figure 5.18) show a uniform oxide layer of the correct thickness. The stable value

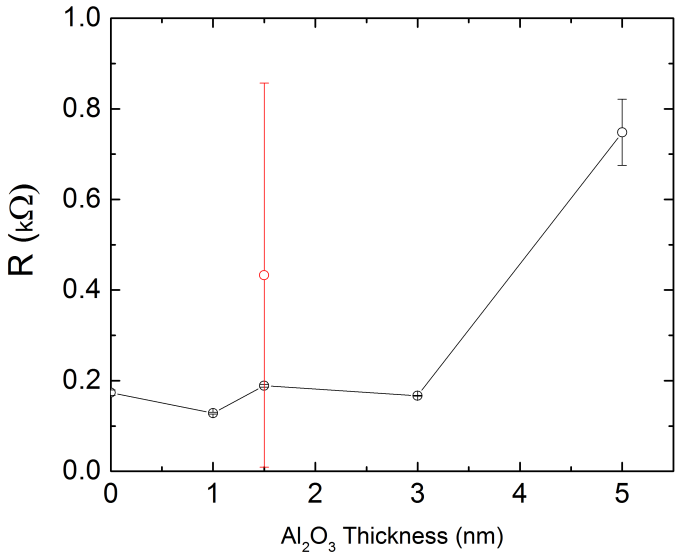

Figure 5.20: Resistance as a function of oxide thickness for the CTLM contacts with 32 µm separation for Ti/Ni/Al_2O_3 on n-Ge. The resistance was extracted by fitting a straight line at low voltages. Larger errors denote contacts with significant variations in repeat measurements, the red circle marks the value of R when the anomalously large resistance was measurement is included.

in R suggests that the Schottky barrier at thicknesses 3 nm and below dominates the contact resistance.

It is important to note that there was a slight variation in I-V characteristic for the 5 nm Al_2O_3 device between variations and a noticeable variation in the 1.5 nm Al_2O_3 device, between the initial measurements and repeats. This instability in contact resistance will be discussed in section 5.2.3.

Additional devices in the TLM configuration were also measured and the contact resistance-area product (R_cA) was extracted by halving the RA value at $s = 0\,\mu$m. Four different sets of devices were investigated:

- Ni/Al_2O_3 on n-Ge (P-doped $5\times10^{18}\,cm^{-3}$) with barrier thicknesses: 0 nm, 2 nm, 3 nm, 5 nm.
- Ni/MgO on n-Ge (P-doped $5\times10^{18}\,cm^{-3}$) with barrier thicknesses: 2 nm,

20 nm.

- Ni/Al_2O_3 on n-Ge (P-doped $1\times10^{19}\,cm^{-3}$) with barrier thicknesses: 0.5 nm, 2 nm.
- $NiFe/Al_2O_3$ on n-Ge (P-doped $1\times10^{19}\,cm^{-3}$) with barrier thicknesses: 5 nm, 8 nm.

The TLM plots for contacts with Al_2O_3 and MgO barriers are given in figures 5.21 and 5.22 respectively. A number of plots can be seen to follow the expected linear relationship closely, others however contain large amounts of deviation, particularly for the MgO based contacts. The plotted RA values are averages of multiple measurements, thus the error in RA reflect the variation in I-V characteristics on repeat measurements. The extracted R_cA values for the Al_2O_3 based contacts are plotted as a function of barrier thickness (t) in figure 5.23. Apart from the 5 nm Ni/Al_2O_3 structure, all three oxide thicknesses displayed an increase in contact resistance with oxide thickness. The large variation in the 5 nm oxide sample likely results from inaccuracies due to the deviation of a linear RA behaviour, a lack of data points and large deviations of resistance measurements at the largest separation, as visible in figure 5.21. Unlike its CTLM counterparts, the Ni/Al_2O_3 on the lower doped n-Ge, an increase in contact resistance from the pure Ni contact to the 2 nm barrier contact is seen, contradicting previous I-V measurements from CTLMs on the same die. The scaling of resistance with oxide thickness however is inadequate to describe a purely direct tunnelling contribution where a 1 nm difference in barrier thickness often results in a difference in RA of several magnitudes [100]. The tunnel contacts on the higher doped n-Ge were generally less resistive, due to the reduction of the Schottky barrier depletion width, but also showed marginal scaling of R_cA with thickness that was far less than the lower doped Ge contacts.

The lack of sensitivity of R_cA to oxide thickness, even on highly doped Ge, where influences of the residual Schottky barrier is kept to a minimum is worrying,

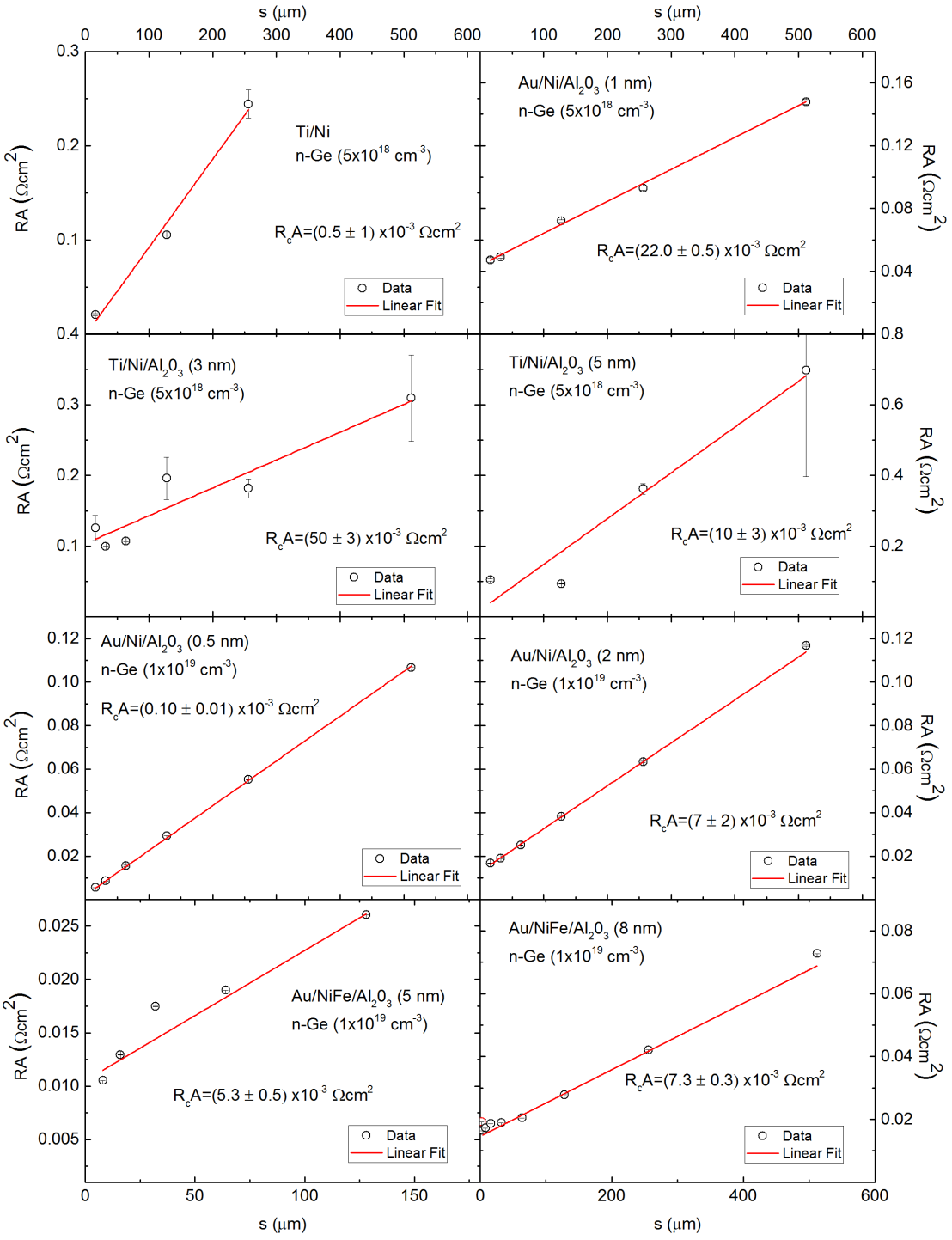

Figure 5.21: TLM plots of Ni/Al_2O_3 and $NiFe/Al_2O_3$ contacts on n-Ge. The size of error bars indicate the degree of variability between repeat I-V measurements.

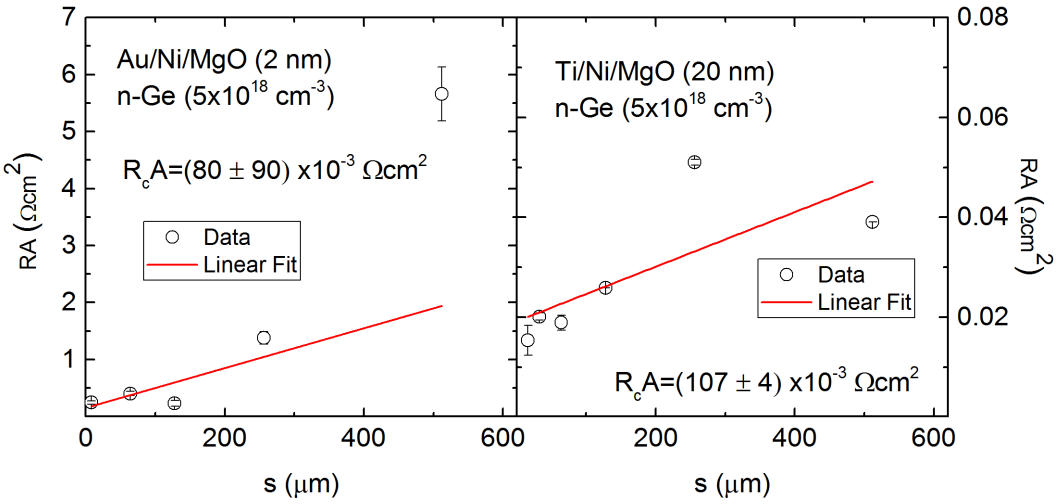

Figure 5.22: TLM plots of Ni/MgO contacts on n-Ge. The size of error bars indicate the degree of variability between repeat I-V measurements.

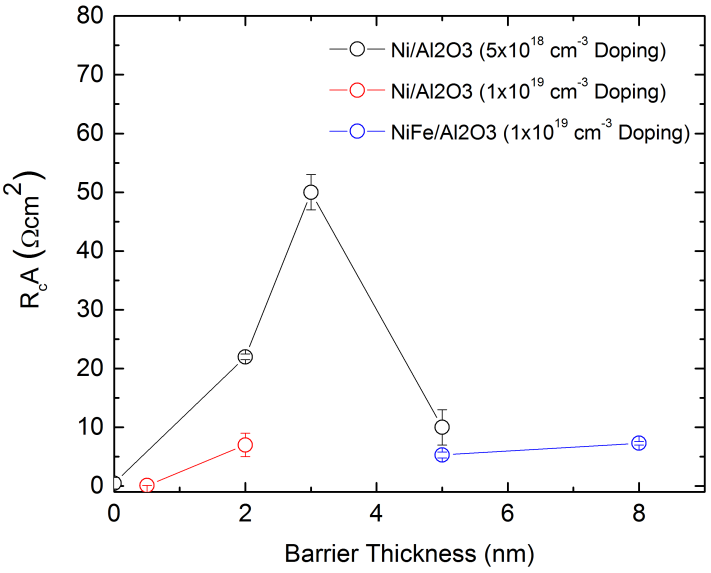

Figure 5.23: Contact RA against oxide thickness for the Ni/Al_2O_3 and $NiFe/Al_2O_3$ TLM devices on n-Ge.

suggesting untreated e-beam deposited tunnel contacts exhibit other processes in parallel with direct tunnelling. Furthermore, the discrepancies between TLM and CTLM devices fabricated on the same die also indicate inhomogeneity in the oxide barrier layer across the sample. One source for additional conduction processes through the barrier may be the inclusion of pin holes in the dielectric, which evaporated Al_2O_3 is known to suffer from. When sufficiently thin, pin holes can penetrate through to the substrate and provide direct current paths to the substrate. Despite the uniformity and absence of voids in the X-TEM micrographs (figure 5.18), only a small region (of length 200 nm) is observed, this is highly localised and may not give an accurate account for the majority of the sample. If the density of pin holes and therefore leakage is significant it may explain why the devices experience a weak resistance dependence on oxide thickness.

Electrical Instability of Tunnel Contacts

We will now discuss the reliability and reproducibility of these structures. The shift in I-V characteristics visible in the 1.5 nm barrier sample (figure 5.19) was also visible in multiple devices (CTLM and TLM) for various oxide thicknesses, the shift was observed to occur both between and during voltage sweeps. Figure 5.24 displays further measurements on the 1.5 nm barrier device (sweeping current and measuring voltage). Multiple shifts are seen to higher and lower resistances on repeats with low voltage resistances in the range $0.69\,\mathrm{k\Omega} < R < 5.7\,\mathrm{k\Omega}$. On the initial measurement, we observe a shift to a lower resistance upon reaching $I \sim 0.4\,\mathrm{mA}$ ($V \sim 0.7\,\mathrm{V}$), then reducing again for the duration of the second measurement. Further switching occurs between resistances during the third sweep, first to a higher resistance state at $I > -0.55\,\mathrm{mA}$ ($V > -1.4\,\mathrm{V}$), then to a lower resistance state at $I > 0.64\,\mathrm{mA}$ ($V > 0.7\,\mathrm{V}$). The final measurement, produced a continuous curve with similar resistance to measurement 3.

Extensive I-V measurements in multiple devices that exhibited significant

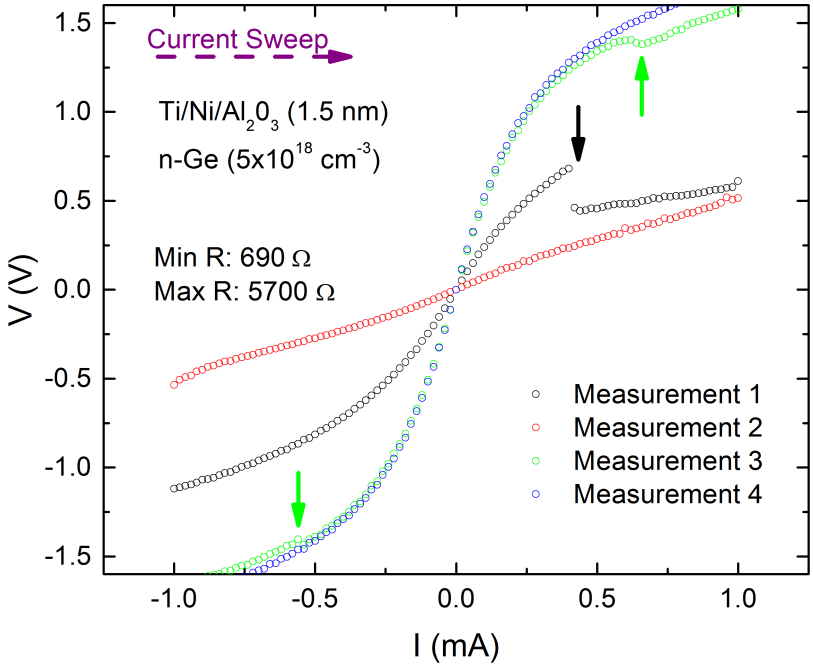

Figure 5.24: An extreme example of resistance switching between and during repeat I-V measurement sweeps for an Ti/Ni/Al_2O_3 on n-Ge CTLM contact (32 µm separation). The green and black arrows indicate points at which the contact experiences a shift in I-V characteristic during a measurement.

shifts in contact resistance revealed a number of trends:

- Shifts in I-V characteristics during sweeps often occurred at higher voltages ($|V| > 0.4\,V$).
- Longer integration/sampling time encouraged multiple switching behaviour in a single sweep.
- CTLM devices were more susceptible to unstable I-V characteristics, even when fabricated along side TLM devices.
- TLM and CTLM contacts with large separations experienced instability more often.

The first and second observations point towards the origin of the anomalous behaviour. A change in I-V characteristic or resistance in a NM/Ox/SC system refers to a change in the dielectric properties. Oxide dielectrics can trap charges either in the layer itself (oxide trapped charge and fixed oxide charge) or at the interface (interface trapped charge) [106]. Fixed oxide charge refers to oxygen vacancies due to oxygen deficiency in evaporated Al_2O_3, leading to dangling Al bonds. Oxide trapped charges on the other hand, can come from either trapped ion impurities or broken bonds in the oxide, significant occupation of these traps could lead to a change in the capacitance. The presence of oxide trapped charges inside the barrier can distort the electric field within the barrier to enhance Fowler-Nordheim tunnelling and therefore leakage [106].

Interface trapped charges originate from positive and negative charges located at the Ox/SC interface due to structural defects, impurities and other surface damage [106]. These charge centres can trap or discharge carriers depending on the surface potential, thus the shift in I-V characteristics at higher voltages could be a result of the charging/discharging of these interface states. The nature of these traps can be probed using capacitance-voltage (C-V) measurements and annealing treatments. Due to time restrictions, the study did not extend to these measurements.

The increased frequency at which the switching occurred for large separations and for CTLM type contacts is an indication of inhomogeneity in oxide quality. If the distribution of pin holes and charge traps is only homogeneous in short ranges, the discharging/charging processes inside the oxide and at the interface, as well as the degree of leakage current will be asymmetrical and prone to shifting. This is enhanced for CTLM devices as the contacts are of different areas and span over larger areas of the sample surface than the TLM devices.

5.3 Summary

In this chapter I investigate the viability of using cheap, widely available deposition tools for both research purposes and large scale industrial fabrication of spin tunnel contacts on semiconductors. An annealing study was performed for a number of combinations of FM electrodes (Ni and NiFe) and thin insulating oxide layers (Al_2O_3 and MgO), deposited by e-beam evaporation and sputtering to find the maximum annealing temperature allowed for the preservation of the thin oxide barriers. XPS measurements were utilised to monitor the surface of the thin layers during the annealing process. Ni as a ferromagnetic electrode material proved to cause the breakdown of the oxide barrier through diffusion into the bulk Ge at much lower temperatures than NiFe. At low temperatures in the range 200 °C$< T <$300 °C, Ni was found to diffuse downwards, whilst Fe segregated towards the surface suggesting processes with long annealing times in this range should be avoided to preserve Ni:Fe ratios.

In terms of oxide barriers with a thickness of 1 nm (typical to those used in electrical spin injection into semiconductors) the Al_2O_3 was found to be more robust than MgO, failing at 350 °C after 45 minutes when a Ni electrode was used. With a NiFe electrode layer, the Al_2O_3 barrier was able to withstand an annealing temperature of 475 °C in excess of 2.5 hours. This is encouraging for future implementation of spin tunnel contacts in 2D Ge/SiGe heterostructures where annealing temperatures of 350-400 °C are used to form ohmic contacts with buried conduction channels. In contrast sputtered MgO layers required a minimum thickness of 3 nm to prevent diffusion of NiFe into the bulk Ge at 375 °C and only showed limited formation of crystalline regions post annealing.

Electrical measurements of these tunnel contacts without annealing, produced very poor tunnel contacts. Due to the symmetry of the measurements it was not possible to distinguish Schottky diode from tunnel behaviour, however the weak

dependence of oxide thickness on R_cA, suggested that the dominant conduction through the oxide layer was not tunnelling. Instead it is suspected that there is significant leakage through the dielectric. Furthermore a number of contacts exhibited instabilities shifting contact resistance between and during measurements. This shift is thought to be attributed by the filling and discharging of trapped charges either at the Ge/oxide interface or at oxygen vacancies due to oxygen deficiency.

I conclude that standard deposition techniques such as evaporation and sputtering may not be suitable for large scale fabrication as thicker oxide layers will be required if annealing processes are integral to the fabrication of devices. Although NiFe/Al_2O_3 remains a promising combination for these deposition techniques, issues associated with pinhole formation and charge trapping may hinder the performance of the tunnel contacts. Instead I propose the use of atomic layer deposition for the growth of thin Al_2O_3 barriers with smooth interfaces and lower pin hole density. Quality MgO barriers on the other hand may not be practical for industrial fabrication on semiconductors as it is only achievable through MBE growth for smooth, crystalline layers.

Chapter 6

Spin Lifetime Measurements in Ge

In the previous chapter, FM-tunnel junctions were developed using materials typical to spintronics, here I implement these tunnel junctions into Hanle devices for spin-like measurements in bulk n-Ge. A number of devices were fabricated over the course of this project, however due to the sensitive nature of spin tunnel junctions and the difficulty of fabricating them without adequate equipment, only two out of 200-300 devices fabricated have shown evidence of spin injection and detection in Ge. The two devices discussed, use either an Au/NiFe/Al_2O_3 FM-tunnel contact on P-doped Ge (n $\sim 1.4\times10^{19}\,cm^{-3}$) or an Au/Ni/$Al_2O_3$ FM-tunnel contact on P-doped Ge (n $\sim 5\times10^{18}\,cm^{-3}$) and will be referred to as samples 'A' and 'B'.

6.1 Material Characterisation

The material used in the spin lifetime study was a 50 nm n^+-Ge with a 1.2 µm i-Ge buffer, grown on a p-Si substrate (with resistivity 1-20 Ωcm). Although doping impurities enhance spin relaxation in bulk materials through EY spin relaxation, the n^+ layer also serves to lower the depletion width of the Schottky barrier at the

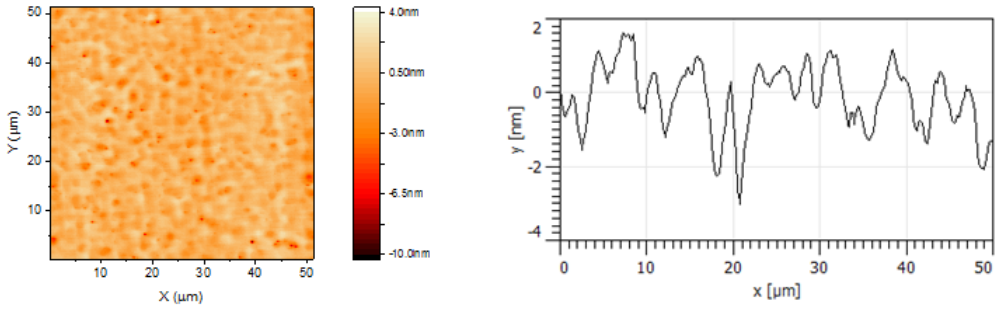

Figure 6.1: A 50µm×50µm AFM scan (left) of the sample and a line profile (right) taken through the centre (left to right) of the scan.

interface for improved tunnel properties. The doping level as confirmed by SIMS is $(1.1 \pm 0.2)\times10^{19}\,\mathrm{cm}^{-3}$ and $(5.4 \pm 0.7)\times10^{18}\,\mathrm{cm}^{-3}$ for samples A and B respectively and the i-Ge layer registering below the noise level $(5\times10^{16})\,\mathrm{cm}^{-3}$. The sensitive nature to interfaces in quantum tunnelling requires smooth and clean surfaces for fabrication. AFM scans gave an RMS roughness of (1.01 ± 0.01) nm, an example of one scan is given in figure 6.1.

6.2 Device Fabrication

The Hanle measurement device design is given in figure 6.2. The device consists of two 200 µm×200 µm ohmic contacts at either end of a 50 µm×250 µm mesa. Two FM tunnel contacts are placed close to the centre of the mesa bar with a separation of 2 µm. These two contacts are extended from larger 200 µm×200 µm contact pads either side of the mesa bar. The two FM tunnel contact arms have different widths, one 2 µm and the other 4 µm. The variation of the contact arm areas was initially decided upon to allow for differing coercive (due to geometric anisotropy) fields for possible spin valve measurements.

The VdP square devices used for MR and Hall measurements were fabricated using shadow evaporation. The mask consisted of a grid of circular contacts. The deposited contacts were annealed at 425 °C for 25 minutes in an N_2 atmosphere.

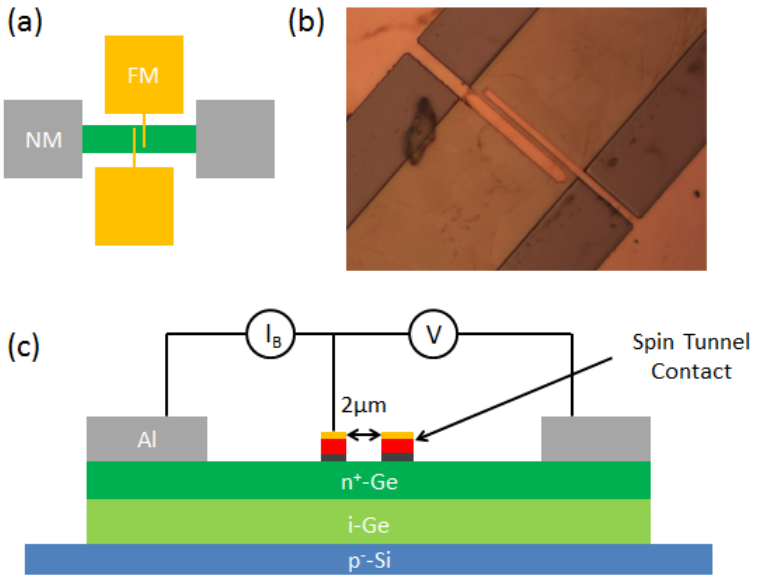

Figure 6.2: a)A diagram of the Hanle device design as viewed from above. b)Optical micrograph of the spin tunnel contacts of a fabricated device located in the centre of the mesa. c) A cross-sectional diagram of the device set up in a local 3T measurement orientation.

The annealed material was then cleaved along the row of Al dots and again in the perpendicular direction to produce squares with quarter dot contacts at each corner.

The fabrication process used for the Hanle devices was more complicated, resembling that of the one used for Hall bars in chapter 4. The ohmic Al contacts and the mesa patterning processes were identical to that used in the Hall bar method. An additional stage was inserted between the Al contact deposition and the mesa etch for the fabrication of the FM-tunnel contacts. This used the same negative AZ512E resist and exposure times. Prior to deposition, the surface was cleaned to ensure a suitable interface for the tunnel barrier, this is achieved using a 30 s plasma ash followed by a 2% HF dip. Electron-beam evaporation was used to deposit the three layer FM-tunnel contact stack in UHV (10^{-7} mbar), without breaking vacuum between layer deposition. The FM-tunnel contact stack for sample B consisted of a (2.7 ± 0.4) nm Al_2O_3, and 100 nm Ni FM, followed by a 5 nm Au cap used to prevent oxide formation on the contact surface. These thicknesses were confirmed

by X-TEM. For sample A, X-TEM was not preformed, however the layers and their target thicknesses are as follows: 5 nm Al_2O_3 ,100 $\pm$ 5 nm Ni and 5 nm Au.

The largest spin diffusion length recorded electrically in bulk n-Ge is 830 nm [29] at room temperature, where the majority of device designs favoured spacings under 1 µm [10][13][80][107]. The use of a 2 µm spacing between contacts was entirely due to the limitation of available fabrication facilities. Similar studies with non-local Hanle orientation employed e-beam lithography, where features down to 10 nm can be defined. While the lower limit of feature size in UV-lithography can be reduced down to hundreds of nm, this is routinely difficult and often requires highly fine tuned processing. The fabrication mask used included two Hanle devices with FM-tunnel contact separations of 1 µm and 2 µm, however only 2 µm devices were achievable. When considering existing spin lifetime measurements in Ge, this is relatively large and thus I do not expect to measure a noticeable spin signal. Although this design was intended for use with bulk Ge initially, the study was planned to extend to include low dimensional Ge heterostructures where routinely achieved mobilities (orders of magnitudes higher than bulk) are able to push spin diffusion lengths to higher and more relevant scales.

Standard Hall measurements using VdP squares were used to determine the transport properties of the n-Ge between 20 K-300 K. The temperature dependence of n and μ_H for both samples are plotted in figure 6.3. The measured parameters μ_H, n and ρ are summarised in table 6.1 for 20 K. Below 40 K, these transport parameters were constant and the 20 K values in table 6.1 were used for calculations regarding extraction of parameters from Hanle measurements at low temperatures.

	ρ (mΩcm)	n (1×10^{18} cm^{-3})	μ_H (cm^{2}V^{-1}s^{-1})
Sample A	1.5480±0.0003	14.4±0.1	281±2
Sample B	3.808±0.001	5.32±0.08	308±5

Table 6.1: The measured transport parameters of samples A and B at 20 K.

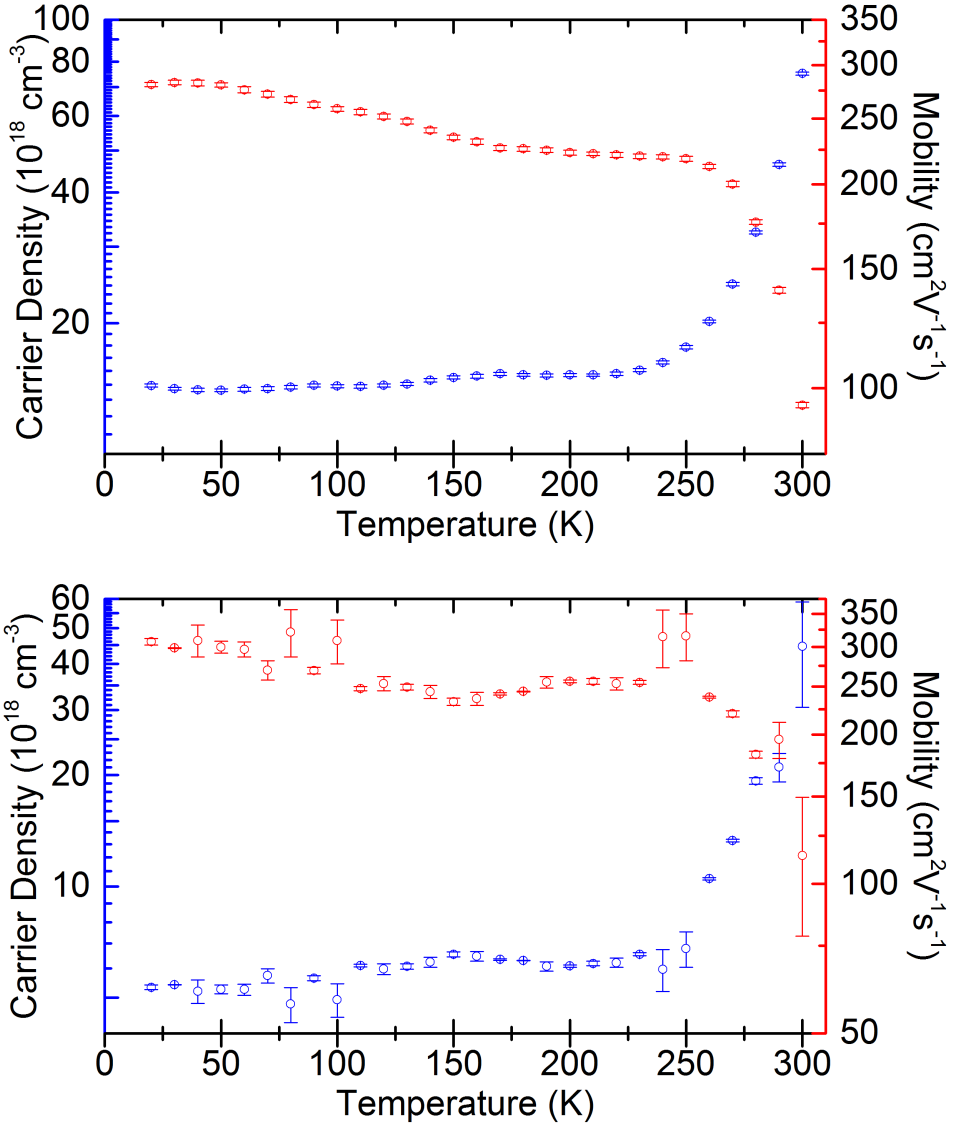

Figure 6.3: Plots of carrier concentration (n) and Hall mobility (μ_H) between 20 K and 290 K, measured from VdP squares for sample A (top) and sample B (bottom).

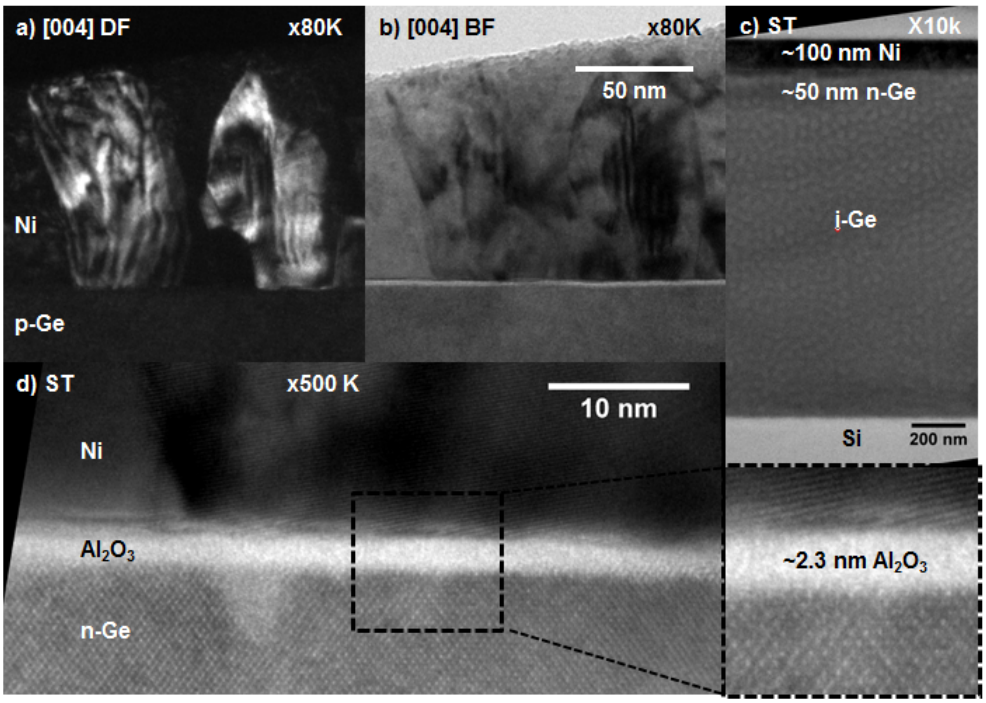

Figure 6.4: X-TEM micrographs of a Au/Ni/Al_2O3 contact. The following images are provided; contact/sample in the (004) DF (a) and BF (b) at ×80k magnification, ×10k magnification of the whole structure in ST condition (c) and ×500k magnification in the ST condition in the vicinity of the barrier (d).

6.3 NiFe/Al_2O_3/Ge Contact Quality

The thicknesses regarding deposited Ni and Al_2O_3 contact layers were obtained by X-TEM. The TEM sample was extracted directly from a device contact on the same die as the electrically measured device via FIB-SEM sample preparation. As the oxide barrier quality and thickness was of interest, no additional protective capping layers were deposited as the Ni/Au layers served as an adequate protective layer.

The (004) diffraction condition was used to confirm the crystallinity of the layers. Comparing the DF and BF (figure 6.4 a and b respectively), the Al_2O_3 layer is visible as a white uniform line in the BF condition, whilst in DF this layer vanishes. Its absence in the DF condition indicates that the layer is amorphous and thus the electrons passing through the layer cannot undergo diffraction. The Ni layer however, is clearly polycrystalline due to the numerous crystal domains

visible. At ×500k magnification a clearer image of the barrier is given, showing the relatively smooth Al_2O_3/Ge interface, the top interface however was not as well defined. Also visible is the lattice of the relaxed Ge for which no dislocations were visible. As the Ge was known to be fully relaxed, the lattice spacing were used to calibrate the length scale at this magnification.

Although no X-TEM micrographs were obtained for the NiFe/Al_2O_3 based device, the conditions used in its deposition was identical to that of the other Ni/Al_2O_3 device and similar devices studied in chapter 5, the quality the therefore taken to be similar.

6.4 Electrical Hanle Measurements

6.4.1 Experimental Setup and Methodology

The devices were measured in an Oxford Instruments Heliox AC-V He^3 cryomagnetic system at low temperatures, with the application of a magnetic field applied perpendicular to the plane of the device using a superconducting magnet. Both 4T and 3T device orientations were attempted. A Keithley digital 182 voltmeter was used to measure the potential difference between the detector contact and an ohmic reference contact, whilst a Keithley 2632A source meter provided a bias current between the second reference contact and the injector contact. In the 3T orientation, the detector and injector contact use the same electrode. The direction of the bias current dictated the nature of the spin accumulation, with a positive bias for majority spin extraction whilst a negative bias injected majority spin. As the field was swept, the source meter was used to measure the change in potential difference due to the field-induced relaxation/dephasing of non-equilibrium spins.

It is common in these experiments to also perform an inverse Hanle measurement where an in plane field is employed. This serves to negate stray random fields at the interface which can enhance spin relaxation and reduce accumulation [28].

The magnitude of the inverse Hanle signal can therefore qualitatively indicate the smoothness of the FM/barrier interface. However due to equipment limitations, an in-plane field was not possible and only the ordinary Hanle effect is investigated.

6.4.2 Electrical Measurements in Sample A and B

For sample A, 3T Hanle measurements were performed for 3 K< T <28 K in both extraction and injection modes. Throughout this temperature range a voltage drop with increase in out-of-plain magnetic field was measured and produced Hanle-like curves for both bias directions, an example of which is given in figure 6.5. The apparent spin signal was still highly visible at 28 K, however equipment faults and time limitations prevented further measurements, I expect an observable spin accumulation at higher temperatures.

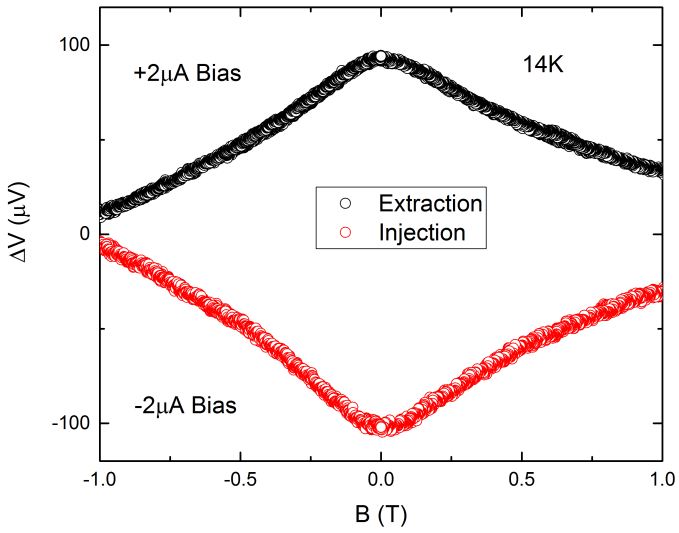

Figure 6.5: A plot of the voltage drop across the FM contact and the reference contact as a function of field for sample A. A negative (positive) bias corresponds to spin injection (extraction).

Sample B was in fact fabricated prior to sample A, however initial measurements on the device at both 300 K and 3 K revealed no noticeable spin signal when

performing Hanle type electrical measurements. After leaving the device in atmosphere, the devices were measured approximately one year later, at which point a voltage peak at zero-field was measurable. Between these two measurements, I expect that the oxygen deficient barrier may have improved in quality after gradual oxidation from the atmospheric conditions. The same issue was not present in sample A probably due to its thicker oxide layer, which will reduce leakage current through the oxide.

Sample B was of significantly lower quality, with noticeably more noise than sample A. Measurements on sample B were performed on two different devices. Preliminary measurements on the first device were relatively low noise as seen in figure 6.6, however this device was damaged after attempts to run at higher currents ($>1\,\mu A$). The majority of the measurements were then conducted on a second, lower quality device with significantly higher noise. At times the noise for this device was too significant to provide accurate fits, however measurements at the same bias current and similar temperatures agreed well for both devices when the noise was at a manageable level. Figure 6.6 gives a comparison between the two devices measured from sample B.

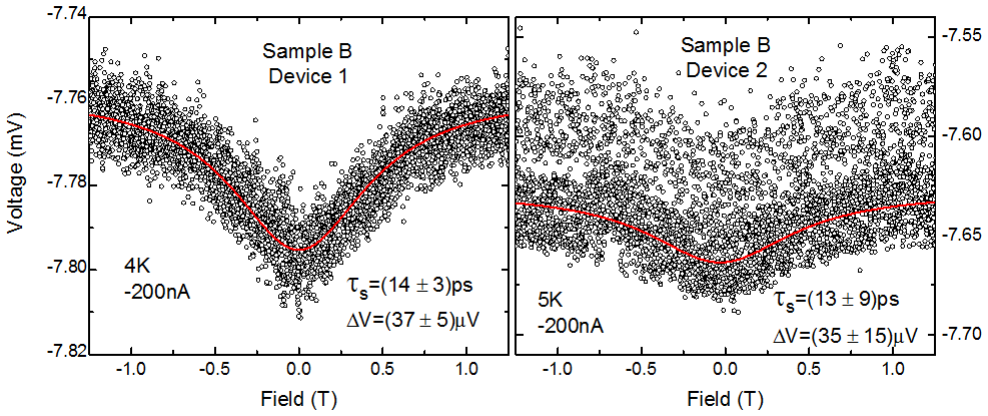

Figure 6.6: Examples of Hanle signals measured in sample B for two adjacent devices at similar temperatures and bias currents. The measured data is plotted as black circles, whilst the resulting fit is given as a red line. Device 1 (left) appears to be much higher quality with significantly lower noise than device 2 (right).

Measurements for sample B were carried out over a temperature range of 0.28 K$< T <$10 K for device 1 and 0.28 K$< T <$40 K for device 2.

Anomalous Behaviour in Sample B Spin Signals

Both devices for sample B (more so in device 2) also exhibited anomalous behaviour dependant on the sign of the bias current, this behaviour appeared to vary or even disappear upon repeat measurements with identical temperature and bias conditions. It was found for forward bias (extraction) segments of the signal curve would be shifted vertically as given in the left hand plot in figure 6.7. The fields at which the shift occurs, as well as the length of the shift, appeared to be random and change upon repeat measurements. The magnetic field was swept from zero to the maximum positive field, then down to the maximum negative field, followed by a positive sweep back to zero-field, the direction of the field sweep in figure 6.7 is denoted by the colour of the data points. The sweep of the full range in both directions along with the random nature of the shifts allows us to compare a shifted curve with a non-shifted region. The vertical shift in forward bias is likely a change in contact resistance for the FM/Ox contact. The behaviour given in figure 6.7 (left) is a more extreme example displaying 4-5 different partial Hanle signals. On this graph, it is noticeable that segments that have been shifted up in voltage follow the same trend as the lower signal, but appear to have marginally steeper gradients and therefore indicate a larger signal. This is consistent with a shift to a higher tunnel resistance (as seen in the previous chapter with the shift in tunnel I-V characteristics), indicating that some degree of charging and discharging is present in the oxide layer.

For reverse bias (injection), the signal noise was enhanced such that a second or third curve would appear above and below a stronger main curve as seen in the right plot of figure 6.7. This anomaly is noticeably different from the forward bias condition. The apparent shift does not appear in segments, but the duplication of the curve occurs through out the whole field sweep as opposed to small segments

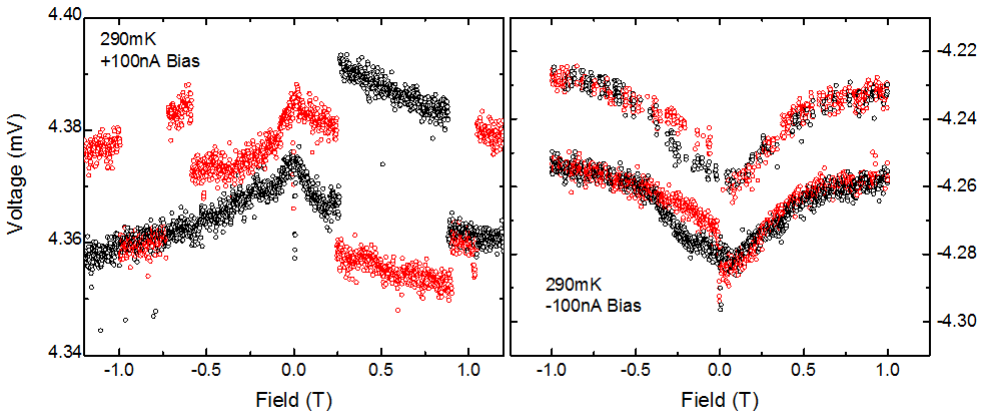

Figure 6.7: Plots of the anomalous behaviour in sample B, found when using positive (left) and negative (right) bias. Red (black) circles denote data points measured in a positive (negative) field sweep. The behaviour associated with positive bias appeared to shift segments the curve vertically, the amount of which varied and did not necessarily occur for the same region of field when reversing the sweep direction. In contrast, negative bias produced a second vertically off set curve which consisted of data points from both sweep directions.

of it. The additional curves have a weaker signal than the 'main' peak and appear as noise, but for the majority of cases strongly occur in one voltage direction with little noise between the main and secondary curves (as opposed to the case in the right hand plot of figure 6.6).

The origin of the two behaviours are likely the same, a sudden shift in tunnel characteristics, however happening at different time scales, i.e. at short and frequent intervals in reverse bias and long and slow intervals in forward bias. A reasonable explanation for this mechanism is the significant presence of charge accumulation and discharging in the tunnel barrier. The difference in frequency in the switching behaviour may be an indication of where these charge traps are located within the barrier. For spin injection, frequent switching occurs meaning short lived trapping of tunnelling charges, if this is indeed the case, the traps may be located inside the oxide, close to the Ge interface. Electrons tunnelling into the charge traps near the Ox/SC interface will have shorter trapping times as the electron will only need to tunnel a short distance through the remainder of the oxide barrier into the

semiconductor conduction band. Conversely for extraction, electrons tunnel from the semiconductor into the oxide and now will have to tunnel a larger distance to escape into the metal and thus will take a longer time to tunnel or discharge.

The inconsistent and random behaviour for forward bias made it difficult to extract meaningful fits from the curves, as a result I mostly focus on analysing Hanle signals for spin injection in sample B. The additional problem of noise along with the anomalous behaviour made it difficult to extract accurate fits and at times almost completely masked the measured Hanle peak. For this reason I will examine quantitatively the limited data collected with device 1 where noise levels and anomalous behaviour were minimal and analyse data for device 2 qualitatively.

6.4.3 Spin Lifetime

The spin lifetime, τ_s is related to the width of the Lorentzian form Hanle signal and is described by equation 3.20. Fitting this equation to the measured signals (using $g = 1.6$ for Ge [13]), I extract τ_s for the two samples over the measured temperature range and for different bias currents, an example of a curve fitted to data collected from sample A is seen in figure 6.8.

Spin Lifetime: Sample A

A plot of the measured Hanle curves at different temperatures is shown in figure 6.9 along with the extracted τ_s as a function of temperature in figure 6.10. The peak is seen to decrease in amplitude and increase in width with increasing temperature. This corresponds to a reduction of both spin accumulation and τ_s.

The extracted τ_s values range from $\sim$25 ps to $\sim$7 ps. τ_s has extensively been measured in Ge for a number of doping densities, reaching up to values of 123 ps [14][15][29][30] at room temperature. These large values however are due to lower doping densities (n$< 3 \times 10^{18}\,\mathrm{cm}^{-3}$), at higher doping levels I expect to see stronger spin relaxation from the EY mechanism, due to the increased presence of momen-

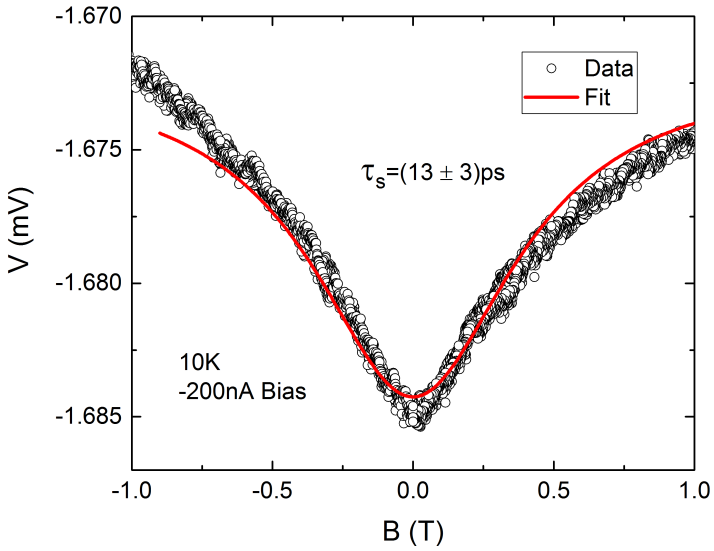

Figure 6.8: A Hanle curve measured at 10 K for sample A, with I_{Bias} =-200 nA. Data points are represented by circles and the resulting Lorentzian Hanle fit is plotted as a solid red line.

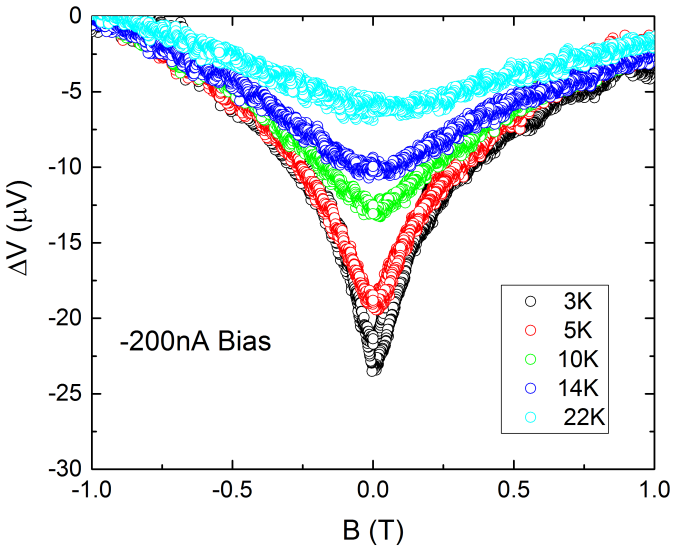

Figure 6.9: A plot of the Hanle curve measured at different temperatures for I_{Bias} =-200 nA for sample A.

tum scattering from ionised impurities, this was demonstrated by Hanbicki et al. [29] involving identical measurements with materials of different doping concentrations. Measurements on n-Ge with similar densities by Jain et al. ($1\times10^{19}\mathrm{cm}^{-3}$) [15] and Fischer et al. ($1\times10^{20}\mathrm{cm}^{-3}$) [14] have yielded τ_s values of 35 ps and 38 ps respectively at low temperatures.

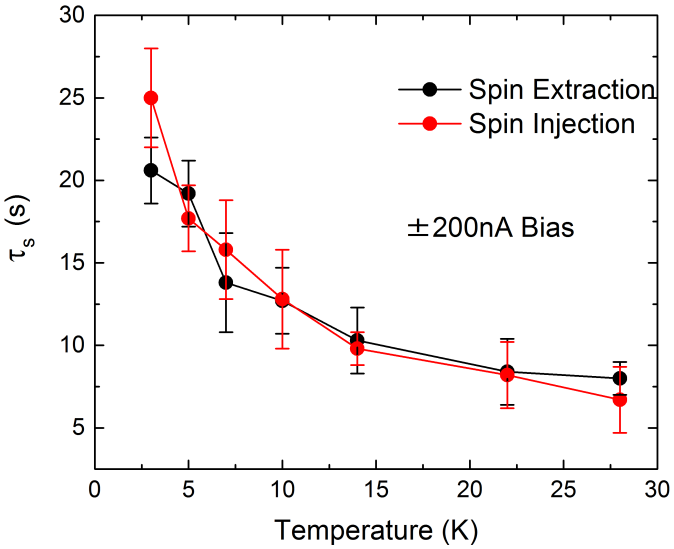

Figure 6.10: The extracted τ_s values for sample A as a function of temperature for both spin injection (red) and extraction (black).

The values extracted here are fairly similar, but still smaller, suggesting that this sample suffers from significant spin relaxation from a source other than EY. Dash et al. [28] reported a broadening of the Hanle curve and by extension an underestimation of τ_s due to local stray fields at a rough interface. Jain and Fischer who also saw these effects, stated RMS roughness of 0.2 nm and 0.4 nm at their barrier interface. The RMS roughness of sample A as stated earlier is (1.01 ± 0.01) nm, and like the device measure by Jain et al. uses NiFe/Al_2O_3, the lower value of τ_s is therefore not surprising. This however is difficult to quantify without the use of an in plane field (inverse Hanle effect). In addition to the stray magnetic fields, the

interface roughness may also increase momentum scattering in the vicinity. It can be assumed that the majority of transport takes place in the top 50 nm n^+ region due to the band bending from the doping impurities. If the carriers are confined to the surface, EY spin relaxation will be enhanced.

The temperature dependence of τ_s is highly unusual, showing a strong temperature dependence in the range measured, with τ_s beginning to level out at T >20 K. In a system in which EY spin relaxation is dominant, it is expected that $1/\tau_s \propto 1/\tau_m$ where $1/\tau_m$ is the momentum scattering rate. This results in a weak dependence at low temperatures where the majority of momentum scattering originates from charge impurities, at higher temperatures, phonon scattering becomes significant and τ_s begins to decrease with increasing temperature, this has been reported in a number of experiments [10][13]. The temperature dependence of τ_s, should therefore be reflected in the temperature dependence of the mobility. A plot of the measured μ_H as a function of temperature from Hall measurements given in figure 6.3 reveals a relatively constant momentum scattering rate for T <40 K, contradicting the behaviour of τ_s. Indeed, $1/\tau_s$ has been predicted to have a $T^{-1.66}$ dependence for phonon scattering [108], where as the temperature dependence extracted from a plot of $ln(\tau_s)$ vs. $ln(T)$ followed a $T^{-0.46}$ dependence. This suggests that either a different spin relaxation mechanism is dominant or the peak observed originates from spin accumulation not outside of the bulk Ge layer.

Using $L_s = \sqrt{D\tau_s}$, where the diffusion coefficient for a degenerate semiconductor is defined as

$$D = \frac{2}{3q}(E_F - E_C)\mu \tag{6.1a}$$

$$E_F - E_C = \frac{1}{m^*}(\frac{3}{2}\frac{\pi^2\hbar^3}{\sqrt{2}}N_D)^{2/3} \tag{6.1b}$$

a values of 67.5 nm< L_s <134.3 nm (much lower than the 4T contact separation) is calculated. Again I must remind the reader that the L_s given here is expected to be underestimated.

Spin Lifetime: Sample B

Figure 6.11, shows a plot with the smallest amount of noise and no anomalous behaviour measured in sample B device 1, which allows for the extraction of fairly accurate values of τ_s and ΔV. The resulting fit (shown as a red line) corresponds to the parameter values $\tau_s = (18 \pm 3)$ ps and $\Delta V = (38.7 \pm 5)\mu$V for spin extraction at 280 mK. Once again I have a comparable τ_s to that measured by Jain et al., although a slightly higher value than that measured in sample A is expected, due to the reduced doping concentration in this sample. A reduction of τ_s with doping density is a possible trait of DP spin relaxation which is inversely proportional to momentum scattering, though it is not expected to be the dominant in bulk. Furthermore DP dominant spin relaxation has not been reported in bulk Ge. An explanation for this behaviour is discussed later in section 6.4.4.

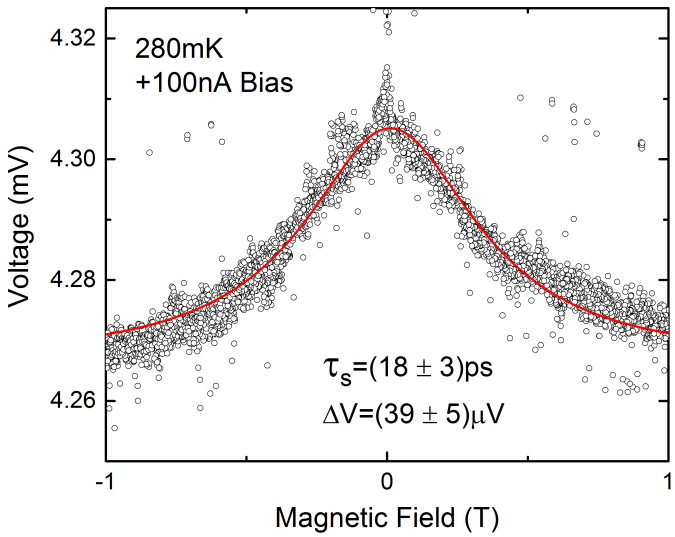

Figure 6.11: A relatively low noise plot of the apparent Hanle signal measured in sample B, device 1 at 280 mK with a bias current 100 nA.

The RMS roughness of sample A and B are comparable, furthermore the magnetisation of Ni is lower than NiFe, as a consequence it is expected that a

smaller underestimation of τ_s originating from stray fields at the interface. The barrier thickness in this sample however is thinner allowing the stray magnetostatic fields to be more effective in providing additional spin relaxation due to the proximity of the Ni to bulk Ge. The spin lifetime was extracted from curves showing minimal anomalous behaviour and noise to allow for more accurate values, τ_s vs. temperature is given in figure 6.12 for the limited temperature range device 1 was measured in. As seen in sample A, there is also an initial decrease in τ_s with temperature, with no noticeable difference between different bias currents and directions. The apparent shift from the low spin relaxation regime to the higher regime occurs at much lower temperatures below 2 K for this sample. The corresponding L_s values for this sample is 59.8 nm$< L_s <$95.3 nm within the measured temperature range of device 1.

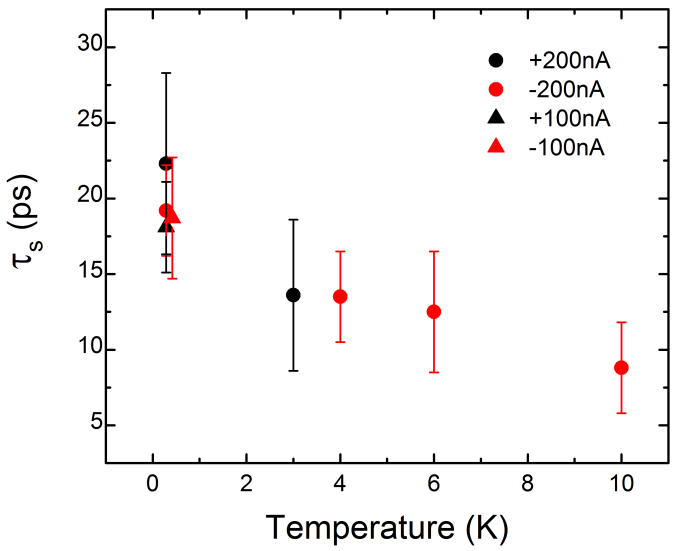

Figure 6.12: Temperature dependence of τ_s extracted from selected Hanle curves with minimal noise and anomalous behaviour in sample B, device 1 for different bias currents.

6.4.4 Spin Signal/Accumulation

An accumulation of spin results in a difference in chemical potential ($\Delta\mu_{spin} = \mu_\uparrow - \mu_\downarrow$) between the spin sub bands, this is related to the measured voltage drop due to the Hanle effect by equation 3.19. When analysing the spin signal of the electrically injected/extracted spin, it is also standard to include the voltage increase of the inverse Hanle effect to negate the reduction of the true spin signal from stray magneto static fields, $\Delta V(0)$, associated with spin accumulation is then taken to be $\Delta V(0) = \Delta V_{Hanle}(0) + \Delta V_{InverseHanle}(0)$. Due to the limitations of the equipment, only regular Hanle measurements were taken and thus the inverse Hanle signal is not included in the analysis.

Although ΔV directly described the degree of spin accumulation, the spin resistance-area product, $R_sA = \Delta V(0)/J$ is also commonly use to look at the efficiency of spin injection and allows direct comparison with other devices regardless of the differences between bias used and contact dimensions.

Spin Signal: Sample A

I first examine the temperature dependence of the spin signal in sample A. The R_sA product was calculated such that both the area of the contact pad and contact arm for the injector/detector contact was taken into account. As stated before, the primary design for this device was intended for a 4T set up where only a weak signal from the diffused spins under the detector contact in the mesa bar is measured. There should be no significant diffusion of spins from the mesa bar to the large contact pad, hence the active area for the 4T orientation is the area of the contact arms overlapping with the mesa bar. However as a 3T set up is used here, the detector and injector contacts are one and the same and spins injected under the contact pas is also detected. The area used in signal calculations changes from $A = 200\,\mu\text{m}^2$ to $A = 40200\,\mu\text{m}^2$ when using the device in a 3T-Hanle orientation.

The spin accumulation under the detection contact will be a balance between

the rate of spins injected into the material, the rate at which the spins relax and the rate at which spins diffuse away from the contact area. $\Delta V(0)$ will thus change with bias and TSP (γ), if γ is constant with bias current/voltage then R_sA should not change with bias.

A plot of R_sA against temperature is given for both extraction and injection regimes in figure 6.13 and is seen to drop with temperature as a response to the drop in τ_s. The slight offset between the two regimes is a result of the asymmetry of tunnelling through the residual Schottky barrier at the Al_2O_3/Ge interface, though larger differences between the bias sign are commonly observed [10][29]. When spin is injected, E_F in the FM is raised above E_F in the semiconductor to allow electrons to flow into the semiconductor conduction band, in extraction E_F in the FM is lowered. It follows that in injection, the electrons that tunnel are those at E_F, with extraction, the electrons tunnel through into the FM into energies above E_F, where the polarisation (spin density of states) is different. In addition to this, the bias also changes the depletion width of the Schottky barrier, which in turn changes the tunnelling transparency. The small degree of asymmetry here is due to the thinning of the Schottky barrier from the high level of doping. This effect is enhanced as dopants typically segregate towards the surface to produce a higher level of doping in the first few nm below the surface (which was visible in SIMS scans of the material used). Fully symmetrical behaviour in p-Ge has been observed in Fe/GeO_2 devices on Ge [109].

Understandably, increasing the bias current results in a larger $\Delta V(0)$, as the number of majority spins injected/extracted is increased, however plotting R_sA against bias current actually reveals a a slight decrease in spin accumulation, if any at all (figure 6.14). τ_s remained constant with respect to the bias, meaning that the reduction in spin accumulation is related to a loss of TSP efficiency with bias current (voltage) which has also been reported by Dash et al. [9].

I now compare the measured R_sA with the expected values estimated with

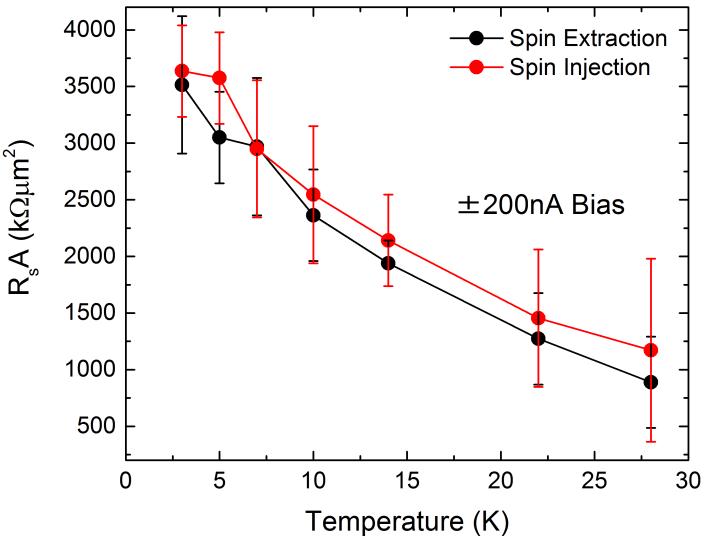

Figure 6.13: A plot of the R_sA product as a function of temperature for spin injection (red) and extraction (black) in sample A.

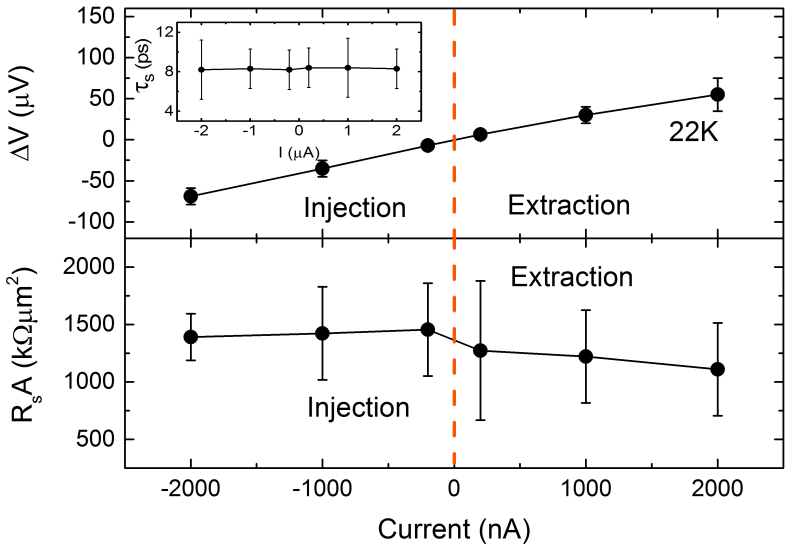

Figure 6.14: Plots of $\Delta V(0)$ (top) and R_sA (bottom) for sample A, with different bias currents at 22 K, the inset shows a constant τ_s for all bias currents.

spin diffusion theory. For this I consider two scenarios, firstly I look at the possibility of spin accumulation and diffusion across the full heterostructure. In the condition where the contact dimensions $W_x, W_y \gg L_s$ and the channel thickness $t \gg L_s$, the spin accumulation is predicted to be [16]

$$R_s A = \gamma^2 \rho L_s \tag{6.2}$$

Instead of using the calculated values, L_s (for which I expect to be underestimated) is taken to to be 1 µm as Jain et al. does in reference [15], this value should still be small enough such that a non-local signal will not be observable in these devices. I work out the expected $R_s A$ for the device with bias current -200 nA for which $\rho = (38.700 \pm 0.006)\,\mathrm{m\Omega cm}$ (calculated from the measured sheet resistance) and γ is taken to be 0.3 for NiFe/Al_2O_3 (measured by Dash et al. [9]). As the measurement uses a local 3T orientation, the area under the whole contact must be considered, including the area beneath the contact pad, bringing the total contact area to $A = 40.2\times10^3\,\mu\mathrm{m}^2$, the predicted $R_s A$ comes to $3.5\times10^{-2}\,\mathrm{k\Omega\mu m^2}$, five orders of magnitude smaller than what was measured (as seen in figure 6.13), despite the generous value of L_s used. Furthermore the measured signal is also expected to be higher (by 2-3 times) as the full signal must also include the voltage increase from the inverse Hanle effect to exclude effects from the stray magnetostatic fields.

The case where transport only takes place in the n^+ layer is also considered. The band offset between the n-Ge and the undoped bulk may be large enough to produce a potential well in which injected carriers are confined, using equation 6.1b the offset between the two layers is ∼31 meV. In this scenario $t \ll L_s$ and therefore the following equation is used [16]

$$R_s A = \gamma^2 \rho L_s^2 / t \tag{6.3}$$

The resulting expected value is R_sA =2.8×10^{-2} kΩμm^2, still five orders of magnitudes different than measured. The enhancement of spin signal, has been widely reported in similar devices, typically on the order of two-three orders of magnitudes in semiconductors [15][100] and has been measured as high as seven orders in magnitude in Si [110] and eight orders of magnitude in metallic Al [111]. It has also been noted that the enhancement of spin signal is particularly prominent at both low biases and temperatures [15], which is true for the conditions I present here. The source of this anomalously high spin signal later in section 6.4.4.

Spin Signal: Sample B

The RA_s for a bias of -200 nA in the temperature range measured for device 1 is plotted in figure 6.15. There is an initial drop in spin signal with an increase in temperature, however unlike sample A, it appears to level off quickly for T >2 K with values around 7500 kΩμm^2. Once again, this drop in signal stems from the drop and stabilisation of τ_s in sample B which also levels off fairly quickly.

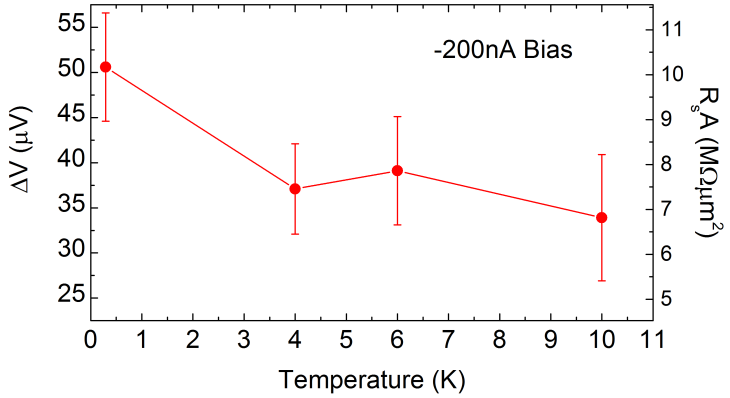

Figure 6.15: Temperature dependence of R_sA extracted from selected Hanle curves with minimal noise and anomalous behaviour in sample B, device 1 at -200 nA bias current.

As mentioned previously, device 2 displayed evidence of spin signals observable for temperatures exceeding the range for which device 1 was measured. Plots

of the Hanle signal at -200 nA bias at different temperatures are given in figure 6.16. A noticeable drop in peak amplitude is observed between 2 K and 5 K, above 5 K the drop in signal stabilises, following the trend as seen in device 1. At temperatures $\geq$25 K no signal associated with spin accumulation is visible suggesting that the tunnelling spin polarization is reduced to zero. The anomalous behaviour in which the signal is duplicated and offset in negative bias is also not visible at these higher temperatures implying that the behaviour is closely related to the spin tunnelling process.

The effect of (negative) bias current on the apparent spin signal measured in sample B device 2 is analysed qualitatively. Plots of the measured spin signal for device 1 at 3 K for different bias currents are given in figure 6.17. The peak amplitude appears to increase initially with bias current, along with the level of noise. As the magnitude of the bias is increased to I_{Bias} <-300 nA, the noise level increases significantly, however a weak peak-like structure is visible, although with a smaller amplitude. At I_{Bias} =-400 nA there is almost no indication of spin accumulation apart from the noise-like anomalous behaviour. Unexpectedly higher bias magnitudes produces a signal peak of opposite sign. This behaviour is not attributed to the Hanle effect as it implies an increase in spin accumulation with out-of-plane field strength and is likely associated with an MR effect.

Using L_s =1μm as done for sample A and γ =0.11 for Ni [112], the predicted R_sA for in this temperature range is 9.2×10^{-3} kΩμm^2 when considering transport confined to the n$^+$ region and 11.5×10^{-3} kΩμm^2, when taking into account the i-Ge region, both values are much smaller than what was measured. The spin accumulation in sample B is surprisingly larger than in sample A despite the use of Ni with a lower γ, it is difficult to comment on why this is the case, as both samples experience an enhancement in signals.

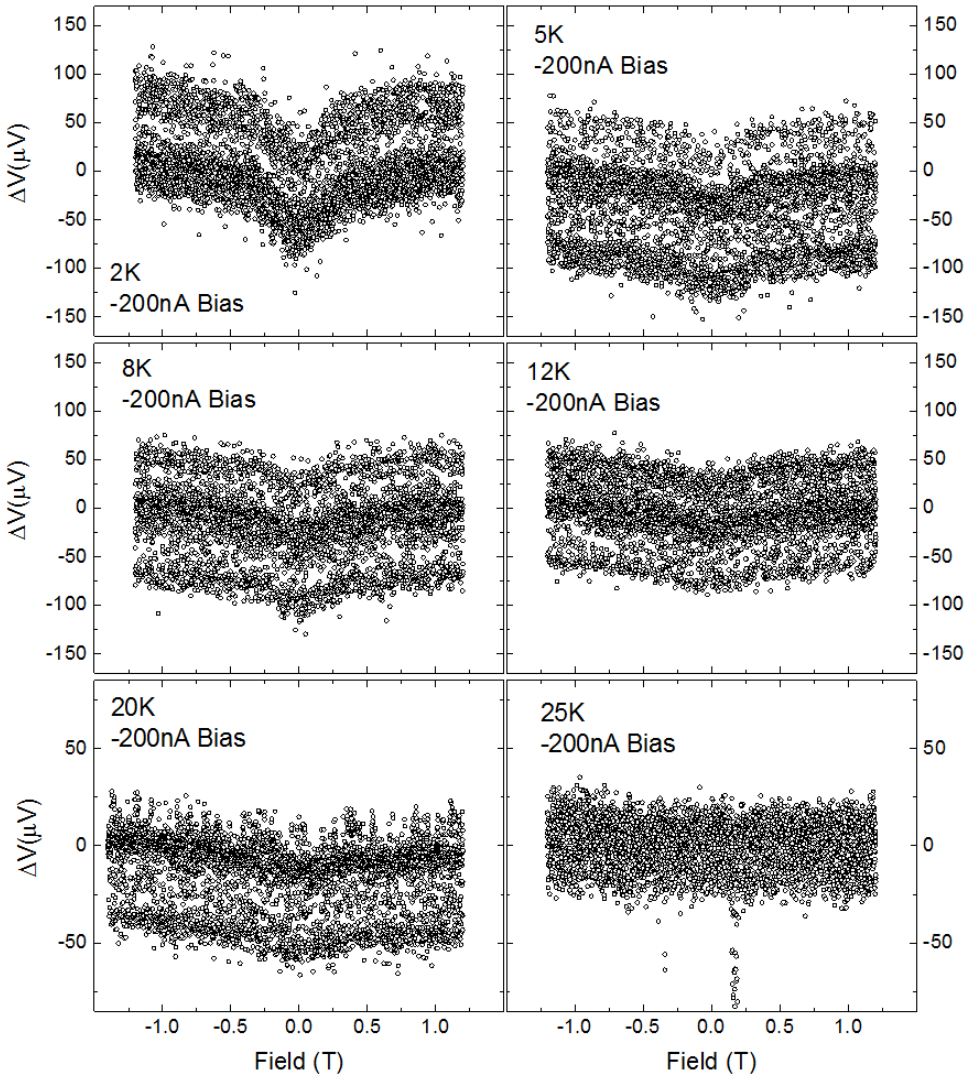

Figure 6.16: Plots of sample B device 2 Hanle curves, measured at a range of temperatures for bias current -200 nA. As temperature is increased, the Lorentzian curve amplitude decreases corresponding to a decrease in spin accumulation, for temperatures above 20 K no visible spin signal is observed.

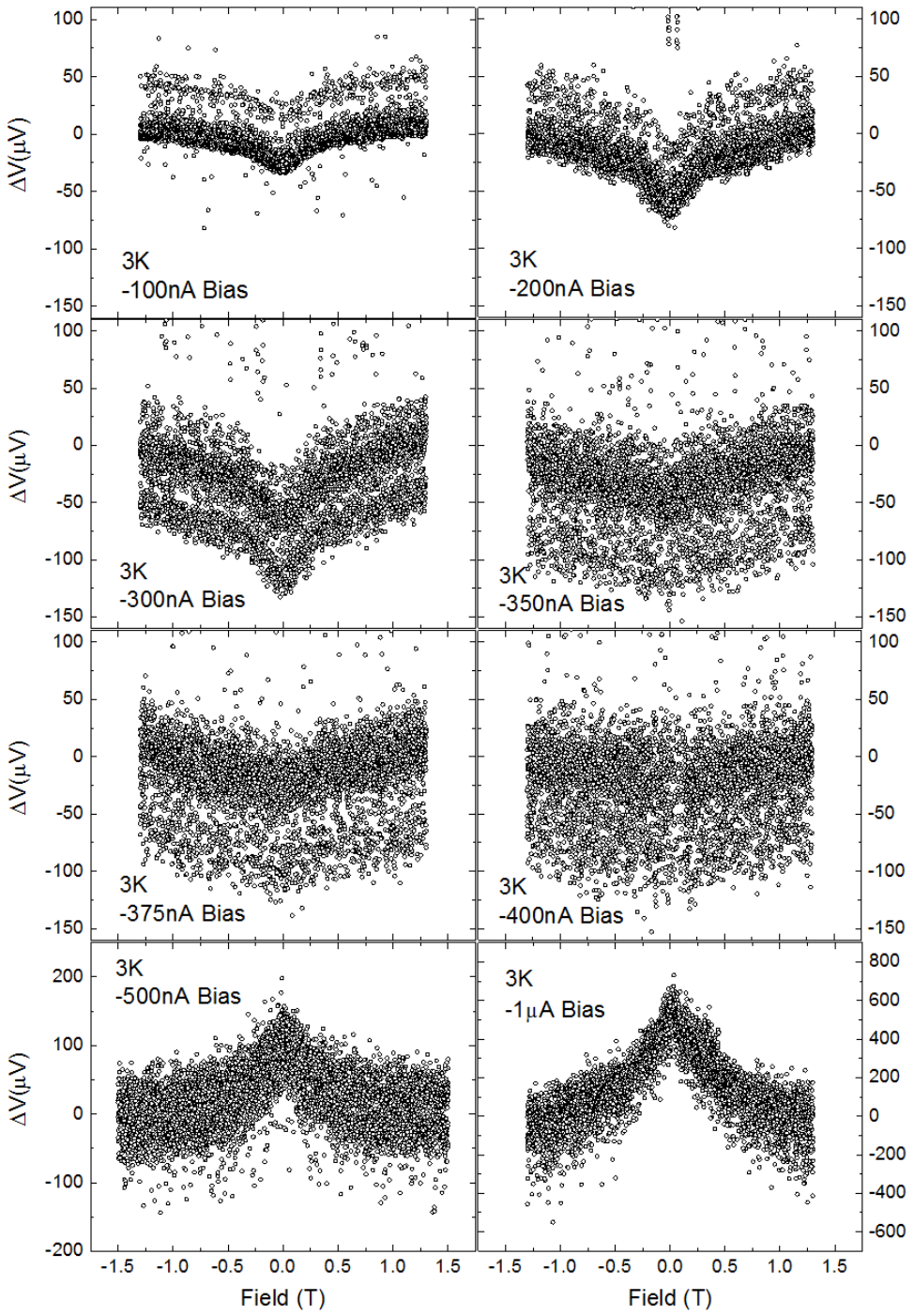

Figure 6.17: Plots of sample B device 2 Hanle curves, measured at 3 K for different bias currents. The spin signal increases with bias current, above this, the noise become worse and the signal begins to drop until no noticeable signal can be observed at -400 nA bias. Above this limit, a positive MR is measured.

Origin of Anomalous Spin Signal Enhancement

Both samples displayed much larger values R_sA than is predicted by current theory, producing an enhancement of 5-6 orders of magnitude. The origin of the anomalous spin signal enhancement has been extensively investigated and debated on [9][16][17][100][113], however there is currently no consensus on the matter. Several explanations have been put across. Dash first suggested that a non-uniform tunnel barrier will cause an incorrect calculation of the expected signal if spin tunnelling was concentrated at different points in the tunnel contact, therefore reducing the real value of J. Although this may cause some discrepancy [9], particularly in the tunnel barriers used here, which are known to have current leakage issues (as discussed in section 5.2.3), it was dismissed as the effective contact areas were required to be unrealistically small. Indeed with the contacts used here an effective contact area of $0.4\,\mu m^2$ is required to explain the observed signal.

Another popular theory is the enhancement of the spin signal via localised states in the barrier, in which electrons can tunnel into from the FM, before tunnelling again into the semiconductor bulk. The occupation of these states by these spin polarised carriers will therefore also be measured as part of the spin accumulation signal in the bulk semiconductor. In addition to this, the measured spin lifetime will also be a weighted average of the lifetime of the local states and the semiconductor. The strong temperature dependence of the τ_s may relate to a shift in dominance between the two tunnelling modes. The idea of localised states was first proposed by Tran et al [17] with a basic model of purely two-step tunnelling and refined by Jansen et al [16] to include spin accumulation detection with direct and two-step tunnelling in parallel.

The localised states can either occur at the Ox/SC interface or within the barrier itself via the same mechanisms as charge trapping. From the previous chapter and the anomalous behaviour seen in sample B device 2 the contacts fabricated here will likely contain a significant density of localised states. Sample 2 is notice-

ably noisier than sample A owing to a lower quality barrier and therefore a larger density of localised states, this may explain why the enhancement in sample B is noticeably larger. Further measurements are required to confirm the presence and effects of these local states. Spin accumulation due to interface states may be probed by measuring similar devices with a treated (passivated) Ge surface. To investigate local states within the barrier, a comparison will need to be made with a similar device with a plasma treated barrier.

One final explanation for signal enhancement is unique to this particular design. These measurements and calculations are based on the idea that the accumulated spins under the contact are free to diffuse deeper into the bulk as well as laterally. The majority of the spins injected will be located under the large contact pad, due to the design of the device the mesa ends at the edge of the contact, restricting lateral diffusion. Although this will increase accumulation directly under the contact, the effect is believed to be marginal.

6.5 Summary

Devices for Hanle measurements on Ge were fabricated using UV-lithography and e-beam deposition for contact fabrication. Two structures were investigated: NiFe/Al_2O_3 on n-Ge ($1.4 \times 10^{19}\,cm^{-3}$) and Ni/$Al_2O_3$ on n-Ge ($5 \times 10^{18}\,cm^{-3}$). Although the device design was capable of non-local 4T Hanle measurements, no signal was observed outside of the local 3T measurement. The NiFe/Al_2O_3 device produced a spin-like signal up to 28 K (for the full range of temperatures measured) where as the Ni/Al_2O_3 sample spin signal survived up to 20 K.

The latter device displayed anomalous behaviour, highly dependent on bias direction, the effect of which shifted the Hanle curve in a vertical direction corresponding to a change in tunnel contact resistance. It is thought that the cause of this contact resistance change is from the charging and discharging of the dielectric

of which was investigated in section 5.2.3.

The extracted τ_s values were of the range 7 ps$< \tau_s <$25 ps, slightly smaller than that seen in other highly doped n-Ge [14][15]. This is attributed to the Ge surface with a RMS roughness at least a factor of 2 larger, resulting in additional spin relaxation from stray local magnetostatic fields at the Ge barrier interface. τ_s was also found to have a strong temperature dependence in the measured range, contradictory to what is expected for EY spin relaxation. Current theory and relaxation mechanisms do not provide an alternate explanation for this.

Calculation of the expected R_sA product for both samples/devices found the extracted values to be 5-6 orders of magnitude larger than predicted. It is thought that this enhancement of the spin signal stems mostly from the inclusion of localised states either at the Ox/SC interface or within the oxide, which allow for an accumulation of spin to occur and be detected within the barrier. Fabrication and measurements of control devices are required to confirm this.

It is clear from the poor performance of these devices that the standard deposition technique e-beam evaporation is inadequate to form suitable tunnel contacts for spin injection/extraction without further steps and treatments to ensure barrier quality and high temperature operation.

Chapter 7

Summary

This thesis explores the suitability of Ge and Ge/$Si_{1-x}Ge_x$ heterostructures for applications in spintronics, namely for the achievable high mobilities and tuneable SOI. It also looks at the suitability of depositing spin tunnel contacts onto Ge with the use of standard deposition techniques already widely used in industry as opposed to the research specific tools such as MBE.

The first investigation examines the Rashba SOI in a high mobility, modulated doped, strained Ge 2DHG. Low temperature MR and Hall measurements extracted a Hall mobility of 777,000 $cm^2V^{-1}s^{-1}$ for temperatures below 45 K. The high level of dopants in the modulation layer was found to be electrically active at the lowest of temperatures, forming a parallel conduction channel. Below 1.9 K at low fields, a negative MR associated with WL was observed, before this gave way to WAL for higher temperatures. The apparent, unorthodox shift from WL to WAL was attributed to the summation of quantum effects from the two conducting channels, specifically WL from the low mobility doping channel and WAL from the pure Ge channel.

The combined behaviour of the two parallel channels meant a fitting of the low field MR was not possible. Instead the strength of the Rashba SOI was estimated from the field at which WL dominates the MR, giving a spin slit energy $\Delta_0 =$

0.8 meV. This value agrees well with other electrically extracted values for Ge 2DHG, furthermore the cubic Rashba coefficient was found to be $B_R = 3.2 \times 10^{-28}\,\mathrm{eVm}^3$, larger than other group IV or group III-V 2DHGs. We conclude that the strength of the SOI in this sample is from the asymmetrical electric field across the QW from the high level of doping impurities.

In chapter 5, I studied the feasibility of employing standard evaporation and sputtering techniques for low cost deposition of magnetic tunnel junctions on Ge. XPS and TEM measurements probed the interface of the deposited materials on Ge to study the robustness of oxide barriers and the evolution of contact material during annealing required to treat and improve tunnel characteristics. Al_2O_3 proved to be more robust than MgO, where a 1 nm thick barrier survived annealing temperatures up to 350°C when using Ni as a capping layer and 475°C when using NiFe. MgO on the other hand failed at T <300°C for Ni/MgO stacks and required a minimum thickness of 3 nm to survive at 375°C and only showed partial crystallinity post anneal.

The study continued with the electrical characterisation of as deposited Ni/Al_2O_3, $NiFe/Al_2O_3$ and Ni/NgO type contacts for different oxide thicknesses. TLM structures and I-V measurements failed to produce the exponential increase in resistance with oxide thickness, suggesting significant amounts of leakage though the oxide. It was found that a number of devices were plagued by unstable dielectrics resulting in shifting junction resistances between and during voltage/current sweeps due to frequent charging and discharging of the dielectric.

The final chapter described the fabrication and measurement of Hanle devices on bulk n-Ge with tunnel contact material Ni/Al_2O_3 and $NiFe/Al_2O_3$. Hanle spin signals were observed for both sample types at low temperatures below 28 K, however the $NiFe/Al_2O_3$ based device appeared to suffer high levels of noise and anomalous behaviour believed to be associated with the charging and discharging of the dielectric as seen in chapter 5. The extracted τ_s was of the order 7-25 ps,

close to other reported low temperature values for degenerately doped n-Ge. Both devices exhibited a large enhancement of the spin accumulation signal of up to seven orders of magnitude from the predicted value. Although it is difficult to confirm, the clear presence of charge traps inferred from the dielectric discharge behaviour of the NiFe/Al_2O_3 and similar contacts in the chapter 5 study doubles up as traps for spins. The accumulation of spins in these traps contribute to the total signal detected.

In conclusion, the poor performance of the fabricated tunnel contacts leads us to believe that for the implementation of spin injection contacts into real world applications will either prove to be difficult or non-affordable, when employing more reliable, but slow techniques such as MBE and ALD. Despite this, Ge remains an exciting candidate for quality semiconductor spintronics, specifically due to its high mobility and its tuneable, strong Rashba coefficient, that is not hindered by the presence of the Dresselhaus SOI.

Chapter 8

Future Work

The work described in chapter 4 is one of only a few studies that has electrically measured the Rashba SOI in a 2D Ge system. A more in-depth study of the Rashba SOI is required, namely involving the effect of an applied external field via gating on the strength of the Rashba SOI. However these experiments have been marred by the added effect of changing carrier densities which Δ_0 is also dependent on [47][48]. To move on from this problem, similar experiments must be conducted with the addition of a second gate such that the heterostructure is both top and bottom gated [93][94]. Simultaneous application of gate voltages can be used to adjust the internal electric field whilst keeping carrier concentrations constant.

We attribute our strong SOI from the high level of doping in our supply layer, it would thus be interesting to study the effect of doping density and in addition spacer layer thickness on the strength of the Rashba SOI, though this may be difficult as the spacer thickness will also affect the carrier concentration in the well. Through calibration of these two factors it will also be possible to obtain a high mobility Ge 2DHG with high mobility and no parasitic conduction which will complicate the analysis of the Rashba SOI in this system.

Ultimately it was the initial goal to inject spin electrically directly into a Ge QW and measure the spin lifetime of non-equilibrium spins in a 2D system. As it

stands, the heterostructures investigated over the duration of this project used a modulated doping supply layer above the Ge channel along with a series of spacers and $Si_{1-x}Ge_x$ and Si capping layers. This type of structure is unsuitable for electrical injection due to the potential well created by the doping profile and the distance required for the carriers to reach the QW (a minimum 50 nm of spacer, capping and supply layers). It is therefore necessary to develop inverted modulated doped QW structures and bring the Ge channel as close as possible to the surface.

Bibliography

[1] V. K. Joshi. Spintronics: A contemporary review of emerging electronics devices. *Engineering Science and Technology, an International Journal*, 19(3):15031513, 2016.

[2] M. N. Baibich, J. M. Broto, A. Fert, F. Nguyen Van Dau, F. Petroff, P. Etienne, G. Creuzet, A. Friederich, and J. Chazelas. Giant magnetoresistance of (001)Fe/(001)Cr magnetic superlattices. *Physical Review Letters*, 61(21):2472, 1988.

[3] G. Binasch, P. Grnberg, F. Saurenbach, and W. Zinn. Enhanced magnetoresistance in layered magnetic structures with antiferromagnetic interlayer exchange. *Physical Review B*, 39(7):4828, 1989.

[4] S. S. P. Parkin. Dramatic enhancement of interlayer exchange coupling and giant magnetoresistance in $Ni_{81}Fe_{19}$/Cu multilayers by addition of thin Co interface layers. *Applied Physics Letters*, 61:1358, 1992.

[5] J. A. C. Bland and B. Heinrich. *Ultrathin Magnetic Structures II - An Introduction to the Electronic, Magnetic and Structural Properties — J.A.C. Bland — Springer*, volume 2. Springer, 1994.

[6] T. Yamamoto, H. Kano, Y. Higo, K. Ohba, T. Mizuguchi, M. Hosomi, K. Bessho, M. Hashimoto, H. Ohmori, T. Sone, K. Endo, S. Kubo, H. Narisawa, W. Otsuka, N. Okazaki, M. Motoyoshi, H. Nagao, and T. Sagara. Mag-

netoresistive random access memory operation error by thermally activated reversal. *Journal of Applied Physics*, 97:10P503, 2005.

[7] D. T. Pierce and F. Meier. Photoemission of spin-polarized electrons from GaAs. *Physical Review B*, 13(12):5484, 1976.

[8] E. Saitoh, M. Ueda, H. Miyajima, and G. Tatara. Conversion of spin current into charge current at room temperature: Inverse spin-hall effect. *Applied Physics Letters*, 88:182509, 2006.

[9] S. P. Dash, S. Sharma, R. S. Patel, M.l P. de Jong, and R. Jansen. Electrical creation of spin polarization in silicon at room temperature. *Nature*, 462(7272):491–494, 2009.

[10] Y. Zhou, W. Han, L. T. Chang, F. Xiu, M. Wang, M. Oehme, I. A. Fischer, R. K. Kawakami, and K. L. Wang. Electrical spin injection and transport in germanium. *Physical Review B*, 84(12):125323, 2011.

[11] S. G. Bhat and P. S. Anil Kumar. Room temperature electrical spin injection into GaAs by an oxide spin injector. *Nature Scientific Reports*, 4:05588, 2014.

[12] F. Pezzoli, F. Bottegoni, D. Trivedi, F. Ciccacci, A. Giorgioni, P. Li, S. Cecchi, E. Grilli, Y. Song, M. Guzzi, H. Dery, and G. Isella. Optical spin injection and spin lifetime in Ge heterostructures. *Physical Review Letters*, 108(15):156603, 2012.

[13] L. T. Chang, W. Han, Y. Zhou, J. Tang, I. A. Fischer, M. Oehme, J. Schulze, R. K. Kawakami, and K. L. Wang. Comparison of spin lifetimes in n-Ge characterized between three-terminal and four-terminal nonlocal hanle measurements. *Semiconductor Science and Technology*, 28(1):015018, 2013.

[14] I. A. Fischer, L. T. Chang, C. Srgers, E. Rolseth, S. Reiter, S. Stefanov, S. Chiussi, J. Tang, K. L. Wang, and J. Schulze. Hanle-effect measurements

of spin injection from $Mn_5Ge_3C_{0.8}/Al_2O_3$ contacts into degenerately doped Ge channels on Si. *Applied Physics Letters*, 105(22):222408, 2014.

[15] A. Jain, L. Louahadj, J. Peiro, J. C. Le Breton, C. Vergnaud, A. Barski, C. Beign, L. Notin, A. Marty, V. Baltz, S. Auffret, E. Augendre, H. Jaffrs, J. M. George, and M. Jamet. Electrical spin injection and detection at Al_2O_3/n-type germanium interface using three terminal geometry. *Applied Physics Letters*, 99(16):162102, 2011.

[16] R. Jansen, S. P. Dash, S. Sharma, and B. C. Min. Silicon spintronics with ferromagnetic tunnel devices. *Semiconductor Science and Technology*, 27(8):083001, 2012.

[17] M. Tran, H. Jaffrs, C. Deranlot, J.-M. George, A. Fert, A. Miard, and A. Lematre. Enhancement of the spin accumulation at the interface between a spin-polarized tunnel junction and a semiconductor. *Physical Review Letters*, 102(3):036601, 2009.

[18] K. Kashara, Y. Baba, K. Yamane, Y. Ando, S. Yamada, Y. Hoshi, K. Sawano, M. Miyao, and K. Hamaya. Spin accumulation created electrically in an n-type germanium channel using Schottky tunnel contacts. *Journal of Applied Physics*, 111:07C503, 2012.

[19] A. Dankert, R. S. Dulal, and S. P. Dash. Efficient spin injection into silicon and the role of the schottky barrier. *Nature Scientific Reports*, 3:03196, 2013.

[20] M. C. Hickey, S. N. Holmes, T. Meng, I. Farrer, G. A. C. Jones, D. A. Ritchie, and M. Pepper. Strongly bias-dependent spin injection from Fe into into n-type GaAs. *Physical Review B*, 75(19):193204, 2007.

[21] J. E. Hirsch. Spin hall effect. *Physical Review Letters*, 83(9):1834, 1999.

[22] Y. K. Kato, R. C. Myers, A. C. Gossard, and D. D. Awschalom. Observation of the spin hall effect in semiconductors. *Science*, 306:1910–1913, 2004.

[23] G. Schmidt, D. Ferrand, L. W. Molenkamp, A. T. Filip, and B. J. van Wees. Fundamental obstacle for electrical spin injection from a ferromagnetic metal into a diffusive semiconductor. *Physical Review B*, 62(8):R4790, 2000.

[24] G. Schmidt and L. W. Molenkamp. Spin injection into semiconductors, physics and experiments. *Semiconductor Science and Technology*, 17(4):304, 2002.

[25] H. Ohno. A window on the future of spintronics. *Nature Materials*, 9:952, 2010.

[26] A. Fert and H. Jaffrs. Conditions for efficient spin injection from a ferromagnetic metal into a semiconductor. *Physical Review B*, 64(18):184420, 2001.

[27] E. I. Rashba. Theory of electrical spin injection: Tunnel contacts as a solution of the conductivity mismatch problem. *Physical Review B*, 62(24):R16267, 2000.

[28] S. P. Dash, S. Sharma, J. C. Le Breton, J. Peiro, H. Jaffrs, J.-M. George, A. Lematre, and R. Jansen. Spin precession and inverted hanle effect in a semiconductor near a finite-roughness ferromagnetic interface. *Physical Review B*, 84(5):054410, 2011.

[29] A. T. Hanbicki, S. F. Cheng, R. Goswami, O. M. J. van 't Erve, and B. T. Jonker. Electrical injection and detection of spin accumulation in Ge at room temperature. *Solid State Communications*, 152(4):244–248, 2012.

[30] K. R. Jeon, B.-C. Min, Y.-H. Jo, H.-S. Lee, I.-J. Shin, C.-Y. Park, S.-Y. Park, and S.-C. Shin. Electrical spin injection and accumulation in CoFe/MgO/Ge contacts at room temperature. *Physical Review B*, 84(16):165315, 2011.

[31] Y. A. Bychkov and E. I. Rashba. Oscillatory effects and the magnetic susceptibility of carriers in inversion layers. *Solid State Physics*, 17(33):6039, 1984.

[32] S. Datta and B. Das. Electronic analog of the electro-optic modulator. *Applied Physics Letters*, 56(7):665–667, 1990.

[33] P. Barate, S. Liang, T. Zhang, J. Frougier, M. Vidal, P. Renucci, X. Devaux, B. Xu, H. Jaffrs, J. M. George, X. Marie, M. Hehn, S. Mangin, Y. Zheng, T. Amand, B. Tao, X. F. Han, Z. Wang, and Y. Lu. Electrical spin injection into InGaAs/GaAs quantum wells: A comparison between MgO tunnel barriers grown by sputtering and molecular beam epitaxy methods. *Applied Physics Letters*, 105:012404, 2014.

[34] G. Dresselhaus. Spin-orbit coupling effects in zinc blende structures. *Physical Review*, 100(2):580, 1955.

[35] A. Dobbie, M. Myronov, R. J. H. Morris, A. H. A. Hassan, M. J. Prest, V. A. Shah, E. H. C. Parker, T. E. Whall, and D. R. Leadley. Ultra-high hole mobility exceeding one million in a strained germanium quantum well. *Applied Physics Letters*, 101(17):172108, 2012.

[36] M. Myronov, C. Morrison, J. Halpin, S. D. Rhead, C. Casteleiro, J. Foronda, V. A. Shah, and D. Leadley. An extremely high room temperature mobility of two-dimensional holes in a strained Ge quantum well heterostructure grown by reduced pressure chemical vapor deposition. *Japanese Journal of Applied Physics*, 53(4S):04EH02, 2014.

[37] M. E Levinshtein, S. L. Rumyantsev, and M. S. Shur. *Properties of Advanced Semiconductor Materials: GaN, AIN, InN, BN, SiC, SiGe.* Wiley-Interscience, 2001.

[38] E. Kasper, A. Schuh, G. Bauer, B. Hollnder, and H. Kibbel. Test of Vegard's law in thin epitaxial SiGe layers. *Journal of Crystal Growth*, 157:68, 1995.

[39] D. De Salvador, M. Petrovich, M. Berti, F. Romanato, E. Napolitani, A. Drigo, J. Stangl, S. Zerlauth, M. Muhlberger, F. Schaffler, G. Bauer, and P. C. Kelires. Lattice parameter of $Si_{1-x-y}Ge_xC_y$ alloys. *Physical Review B*, 61:13005–13013, 2000.

[40] J. Weber and M. I. Alonso. Near-band-gap photoluminescence of Si-Ge alloys. *Physical Review B*, 40(8):5683, 1989.

[41] A. Sadao. *Properties of group-IV, III-V and II-VI semiconductors / Sadao Adachi.* Wiley series in materials for electronic and optoelectronic applications. John Wiley & Sons, 2005.

[42] Vishal Shah. *Reverse Graded High Content (x>0.75) $Si_{1-x}Ge_x$ Virtual Substrates.* Thesis, 2009.

[43] M. Myronov. *Magnetotransport, structural and optical characterisation of p-type modulation doped heterostructures with high Ge content $Si_{1-x}Ge_x$ channel grown by SS-MBE on $Si_{1-y}Ge_y$/Si(001) virtual substrates.* Thesis, 2001.

[44] A. A. Williams, J. M. C. Thornton, J. E. Macdonald, R. G. van Silfhout, J. F. van der Veen, M. S. Finney, A. D. Johnson, and C. Norris. Strain relaxation during the initial stages of growth in Ge/Si(001). *Physical Review B*, 43:5001, 1991.

[45] A. Manchon, H. C. Koo, J. Nitta, S. M. Frolov, and R. A. Duine. New perspectives for rashba spin-orbit coupling. *Nature Materials*, 14:871–882, 2015.

[46] J. Nitta, T. Akazaki, H. Takayanagi, and T. Enoki. Gate control of spin-

orbit interaction in an inverted $In_{0.53}Ga_{0.47}As/In_{0.52}Al_{0.48}As$ heterostructure. *Physical Review Letters*, 78(7):1335, 1997.

[47] V. A. Guzenko, M. Akabori, T. Schpers, S. Cabaas, T. Sato, T. Suzuki, and S. Yamada. Weak antilocalization measurements on a 2-dimensional electron gas in an InGaSb/InAlSb heterostructure. *physica status solidi (c)*, 3(12):4227–4230, 2006.

[48] R. Moriya, K. Sawano, Y. Hoshi, S. Masubuchi, Y. Shiraki, A. Wild, C. Neumann, G. Abstreiter, D. Bougeard, T. Koga, and T. Machida. Cubic Rashba spin-orbit interaction of a two-dimensional hole gas in a strained-Ge/SiGe quantum well. *Physical Review Letters*, 113(8):086601, 2014.

[49] R. Winkler. *Spin–Orbit Coupling Effects in Two-Dimensional Electron and Hole Systems - Springer*, volume 191 of *Springer Tracts in Modern Physics*. Springer, 2003.

[50] M. I. Dyakonov. *Spin Physics in Semiconductors*, volume 157 of *Springer Series in Solid-State Sciences*. 2008.

[51] K. Kondo. Spin filter effects in an Aharonov-Bohm ring with double quantum dots under general Rashba spin-orbit interactions. *New Journal of Physics*, 18:013002, 2016.

[52] O. Mauritz and U. Ekenberg. Spin splitting in a p-type quantum well with built-in electric field and microscopic inversion asymmetry. *Physical Review B*, 55(16):10729, 1997.

[53] R. Winkler, H. Noh, and M. Shayegan. Anomalous Rashba spin splitting in two-dimensional hole systems. *Physical Review B*, 65(15):155303, 2002.

[54] B. Habib, J. Shabani, E. P. De Poortere, M. Shayegan, and R. Winkler. Tuning

of the spin-orbit interaction in two-dimensional GaAs holes via strain. *Physical Review B*, 75(15):153304, 2007.

[55] J. H. Davies. *The Physics of Low-dimensional Semiconductors.* Cambridge University Press, 1998.

[56] P. T. Coleridge, R. Stoner, and R. Fletcher. Low-field transport coefficients in GaAs/$Ga_{1-x}Al_xAs$ heterostructures. *Physical Review B*, 39(2):1120, 1989.

[57] C. Morrison, C. Casteleiro, D. R. Leadley, and M. Myronov. Complex quantum transport in a modulation doped strained Ge quantum well heterostructure with a high mobility 2D hole gas. *Applied Physics Letters*, 109:102103, 2016.

[58] C. Morrison, J. Foronda, P. Wisniewski, S. D. Rhead, D. R. Leadley, and M. Myronov. Evidence of strong spinorbit interaction in strained epitaxial germanium. *Thin Solid Films*, 602:8489, 2016.

[59] J. J. Lin and J. P. Bird. Recent experimental studies of electron dephasing in metal and semiconductor mesoscopic structures. *Journal of Physics: Condensed Matter*, 14:R501–R596, 2002.

[60] G. Bergmann. Weak localization in thin films: a time-of-flight experiment with conduction electrons. *Physics Reports*, 107(1), 1984.

[61] W. Knap, C. Skierbiszewski, A. Zduniak, E. Litwin-Staszewska, D. Bertho, F. Kobbi, J. L. Robert, G. E. Pikus, F. G. Pikus, S. V. Iordanskii, V. Mosser, K. Zekentes, and Y. B. Lyanda-Geller. Weak antilocalization and spin precession in quantum wells. *Physical Review B*, 53(7):3912, 1996.

[62] S. Hikami, A. I. Larkin, and Y. Nagaoka. Spin-orbit interaction and magnetoresistance in the two dimensional random system. *Progress of Theoretical Physics*, 63:707, 1980.

[63] S. V. Iordanskii, Y. B. Lyanda-Geller, and G. E. Pikus. Weak localization in quantum wells with spin-orbit interaction. *Journal of Experimental and Theoretical Physics Letters*, 60:206, 1994.

[64] L. E. Golub. Weak antilocalization in high-mobility two-dimensional systems. *Physical Review B*, 71(23):235310, 2005.

[65] G. J. Dolan and D. D. Osheroff. Nonmetallic conduction in thin metal films at low temperatures. *Physical Review Letters*, 43(10):721, 1979.

[66] S. Kobayashi, F. Komori, Y Ootuka, and W. Sasaki. ln t dependence of resistivity in two-dimensionally coupled fine particles of Cu. *Journal of the Physical Society of Japan*, 49(4):1635–1636, 1980.

[67] L. Van den Dries, C. Van Haesendonck, Y. Bruynseraede, and G. Deutscher. Two-dimensional localization in thin copper films. *Physical Review Letters*, 46(8):565, 1981.

[68] G. Bergmann. Consistent temperature and field dependence in weak localization. *Physical Review B*, 28(2):515, 1983.

[69] J. Fabian and S. D. Sarma. Spin relaxation of conduction electrons. *Journal of Vacuum Science & Technology B*, 17:1708, 1999.

[70] I. Žutiˇc, J. Fabian, and S. D. Sarma. Spintronics: Fundamentals and applications. *Reviews of Modern Physics*, 76(2):323, 2004.

[71] T. R. Bramblett, Q. Lu, T. Karasawa, M. A. Hasan, S. K. Jo, and J. E. Greene. Si(001)2×1 gas-source molecularbeam epitaxy from Si_2H_6: Growth kinetics and boron doping. *Journal of Applied Physics*, 76:1884, 1994.

[72] K. Y. Suh and H. H. Lee. Ge composition in $Si_{1-x}Ge_x$ films grown from SiH_2Cl_2/GeH_4 precursors. *Journal of Applied Physics*, 88:4044, 2000.

[73] P. F. Fewster. *X-Ray Scattering from Semiconductors.* Imperial College Press, 2000.

[74] P. van der Sluis. Determination of strain in epitaxial semiconductor layers by high-resolution x-ray diffraction. *Journal of Physics D: Applied Physics*, 26:A188–A191, 1993.

[75] D. Hull and D. J. Bacon. *Introduction to Dislocations.* Butterworth-Heinemann, Elsevier, fifth edition, 2011.

[76] Q. Zhong and D. Innis. Fractured polymer/silica fiber surface studied by tapping mode atomic force microscopy. *Surface Science*, 290(1-2):L688–L692, 1993.

[77] S. M. Sze and K. K. Ng. *Physics of Semiconductor Devices, 3rd Edition.* Wiley, 2006.

[78] R. W. Wood and A. Ellet. Polarized resonance radiation in weak magnetic fields. *Physical Review B*, 24:243, 1924.

[79] W. Hanle. *Physik*, 24, 1924.

[80] T. Sasaki, T. Oikawa, T. Suzuki, M. Shiraishi, Y. Suzuki, and K. Noguchi. Temperature dependence of spin diffusion length in silicon by hanle-type spin precession. *Applied Physics Letters*, 96:122101, 2010.

[81] V. F. Motsnyi, J. De Boeck, J. Das, W. Van Roy, G. Borghs, E. Goovaerts, and V. I. Safarov. Electrical spin injection in a ferromagnet/tunnel barrier/semiconductor heterostructure. *Applied Physics Letters*, 81:265–267, 2002.

[82] C. Morrison, P. Winiewski, S. D. Rhead, J. Foronda, D. R. Leadley, and M. Myronov. Observation of rashba zero-field spin splitting in a strained germanium 2D hole gas. *Applied Physics Letters*, 105:182401, 2014.

[83] J. Foronda, C. Morrison, J. E. Halpin, S. D. Rhead, and M. Myronov. Weak antilocalization of high mobility holes in a strained germanium quantum well heterostructure. *Journal of Physics: Condensed Matter*, 27:022201, 2015.

[84] P. Mooney. Strain relaxation and dislocations in SiGe/Si structures. *Materials Science & Engineering R-Reports*, 17:105–146, 1996.

[85] E. A. Fitzgerald, Y. H. Xie, D. Monroe, P. J. Silverman, J. M. Kuo, A. R. Kortan, F. A. Thiel, and B. E. Weir. Relaxed Ge_xSi_{1-x} structures for III-V integration with Si and high mobility two-dimensional electron gases in Si. *Journal of Vacuum Science & Technology B*, 10:1807, 1992.

[86] M. Grayson and F. Fischer. Measuring carrier density in parallel conduction layers of quantum Hall systems. *Journal of Applied Physics*, 98:013709, 2005.

[87] S. A. Studenikin, P. T. Coleridge, N. Ahmed, P. J. Poole, and A. Sachrajda. Experimental study of weak antilocalization effects in a high-mobility. *Physical Review B*, 68(3):035317, 2003.

[88] S. A. Studenikin, P. T. Coleridge, G. Yu, and P. J. Poole. Electron spinorbit splitting in a InGaAs/InP quantum well studied by means of the weak-antilocalization and spin-zero effects in tilted magnetic fields. *Semiconductor Science and Technology*, 20:1103, 2005.

[89] W. Z. Zhou, T. Lin, L. Y. Shang, G. Yu, Z. M. Huang, S. L. Guo, Y. S. Gui, N. Dai, J. H. Chu, L. J. Cui, D. L. Li, H. L. Gao, and Y. P. Zeng. Weak antilocalization and beating pattern in an InGaAs/InAlAs quantum well. *Solid State Communications*, 143(Issues 67):300303, 2007.

[90] Y. Lin, T. Koga, and J. Nitta. Effect of an $InP/In_{0.53}Ga_{0.47}As$ interface on spin-orbit interaction in $In_{0.52}Al_{0.48}As/In_{0.53}Ga_{0.47}As$ heterostructures. *Physical Review B*, 71(4):045328, 2005.

[91] G. M. Minkov, A. A. Sherstobitov, A. V. Germanenko, O. E. Rut, V. A. Larionova, and B. N. Zvonkov. Antilocalization and spin-orbit coupling in the hole gas in strained GaAs/$In_xGa_{1-x}As$/GaAs quantum well heterostructures. *Physical Review B*, 71(16):165312, 2005.

[92] B. Grbic, R. Leturcq, T. Ihn, K. Ensslin, D. Reuter, and A. D. Wieck. Strong spin-orbit interactions and weak antilocalization in carbon-doped p -type GaAs $Al_xGa_{1-x}As$ heterostructures. *Physical Review B*, 77(12):125312, 2008.

[93] S. J. Papadakis, E. P. D. Poortere, H. C. Manoharan, M. Shayegan, and R. Winkler. The effect of spin splitting on the metallic behavior of a two-dimensional system. *Science*, 26:2056–2058, 1999.

[94] M. Studer, G. Salis, K. Ensslin, D. C. Driscoll, and A. C. Gossard. Gate-controlled spin-orbit interaction in a parabolic. *Physical Review Letters*, 103(2):027201, 2009.

[95] X. Z. Liu, Y. G. Xu, G. Yu, L. M. Wei, T. Lin, S. L. Guo, J. H. Chu, W. Z. Zhou, Y. G. Zhang, and D. J. Lockwood. The effective g-factor in $In_{0.53}Ga_{0.47}As/In_{0.52}Al_{0.48}As$ quantum well investigated by magnetotransport measurement. *Journal of Applied Physics*, 113:033704, 2013.

[96] Y. Aharonov and A. Casher. Topological quantum effects for neutral particles. *Physical Review Letters*, 53(4):319, 1984.

[97] M. Ehlert, C. Song, M. Ciorga, M. Utz, D. Schuh, D. Bougeard, and D. Weiss. All-electrical measurements of direct spin hall effect in GaAs with Esaki diode electrodes. *Physical Review B*, 86(20):205204, 2012.

[98] A. Spiesser, S. Sharma, H. Saito, R. Jansen, S. Yuasa, and K. Ando. Electrical spin injection in p-type Si using Fe/MgO contacts. In *SPIE NanoScience +*

Engineering, pages 84610K–84610K–9. International Society for Optics and Photonics, 2012.

[99] S. Sharma, A. Spiesser, H. Saito, S. Yuasa, B. J. van Wees, and R. Jansen. Crystal-induced anisotropy of spin accumulation in Si/MgO/Fe and Si/Al_2O_3 /ferromagnet tunnel devices. *Physical Review B*, 87:085307, 2013.

[100] S. Sharma, A. Spiesser, S. P. Dash, S. Iba, S. Watanabe, B. J. van Wees, H. Saito, S. Yuasa, and R. Jansen. Anomalous scaling of spin accumulation in ferromagnetic tunnel devices with silicon and germanium. *Physical Review B*, 89(7):075301, 2014.

[101] D. D. Djayaprawira, K. Tsunekawa, M. Nagai, and K. Ando. 230% room-temperature magnetoresistance in CoFeB/MgO/CoFeB magnetic tunnel junctions. *Applied Physics Letters*, 86:092502, 2005.

[102] Y. Ding, D. O. Northwood, and A. T. Alpas. Fabrication of microlaminated Al/Al_2O_3 composites by magnetron sputtering for tribiological applications. In *Surface & Coatings Technology*, volume 62, pages 448–453. Elsevier, 1993.

[103] T. Marron, S. Takashima, Z. Li, and T. P. Chow. Impact of annealing on ALD Al_2O_3 gate dielectric for GaN MOS devices. *physica status solidi (c)*, 9(34):907–910, 2011.

[104] H. Mehrer. *Diffusion in Solids - Fundamentals, Methods, Materials, — Helmut Mehrer — Springer*, volume 155 of *Springer Series in Solid-State Sciences*. Springer, 2007.

[105] D. R. Gajula, D. W. McNeill, B. E. Coss, H. Dong, S. Jandhyala, J. W. Kim, R. M., and B. M. Armstrong. Low temperature fabrication and characterization of nickel germanide schottky source/drain contacts for implant-less germanium p-channel metal-oxide-semiconductor field-effect transistors. *Applied Physics Letters*, 100:192101, 2012.

[106] D. K. Schroder. *Semiconductor Material and Device Characterization, 3rd Edition*. Wiley-IEEE Press, 3 edition, 2006.

[107] O. M. J. van 't Erve, A. T. Hanbicki, M. Holub, C. H. Li, C. Awo-Affouda, P. E. Thompson, and B. T. Jonker. Electrical injection and detection of spin-polarized carriers in silicon in a lateral transport geometry. *Applied Physics Letters*, 91:212109, 2007.

[108] Y. Yafet. g factors and spin-lattice relaxation of conduction electrons. *Solid State Physics*, 14:198, 1963.

[109] A. Spiesser, S. Watanabe, H. Saito, S. Yuasa, and K. Ando. Effective creation of spin polarization in p-type Ge from a Fe/GeO_2 tunnel contact. *Japanese Journal of Applied Physics*, 54:04CM01, 2013.

[110] Y. Pu, J. Beardsley, P. M. Odenthal, A. G. Swartz, R. K. Kawakami, P. C. Hammel, E. Johnston-Halperin, J. Sinova, and J. P. Pelz. Correlation of electrical spin injection and non-linear charge-transport in Fe/MgO/Si. *Applied Physics Letters*, (103):012402, 2013.

[111] O. Txoperena, M. Gobbi, A. Bedoya-Pinto, F. Golmar, X. Sun, L. E. Hueso, and F. Casanova. How reliable are hanle measurements in metals in a three-terminal geometry? *Applied Physics Letters*, (102):192406, 2013.

[112] P. M. Tedrow and R. Meservey. Spin polarization of electrons tunneling from films of Fe, Co, Ni, and Gd. *Physical Review B*, 7:318, 1973.

[113] O. Txoperena and F. Casanova. Spin injection and local magnetoresistance effects in three-terminal devices. *Journal of Physics D: Applied Physics*, 49:133001, 2016.